Timing and Evolution of Structures within the Southeastern Greater Caucasus and Kura Fold-Thrust Belt from Multiproxy Sediment Provenance Records

Adam M. Forte[1] (aforte8@lsu.edu), Eric S. Cowgill[2] (escowgill@ucdavis.edu), Dawn Y. Sumner[2] (dysumner@ucdavis.edu) Dominique I. Garello[1] (dgarello1@lsu.edu), Nathan A. Niemi[3] (naniemi@umich.edu), K. Colton Fowler[1] (kfowl11@lsu.edu)

[1]Department of Geology & Geophysics, Louisiana State University, Baton Rouge, LA, USA
[2]Department of Earth and Planetary Sciences, University of California, Davis, CA, USA
[3]Department of Earth & Environmental Sciences, University of Michigan, Ann Arbor, MI, USA

This paper is a non-peer reviewed preprint submitted to EarthArXiv. This paper has been submitted to Geosphere for peer review.

Timing and Evolution of Structures within the Southeastern Greater Caucasus and Kura Fold-Thrust Belt from Multiproxy Sediment Provenance Records

Adam M. Forte[1], Eric S. Cowgill[2], Dawn Y. Sumner[2], Dominique I. Garello[1], Nathan A. Niemi[3], K. Colton Fowler[1]

[1]Department of Geology & Geophysics, Louisiana State University, Baton Rouge, LA, USA
[2]Department of Earth and Planetary Sciences, University of California, Davis, CA, USA
[3]Department of Earth & Environmental Sciences, University of Michigan, Ann Arbor, MI, USA

ABSTRACT

The west-northwest trending Greater Caucasus (GC) mountains locally represent the main locus of post-Pliocene shortening within the north central Arabia-Eurasia collision. Although recent low-temperature thermochronology constrains the timing of orogen formation, the evolution of major structures remains enigmatic - particularly regarding the internal kinematics within this young orogen and the Kura Fold-Thrust Belt (KFTB), which flanks its southeastern margin. Here we use a multiproxy provenance analysis to investigate the tectonic history of both the southeastern GC and KFTB by presenting new data from a suite of sandstone samples from the KFTB, including point counts, whole-rock geochemistry, and detrital zircon (DZ) U-Pb geochronology. To define source terrains for these sediments, we integrate additional new whole-rock geochemical analyses with published DZ results and geological mapping. Our analysis reveals a progressive change up-section from a dominantly volcanic or volcaniclastic source, presently exposed as a thin strip along the southeastern GC, to a flysch source, now exposed in the core of the GC. In detail, while point counts and geochemistry suggest a consistent history of changing sediment sources, more limited DZ geochronology suggests less up-section change. We interpret this apparent discrepancy to reflect the onset of sediment recycling and local reworking of sediments within the KFTB, selectively weathering unstable mineral species that define the volcaniclastic source terrain. We conclude that this transition constrains the timing of the initiation of the central KFTB, which we argue initiated nearly synchronously along-strike.

1. INTRODUCTION

The provenance histories of siliciclastic sediments in foreland basins often provide a robust, and in some cases, unique record of the past structural and kinematic history of the flanking orogenic system (e.g., Sinclair, 1997; DeCelles et al., 1998; Lawton et al., 2010; Nagel et al., 2014; Leary et al., 2016; Capaldi et al., 2020). The initiation of large thrust systems within an orogen can expose new source terranes, which is recorded in the foreland basin as a change in the provenance of sediments (e.g., Garzanti et al., 2004; Lease et al., 2007). These shifts in provenance can elucidate the order of initiation, direction of propagation, and style of structures within a mountain range, thus providing crucial constraints for tectonic models of orogen evolution (e.g., Carrapa et al., 2006; Panaiotu et al., 2007; Bande et al., 2012; Laskowski et al., 2013; Garber et al., 2020). In deeply eroded orogens with large amounts of total exhumation, the structures responsible for changes in foreland basin provenance may no longer exist within the mountain range. Thus, provenance studies in young mountain ranges provide a unique opportunity to explore the degree to which major structural changes are preserved in the sedimentary record in the case where both the causative structures and foreland-basin record still exist.

The Greater Caucasus (GC) Mountains and associated foreland basins (Figure 1), at the northern margin of the Arabia-Eurasia collision zone, provide an excellent opportunity to use provenance records to elucidate recent structural changes in an orogen and fringing fold-thrust belts. Over the last decade, low-temperature thermochronologic analyses have broadly constrained the timing of orogen initiation to 5-10 Ma (Avdeev and Niemi, 2011; Vincent et al., 2011, 2020; Forte et al., 2022a; Tye et al., 2022). While recent work by Trexler et al., (2022) has significantly clarified the locations, geometry, and nature of many of the first-order structures within the internal Greater Caucasus, the timing and evolution of these first-order structures remain under-constrained with the exception of very specific locations in the western GC (Vasey et al., 2020) and extreme eastern GC (Tye et al., 2022). Likewise, the importance of fringing foreland fold-thrust belts for accommodating shortening in the GC is now understood in the north central and western (Sobornov, 1994, 1996, 2021; Forte et al., 2014), southwestern (Banks et al., 1997; Tsereteli et al., 2016; Tibaldi et al., 2017, 2018; Trexler et al., 2020; Alania et al., 2021b; Tibaldi et al., 2021), southcentral (Alania et al., 2021a), and southeastern (Forte et al., 2010, 2013, 2014; Alania et al., 2015) GC. However, when these fold-thrust belts began to form generally remains enigmatic.

Here we focus on the Kura Fold-Thrust Belt (KFTB), which fringes the southeastern GC in the countries of Azerbaijan and Georgia. Since its initiation, the KFTB has likely accommodated upwards of 50% of the orogen-perpendicular shortening between Arabia and Eurasia, and nearly all of the convergence between the Greater and Lesser Caucasus between 45-49°E (Forte et al., 2010, 2013). The formation of the KFTB represents a significant structural reorganization within the GC (e.g., Forte et al., 2010; Mosar et al., 2010). Thus, constraining the timing and evolution of deformation within the KFTB is critical for understanding the broader structural evolution of the GC. Constraining timing of the KFTB and associated GC structural reorganization is also critical to understanding the context of its formation. For example, based on relatively limited data, Forte et al., (2013) originally hypothesized that initiation of the Kura Fold-Thrust Belt (KFTB), and resultant widening of the GC, initiated at 1.5-1.8 Ma, coincident with regional records of an increase in aridity (e.g., Kvavadze and Vekua, 1993; Gabunia et al., 2000; Kovda et al., 2008; Messager et al., 2010a, 2010b). Forte et al., (2013) considered that this shift to more arid conditions could have initiated orogen widening and KFTB formation, consistent with the proposal that active, doubly-vergent orogens experiencing less efficient erosion will expand (Whipple and Meade, 2004, 2006). The viability of such a mechanism depends fundamentally on the timing of the structural reorganization and the extent to which the initiation of the KFTB was synchronous or asynchronous along-strike. While some prior work suggested a diachronous initiation of the KFTB along strike (Forte et al., 2010), recent constraints suggest a more synchronous initiation is viable, although it is essential to note that these constraints come from the extreme western and eastern ends of the KFTB (Forte et al., 2013; Lazarev et al., 2019; Sukhishvili et al., 2020). Further constraint on timing within the central KFTB, and a broader indication of how this may relate to evolution of the internal structure of southeastern GC, is needed to better understand the tectonic context of the KFTB.

The foreland sediments exposed within the KFTB itself may provide an avenue through which to constrain the timing of formation of the KFTB and evolution of the GC, specifically through tracking changes in sediment provenance. Prior work describing source terrains within the GC broadly suggest relatively distinct, thrust-bounded packages that have the potential to leave diagnostic signatures within the KFTB sediments (e.g., Cowgill et al., 2016; Tye et al., 2020). However, the previously available provenance data within the Kura Basin and associated KFTB region are limited and focused primarily on the oil-producing sandstones of the Productive Series at the extreme eastern edge of the Kura Basin (Morton et al., 2003; Allen et al., 2006; Abdullayev et al., 2018) or on sediments that largely predate formation of the KFTB as inferred at its western and eastern ends (Tye et al., 2020). To explore the tectonic history of both the GC and KFTB, we present new detailed provenance analyses from Miocene-Pleistocene sedimentary rocks that are now exposed within and span much of the KFTB. A majority of prior provenance work focuses on detrital zircon (DZ) geochronology (Allen et al., 2006; Cowgill et al., 2016; Abdullayev et al., 2018; Tye et al., 2020), which we also perform, but consider in conjunction with sandstone composition from point counts and bulk-sample major and trace element geochemical data. To compare source characterizations between DZ and geochemical and/or framework grain compositions, we supplement our foreland samples with additional geochemical analyses of modern river sediments draining the southern Greater Caucasus and northern Lesser Caucasus, and Mesozoic-aged sandstone samples from within the Greater Caucasus. Combining these datasets with prior work on the provenance, structure, and stratigraphy of the KFTB and southeastern GC allows us to further constrain the tectonic history of this portion of the Greater Caucasus.

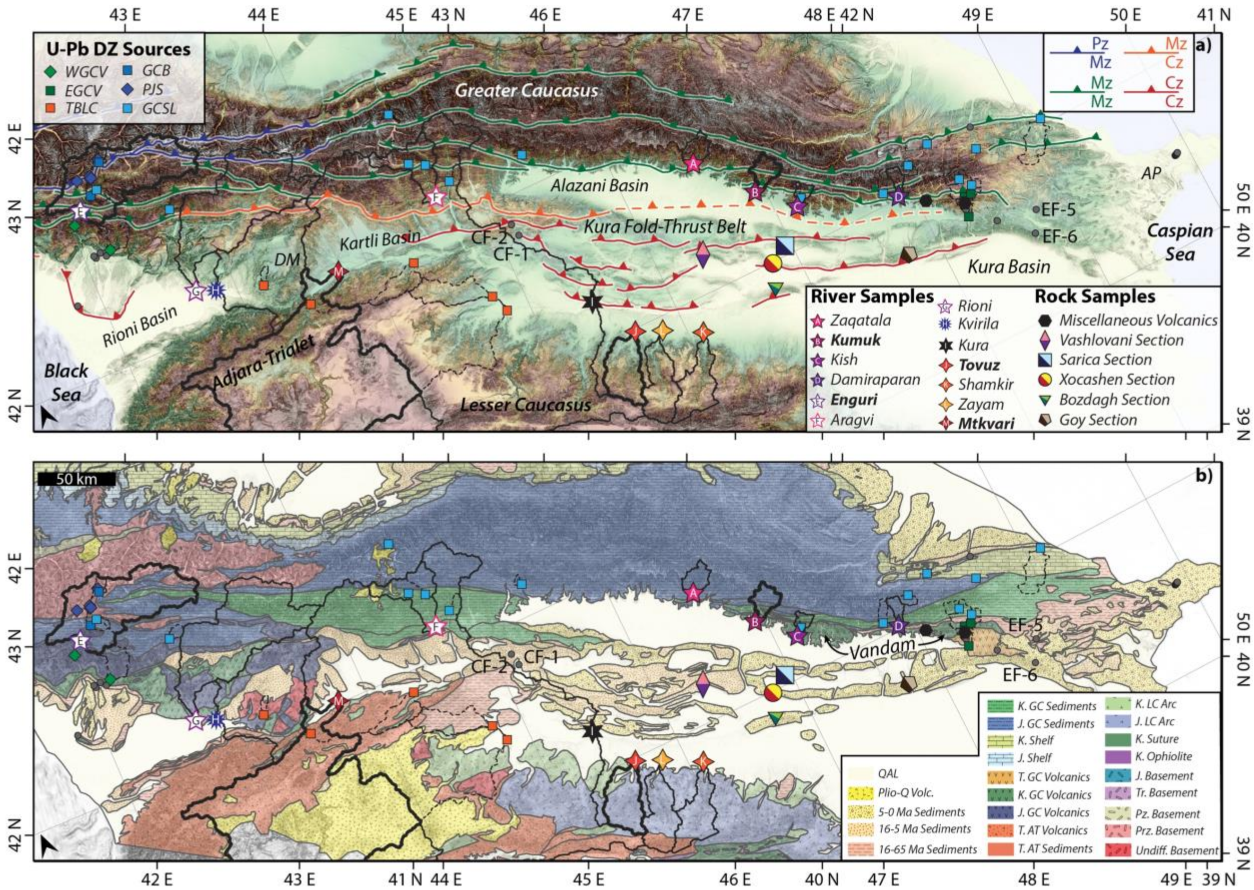

Figure 1 – Sample location and regional geology. a) Locations of the modern river and bedrock samples we analyze (bottom right explanation in panel a). Also shown with colored symbols are the locations of samples and respective detrital zircon U-Pb source terranes from Tye et al., (2020) and references therein and including additional samples from Forte et al., (2022a) (top left explanation in panel. See text for definition of source names. a). Watershed boundaries for modern sediment samples are shown, with bold watershed boundaries indicating catchments for which we present geochemical data and that Cowgill et al., (2016) presented detrital zircon geochronology. Note that modern river samples for Kura and Mtkvari represent samples from the same river, where the Mtkvari is sampled upstream from the Kura and reflects the Georgian (Mtkvari) and Azerbaijani (Kura) names for the river. Gray circles are other foreland provenance samples from Tye et al. (2020), Allen et al., (2006), and Abdullayev et al., (2018). Previous foreland samples from Tye et al. (2020) that we discuss in detail are labeled with their sample names. Locations of major thrusts from Trexler et al., (2022), colored by the age relations of packages they structurally juxtapose. Abbreviations are as follows, DM – Dzirual Massif, AP – Apsheron Peninsula. b) Same samples from 1a, but considering the simplified geology from Forte et al., (2014). Also highlighted is the zone of predominantly Cretaceous volcanic and volcaniclastic rocks in the eastern GC, which we refer to here as the Vandam zone consistent with prior literature (e.g., Tye et al., 2022).

2. BACKGROUND

2.1 Tectonic Setting

The GC are the main locus of convergence within the central Arabia-Eurasia collision zone and represent its most northern structural extent (e.g., Philip et al., 1989; Jackson, 1992; Allen et al., 2004; Dhont and Chorowicz, 2006; Reilinger et al., 2006). The range results from ongoing Cenozoic shortening that partially inverted a Jurassic-Cretaceous back-arc basin that opened north of the Pontide-Lesser Caucasus (LC) island arc during north directed subduction of Neotethyan oceanic lithosphere (e.g., Adamia et al., 1977; Gamkrelidze, 1986; Zonenshain and Le Pichon, 1986; Cowgill et al., 2016; Vincent et al., 2016; van Hinsbergen et al., 2019;

Vasey et al., 2021). The bedrock geology of the GC (Figure 1b) is dominated by Jurassic-Cretaceous, shallow-marine carbonate rocks along the northern flank, Jurassic to Cretaceous flysch to molasse within much of the core of the orogen, and Jurassic to Cretaceous volcanic and volcaniclastic rocks along the southern flank (e.g., Saintot et al., 2006; Adamia et al., 2011a; Forte et al., 2014; Cowgill et al., 2016; Tye et al., 2020). Several observations of the bedrock geology are particularly important with respect to sediment provenance and potential source terranes: (1) within the GC, exposures of intrusive, metamorphic, and sedimentary rocks predating Jurassic rifting in the GC back-arc basin are exclusively present in the western GC; (2) there are two distinct packages of volcanic/volcaniclastic rocks along the southern margin of the GC, a larger and wider package in the west and a narrower and less expansive package in the east; the latter is sometimes referred to as the Vandam zone and both are considered to be genetically linked with the similarly aged Pontide-Lesser Caucasus Arc (e.g., Kopp and Shcherba, 1985); and (3) there are various small exposures of Paleozoic to Precambrian crystalline rocks within the Dzirula Massif and Lesser Caucasus (e.g., Khrami & Loki Massifs - Rolland et al., 2011).

Significant debate has centered on the early Cenozoic geometry and dimensions of the GC back-arc basin north of the LC (Cowgill et al., 2016, 2018; Vincent et al., 2016, 2018), but paleogeographic reconstructions constrain the minimum NE-SW width to being no more than 200-300 km (van der Boon et al., 2018; van Hinsbergen et al., 2019), similar to the dimensions of the Black Sea and South Caspian basins, which are likely remnants of the same back-arc basin system (Zonenshain and Le Pichon, 1986). Timing of initiation of closure and shortening of the GC back-arc basin is unclear, but had likely begun by the Eocene-Oligocene (e.g., Vincent et al., 2007) and was accommodated in part by subduction based on preservation of a remnant subducted slab in the eastern GC (Skolbeltsyn et al., 2014; Mumladze et al., 2015; Gunnels et al., 2020). The timing of the transition from subduction to collision and beginning of significant upper plate shortening and exhumation has also proven controversial, but recent new results from, and syntheses of, low-temperature thermochronology have largely confirmed the original suggestion by Avdeev and Niemi (2011) of initiation of rapid exhumation between 10-5 Ma throughout much of the range (e.g., Vincent et al., 2020; Forte et al., 2022a; Tye et al., 2022).

Since ~2 Ma, deformation has stepped out of the main range to form a series of fold-thrust belts including the Rioni Fold-Thrust Belt in the southwest (Banks et al., 1997; Tsereteli et al., 2016; Tibaldi et al., 2017, 2018; Trexler et al., 2020; Alania et al., 2021b; Tibaldi et al., 2021), the Terek-Sunzha Fold-Thrust belt in the northern central range (Sobornov, 1994, 1996, 2021; Forte et al., 2014), and the KFTB in the southeast (Forte et al., 2010, 2013, 2014; Alania et al., 2015; Sukhishvili et al., 2020). The timing of the formation of these thrust-belts is roughly synchronous with a change to more arid conditions (e.g., Kvavadze and Vekua, 1993; Gabunia et al., 2000; Kovda et al., 2008; Messager et al., 2010a, 2010b) and an internal structural reorganization of the GC (Forte et al., 2022a). All of these structural systems accommodate shortening within their respective extents, and the KFTB specifically has accommodated nearly all LC-GC convergence in the eastern half of the range since its establishment (Forte et al., 2010, 2013). As described previously, different suggestions exist for the exact timing and spatial patterns of KFTB initiation. Interpreting patterns of syn-tectonic vs pre-tectonic stratigraphy from prior coarse scale mapping, Forte et al., (2010), suggested that the KFTB may have initiated in the west and propagated eastward. However, subsequent work both in terms of refined structure (Forte et al., 2013) and stratigraphic relations (Forte et al., 2015a) along with improved age constraints for pre- and syn-tectonic strata (Lazarev et al., 2019; Sukhishvili et al., 2020) have cast doubt on the idea of diachronous initiation, instead suggesting that the KFTB may have initiated synchronously along-strike. However, significant data gaps remain.

The interior of the GC is dominated by south-directed thrusts and reverse faults, which progressively steepen toward the interior of the range (Philip et al., 1989; Saintot et al., 2006; Mosar et al., 2010; Adamia et al., 2011b; Somin, 2011; Trexler et al., 2022). While many prior works describe the structural architecture of the internal GC in the context of a single master structure or structures, often referred to as the Main Caucasus Thrust (e.g., Philip et al., 1989; Mosar et al., 2010), recent work has suggested that the majority of thrusts along the southern margin of the range accommodate similar amounts of displacement (Vasey et al., 2020; Trexler et al., 2022). More critical to our efforts are that many of these structures juxtapose rocks of different composition or detrital zircon age populations, and initiation and activity of these structures during deformation of the GC should produce diagnostic provenance changes in the foreland basin (Figure 1). Of particular importance is the Vandam zone (Figure 1b), a distinctive, thrust-bounded terrane of predominantly Mesozoic volcanic and volcaniclastic rocks that was accreted into the range between 13-3 Ma and subsequently deformed (Tye et al., 2022).

2.2 Kura Basin Framework and Regional Timescale

Here we focus primarily on the stratigraphic framework of the Kura Basin (KB), a foreland basin to the southeast of the GC and subbasin of the South Caspian (Figure 1, e.g., Khain, 1975; Philip et al., 1989; Kremenetskiy et al., 1990). Although at present the GC is separated from the KB by the KFTB and piggy-back Alazani Basin, all three components formed a single continuous basin prior to the formation of the KFTB. Thus, we consider the stratigraphy exposed within the KFTB to largely represent deposition within this former, larger version of the KB. Results from deep-boreholes drilled during the 1970s reveal that the Cenozoic stratigraphic fill of the KB is deposited on top of Jurassic-Cretaceous volcanic rocks thought to be associated with the Lesser Caucasus (LC) arc (Agabekov et al., 1976; Shikalibeily et al., 1988). Seismic velocities within the KB suggests that the Cenozoic sediment thicknesses exceed 10 km through much of the basin, with thickness likely exceeding 15 km at the western and eastern ends of the KFTB (Gunnels et al., 2020). The seismic velocity of the Mesozoic floor of the KB is consistent with it either being oceanic crust or highly attenuated continental crust (McKenzie et al., 2019; Gunnels et al., 2020), consistent with it representing a still unsubducted portion of the former GC back-arc basin.

Exposures of KB stratigraphy in the KFTB vary from shallow marine to terrestrial and are predominantly siliciclastic, with general coarsening upward trends observed throughout most sections (e.g., Agustí et al., 2009; van Baak et al., 2013; Forte et al., 2013, 2015a; Lazarev et al., 2021). The depositional environments of the KFTB stratigraphy reflect influences both from the development of the GC and KFTB (e.g., Forte et al., 2013, 2015), but also large magnitude base level changes of the Caspian Sea during the late Cenozoic (e.g., Popov et al., 2006; Forte and Cowgill, 2013; van Baak et al., 2017; Krijgsman et al., 2019; Lazarev et al., 2021). Variations in Caspian base level, along with potentially related intermittent connections between the Black and Caspian Sea along the southern rangefront of the GC (e.g., Popov et al., 2010; Forte and Cowgill, 2013) are often considered a first-order driver of stratigraphy within the KB. As such, the stratigraphy of the KB and surrounding regions is classified in terms of regional stages associated with transgressions and regressions of the Caspian Sea, and associated changes in biota (e.g., Zubakov and Borzenkova, 1990; Jones and Simmons, 1996).

For the sections within the KFTB presented here, we are primarily concerned with, from oldest to youngest, the Meotian (Base 7.65 Ma - Palcu et al., 2019), Pontian (Van Baak et al., 2016), Productive Series (Base 5.33 Ma - Aghayeva et al., 2023), Ackgahylian (Base 2.7 Ma - Krijgsman et al., 2019; Base 2.95 Ma - Lazarev et al., 2021), Apsheronian (Base 2.1 Ma - Lazarev et al., 2019), and Bakunian (Base 0.8 Ma - van Baak et al., 2013) regional Caspian stages. Estimation of the age of boundaries between Caspian stages, their correlations to similar stages elsewhere in the former extent of Paratethys, and their correlation to the global timescales have all proven extremely controversial, having been revised and/or shifted numerous times in the past several decades (see review in Krijgsman et al., 2019). While concentrated magneto- and biostratigraphic work has helped to significantly clarify the temporal extents of the individual Caspian and related Paratethyan stages, disagreements remain, which may in part reflect that; (1) specific transgressive and regressive surfaces that bound stages occur at different times in different Paratethyan basins; and (2) that these same surfaces may be time transgressive within individual basins and their subbasins (e.g., Vasiliev et al., 2011; van Baak et al., 2013; Forte et al., 2015a; van Baak et al., 2017; Richards et al., 2018; van Baak et al., 2019; Krijgsman et al., 2019; Lazarev et al., 2019, 2021).

In the present study, we consider two different versions of the Caspian timescale. The first is constrained primarily from magnetostratigraphy of several sections in the Apsheron Peninsula and eastern Kura Basin (Krijgsman et al., 2019 and references therein). The second is an alternate timescale based on magnetostratigraphy from the Kvabebi section within the western KFTB (Lazarev et al., 2021). The difference between these two timescales is the duration of the Akchagyl stage, and specifically the age of the base of this regional stage. The base of the Akchagyl represents a transgressive surface reflecting a ~200 meter base level rise of the Caspian following an extreme (~600 m below modern base level) regression during the preceding Productive Series time (e.g., van Baak et al., 2017, 2019; Lazarev et al., 2021). In the composite timescale of Krijgsman et al., (2019), the Akchagylian spans from 2.7 to 2.1 Ma, whereas the Akchagylian is longer in the timescale of Lazarev et al., (2021) and spans from 2.95 to 2.1 Ma. Lacking a basis on which to choose between these two alternate timescales, we consider both when correlating the KFTB stratigraphy to the global timescale.

2.3 Prior Work on Source Terranes

Potential source terranes and their expected provenance signatures in foreland sediments for the Caucasus region are relatively well characterized in terms of U-Pb ages of zircons (Allen et al., 2006; Wang et al., 2011; Cowgill et al., 2016; Vasey et al., 2020; Tye et al., 2020; Forte et al., 2022a; Trexler et al., 2022) and to a lesser extent, heavy mineral assemblages (Morton et al., 2003; Morton and Yaxley, 2007; Vezzoli et al., 2014, 2020). Prior work by Tye et al., (2020) integrated both modern sediments and bedrock samples (Allen et al., 2006; Wang et al., 2011; Cowgill et al., 2016; Vasey et al., 2020; Trexler et al., 2022) to define a suite of 7 distinct source terranes distinguishable in detrital zircon U-Pb age populations within the Caucasus region: Eurasian interior (EUI), Pre-Jurassic sedimentary rocks (PJS), Greater Caucasus basement (GCB), Greater Caucasus siliciclastics (GCSL), eastern Greater Caucasus volcaniclastics

(EGCV), western Greater Caucasus volcaniclastics (WGCV), and Transcaucasus basement and Lesser Caucasus arc (TBLC). These source terranes broadly define three groups: those that reflect a source from the East European Craton to the north of the GC (EUI), a GC source (PJS, GCB, GCSL, EGCV, WGCV), or a LC source (TBLC). In more detail, the GC sources roughly correspond to distinct tectonostatigraphic zones within the GC itself, with the PJS and GCB reflecting exposures in the core of the western orogen, the GCSL corresponding to the Jurassic to Cretaceous flysch exposed throughout the range, and the WGCV and EGCV corresponding to the two volcanic packages along the southern rangefront, the latter of which is also effectively the same as the Vandam zone. The 7 source terranes defined by Tye et al., (2020) largely reflect differences in the relative proportions of 6 different distinct age populations within given samples, specifically: (1) grains < 90 Ma associated with the LC arc, (2) grains 90-200 Ma associated with the LC arc or GC rifting, (3) grains 200-380 Ma associated with the Variscan orogeny, (4) grains 380-500 Ma associated with an earlier arc associated with the Hunia superterrane, (5) grains 500-900 Ma associated with the Pan-African orogeny, and (6) >900 Ma grains associated with East European craton.

A relatively smaller amount of work has considered the heavy mineral assemblage of potential source terranes within the Caucasus region (e.g., Morton et al., 2003; Morton and Yaxley, 2007; Vincent et al., 2007; Vezzoli et al., 2014, 2020). Here we focus on results from Morton et al., (2003) and Morton & Yaxley, (2007) as Vezzoli et al., (2014, 2020) both focus on sources in the far western and northern GC, and as such the extent to which these are relevant for provenance within the Kura Basin is unclear. Morton et al., (2003) and Morton & Yaxley, (2007) consider heavy mineral assemblages from the modern Volga, representing contributions from the East European Craton, the modern Kura River, which drains both the GC and LC, and several smaller rivers draining the extreme eastern GC. Broadly, the results highlight relatively distinct provenance signatures between all three sources. The Volga includes primarily stable, more evolved and felsic components. The Kura river – and by proxy the LC – is dominated by more unstable components like clinopyroxenes and amphiboles. Finally, the GC reflects a mixture of both stable and unstable components, including very similar species like clinopyroxene as observed in the LC-draining Kura river, but generally in lower abundances than in the Kura river (Morton et al., 2003; Morton and Yaxley, 2007).

2.4 Prior Work on Foreland Provenance

There are limited published studies of provenance in the foreland basins of the GC. Existing results include isolated data from the Rioni Fold-Thrust Belt and related Cenozoic stratigraphy of the western GC (Vincent et al., 2013, 2014; Tye et al., 2020), the extreme western and eastern termini of the KFTB (Tye et al., 2020), and the most expansive dataset focusing on exposures of Productive Series strata on the Apsheron Peninsula and in the eastern KB (Morton et al., 2003; Allen et al., 2006; Morton and Yaxley, 2007; Abdullayev et al., 2018). Those from the KFTB, KB, and Apsheron Peninsula are the most relevant here.

Results of heavy mineral analysis of Productive Series sandstones sampled on the Apsheron Peninsula are similar to those of the modern Volga River and rivers draining the eastern tip of the Greater Caucasus (Morton et al., 2003; Morton and Yaxley, 2007). This is consistent with the previous suggestion that during the extreme Caspian Sea low-stand coeval with Productive Series deposition, the paleo-Volga River mouth migrated southwards and entered the Caspian near the modern day position of the Apsheron Peninsula (e.g., Reynolds et al., 1998; Aliyeva, 2005; Kroonenberg et al., 2005; Vincent et al., 2010). Contrastingly, samples of Productive Series sandstones from the eastern margin of the Kura Basin, near the modern Kura River, contain a decidedly different heavy mineral assemblage, more consistent with samples from the modern Kura River taken near its outlet into the Caspian Sea (Morton et al., 2003; Morton and Yaxley, 2007). Generally, both modern Volga River samples and Apsheron Peninsula Productive Series rocks are characterized by more evolved, felsic heavy mineral assemblages when compared with samples from the Kura River or Kura Basin Productive Series rocks (Morton and Yaxley, 2007). In general, Morton et al., (2003) and Morton & Yaxley, (2007) suggest that the presence of distinctive unstable species like clinopyroxene and calcic amphiboles in sediments are strongly suggestive of LC sourcing.

The heavy mineral results from the Apsheron Peninsula exposures of Productive Series sediments are largely reinforced by detrital zircon age populations (Allen et al., 2006; Abdullayev et al., 2018), which are dominated by >900 Ma grains characteristic of the East European Craton and rivers draining this terrane (Safonova et al., 2010; Wang et al., 2011; Tye et al., 2020). Detrital zircon data from the extreme eastern GC and KFTB and western KFTB, sampled from sediments ranging in age from Paleogene to Quaternary instead record mixtures of source terranes indicative of sourcing from either the GC or LC with minimal input from the East European Craton (Tye et al., 2020). The majority of foreland samples from Tye et al., (2020) show affinity with one or more of the GC-associated sources, but some samples (e.g., sample CF-1), even those extremely proximal to or within the modern GC (e.g., sample EF-6), show affinity with the TBLC (i.e., Lesser Caucasus or Transcaucasus basement source). Where such provenance affinities are present, Tye et al., (2020) largely follow Morton et al., (2003) in considering these samples to reflect deposition of sediment delivered by a paleo-Kura river system, predominantly draining the LC, requiring a paleo-Kura river that is in part shifted northward with respect to its modern position and much closer to the GC rangefront. Ultimately, with respect to the questions we consider here, the majority of available detrital zircon data within the southeastern foreland; (1) are derived from sediments that are largely both pre-tectonic with respect to both rapid exhumation of the GC and possible formation of the KFTB and (2) also lack detailed stratigraphic or structural context (Tye et al., 2020), and as such, interpreting either unroofing patterns from the GC or details of the KFTB are challenging.

2.5 Summary and Framework for Work

From the prior work on both the tectonics and foreland provenance, we identify a set of key problems that are under-constrained within the southeastern GC and KFTB and that are addressable by sediment provenance techniques, specifically: (1) how did the provenance of the northern Kura Basin evolve during the transition from subduction to collision and subsequent growth of the GC; (2) what does the evolution of foreland provenance during this time suggest for structural evolution of the southeastern GC; and (3) does the provenance constrain the timing of KFTB initiation and along-strike evolution? To address these questions, we begin by describing the stratigraphic context of the provenance samples we analyze (section 3), the analytical methods (section 4) and statistical (section 5) methods we employ, the results of our analyses (section 6), and finally the implications of these results (section 7).

3 SAMPLES AND THEIR STRATIGRAPHIC CONEXT

We collected four general types of samples for this study (Tables 1, 2, and 3), (1) volcanic ash from within Mio-Pleistocene sections exposed within the KFTB or adjacent regions to enable stratigraphic correlations, (2) sandstone with unknown provenance from the same stratigraphic sections, (3) modern stream sediments with catchments in adjacent mountains to characterize potential source areas for the KFTB sandstones, and (4) Mesozoic volcanic and volcaniclastic rocks of the Vandam zone now exposed within the Greater Caucasus. The suite of 27 KFTB sandstones with unknown provenance were collected while measuring the stratigraphic sections summarized above and reported in Forte (2012), Forte et al., (2013, 2015a) and van Baak et al. (2013). These samples were typically 2-4 kilograms of medium to coarse-grained sandstone.

To interpret the provenance records, it is necessary to correlate the measured sections from which those provenance records were sampled. Forte (2012) proposed an initial set of correlations between the five measured sections considered here. However, that correlation lacked detailed tephra glass geochemistry and predated both new magnetostratigraphic work (Lazarev et al., 2019) and significant revisions to the regional timescale (e.g., van Baak et al., 2017; Krijgsman et al., 2019; Lazarev et al., 2021). To be able to consider variations in provenance through time, in Section 6.2 we present an updated correlation based on these new data sources and integrated with prior magnetostratigraphy (e.g., van Baak et al., 2013) and mapping (Abdullaev et al., 1957; Ali-Zade, 2005; Forte et al., 2015a).

The detailed stratigraphy of each of the fives sections is described in prior work, and we refer readers to the source publications for full descriptions, logs, and ancillary data (e.g., biostratigraphy) for the sections at Vashlovani and Sarica (Forte et al., 2015a), Xocashen (van Baak, 2010; Forte, 2012; van Baak et al., 2013), Bozdagh (Forte, 2012), and Goy (Forte et al., 2013; Lazarev et al., 2019). In the following we summarize the stratigraphy of each section to provide context for the 8 ash and 27 sandstone samples that we analyze. Sandstone sample names indicate both the name of the measured section and stratigraphic height at which the sample was collected. Thus, sample V-15 is from the Vashlovani section, 15 meters above the section base. Original (field) sample names are reported in Table 2. Summary geologic maps showing the detailed locations and geological context of the sections are provided in the supplement (Figures S1-5).

3.1 Vashlovani

The Vashlovani section is 1475 meters thick and is located in eastern Georgia (Figure 1). On the basis of prior geologic mapping (Abdullaev et al., 1957), Vashlovani spans from the Meotian-Pontian to the Apsheronian (Figure S1). Original mapping reported an unconformable contact between the undifferentiated Meotian-Pontian sediments and the overlying Akchagylian, but Forte et al., (2015a) reports an ~150-meter-thick section of conglomerate that they interpret as a condensed section of the Productive Series. Forte et al., (2015a) divides the section into three units, which from oldest to youngest are: (V1) an 850 meter basal unit consisting of predominantly mudstone and sandstone and interpreted as meandering fluvial and overbank deposits; (V2) a 150 meter conglomeratic unit interpreted as a braided fluvial system; and (V3) a 475 meter interlayered mudstone and sandstone sequence with a generally high proportion of sandstone collectively interpreted as a meandering fluvial environment.

Here we present 7 samples from the Vashlovani section, including 2 (V-15 and V-1240) that we analyze for detrital zircon U-Pb ages. A subset of the U-Pb age population for V-1240 was presented by Forte et al., (2015a) to constrain maximum depositional age for this sample.

3.2 Sarica

The Sarica section is 2045 meters long and is located in western Azerbaijan (Figures 1 and S2). Mapping from Forte et al., (2015a) indicates that Sarica spans from the Productive Series to the Apsheronian. Forte et al., (2015a) divided the section into five units, which from oldest to youngest are: (S1) a 220 meter basal unit of interbedded conglomerate and coarse sandstone interpreted as a braided fluvial environment or alluvial fan; (S2) a 300 meter unit dominated by mudstone with large, tabular, and distinctively red sandstone horizons interpreted as a shallow lacustrine and/or near shore environment; (S3) a 390 meter package of interbedded sandstone and mudstone with abundant channels interpreted as meandering fluvial and overbank deposits; (S4) a 545 meter unit of coarse sandstone and conglomerate interpreted as a mixture of meandering and braid-plain environments; and (S5) a 590 meter unit of predominantly conglomerate with large clasts, suggestive of a braided or alluvial-fan environment. Here we present 7 samples from the Sarica section, including 2 (S-210 and S-1735) that we analyze for detrital zircon U-Pb ages. A subset of the U-Pb age population for S-210 was presented by Forte et al., (2015a) to constrain maximum depositional age for this sample.

3.3 Xocashen

The Xocashen section is located in western Azerbaijan, south of Sarica and north of the Mingechevir Reservoir (Figures 1 and S3). The section is within a fold and is a composite of three distinct measured sections: a short (145 meter) one measured in the forelimb of the fold (Xocashen-1), the main (890 meter) one measured in the backlimb of the Xocashen fold (Xocashen-2), and an additional (235 meter) section that is also in the backlimb but measured ~5.5 km to the west (Xocashen-3). Forte (2012) describes all three sections in detail while van Baak et al., (2013) investigates Xocashen-2 and van Baak et al., (2010) studies Xocashen-3, and report both summary descriptions and either complete (Xocashen-2) or partial (Xocashen-3) magnetostratigraphic records. Xocashen-2 and Xocashen-3 are directly correlative, based on both magnetostratigraphy (van Baak, 2010; van Baak et al., 2013) and tracing in the field between the two sections a distinctive blue mudstone horizon (unit XB) that is interpreted as the base of the Bakunian regional stage (van Baak et al., 2013). Based on the mapping and interpreted structural geometry of the Xocashen fold presented in Forte (2012), Xocashen-1 is stratigraphically below Xocashen-2 and Xocashen-3, although the exact thickness of the intervening stratigraphy separating these two is unconstrained. Magnetostratigraphy from van Baak et al., (2013) suggests that Xocashen-2 spans from the Apsheronian to Bakunian. Prior mapping (Ali-Zade, 2005; Forte, 2012) indicates that Xocashen-1 is likely fully within the Akchagylian.

Forte (2012) divided the composite Xocashen-1 and Xocashen-2 sections into 4 units, from oldest to youngest: (X1) the 145 meters of stratigraphy within Xocashen-1, which consists predominantly of dark blue mudstone that coarsens upwards to coarse sandstone and is interpreted as being deposited in a deep lacustrine/marine setting; (X2) a 570 meter unit at the base of the Xocashen-2 section that is predominantly mudstone with minor sandstone and occasional thin dark blue mudstone horizons interpreted as a shallow lacustrine environment; (XB) a thin (20 meter) distinctive blue mudstone horizon that is correlative with a similar horizon in the Xocashen-3 section and is interpreted as a temporary return to deeper lacustrine/marine conditions; and (X3) a 295 meter interval of sandstone and mudstone with a broadly upwards-coarsening trend. Here we present 5 provenance samples from the Xocashen, 1 collected from the Xocashen-1 section and the remaining 4 from within the Xocashen-2 section. Additionally, we report tephra geochemistry for 3 ash samples from the Xocashen section, 1 collected from Xocashen-2 (X-2A), and 2 collected from Xocashen-3 (X-3A and X-3B). Sample X-2A was collected from ~1.2 m from the base of a moderately consolidated 1.6 meter thick ash horizon with alternating horizons of more massive and pumice rich subhorizons (Figue S7d, S7e). Ash X-3A was collected from within 50 cm of the base of an ~3 m thick, well consolidated ash horizon with occasional, meter scale cross beds (Figure S7f). The sample of ash X-3B was collected from the base of ~0.5 meter thick moderately well consolidated ash horizon ~110 m stratigraphically above ash X-3A (Figure S7h) Based on stratigraphic height below the distinctive XB unit and an assumption of relatively similar sedimentation rates in Xocashen-2 and Xocashen-3, ash X-2A was correlated in the field with ash X-3B, implying that ash X-3A, which is several meters thick (e.g., Figure S7), was not present in the main Xocashen-2 section.

3.4 Bozdagh

The Bozdagh section and fold are also located in western Azerbaijan, due south from Xocashen and across the Mingechevir Reservoir (Figures 1 and S4). The 1010-meter-long Bozdagh section is described by Forte (2012) and is completely within the Apsheronian, based on prior mapping (Ali-Zade, 2005; Forte, 2012). The entire section consists of interbedded mudstone and sandstone with abundant terrestrial fossils - e.g., leaf impressions, coalified branches, mammal fossils - and primary features indicative of a deltaic environment - e.g., foresets and topsets, mud drapes, and mud rip-ups. Forte (2012) divide the section into three units, primarily on the relative fraction of sandstone to mudstone and changes in paleocurrent direction, but the depositional character of the units are all broadly similar. From youngest to oldest, the units are: (B1) a basal, 285 meter, sandstone-rich interval with predominantly south-directed paleocurrents; (B2) a 480 meter, mudstone-dominated layer with predominantly north-directed paleocurrents; and (B3) an upper 245 meter, sandstone-dominated interval with mixed north- and south-directed paleocurrents. Forte (2012) interpreted the switching paleocurrents within the section to represent meandering and/or lobe switching within a delta, as opposed to wholesale changes in rivers flowing into this area, given the deltaic nature of the section and its central position within the Kura Basin. We identified and sampled three different ash horizons: B-A at the top of unit B2 is a ~1 m thick, relatively friable horizon with evidence of significant weathering; B-B is in unit B3, ~35 meters stratigraphically above B-A (e.g., Figure S7), and comprises a well-indurated tephra nearly 5 meter thick; and B-C near the top of unit B3 and the section is only a few cm thick and appears to be significantly reworked. Here we present 4 provenance samples from this section, including 2 samples analyzed for detrital zircon U-Pb geochronology (B-280 and B-875). In addition we report tephra geochemistry from ash B-B. Samples were collected from all three ash horizons, but B-A did not yield usable material and the sample volume of B-C that was readily identifiable as being part of the ash horizon was insufficient to process.

3.5 Goy

The Goy section was measured along the Goy River in central Azerbaijan and originally described by Forte et al., (2013). Lazarev et al., (2019) subsequently revisited and extended the section, and both defined a different set of units and acquired magnetostratigraphy. Here we focus on the stratigraphy of the original 1790-meter-thick section described by Forte et al., (2013), as this corresponds with the extent of our provenance samples. However, we include the magnetostratigraphic results from the whole Goy section when correlating between sections (see section 5.2). Based on biostratigraphy and prior mapping (e.g., Ali-Zade, 2005), Forte et al., (2013) consider the Goy section to be restricted to the Apsheronian, but the later magnetostratigraphy from Lazarev et al., (2019) indicates that the section spans from the Akchagylian to the Apsheronian. Forte et al., (2013) define three units within the Goy section mainly based on regionally mappable units as opposed to distinct depositional sequences present in the measured section. Here, we subdivide the original G2 unit from Forte et al., (2013) into three sub-units to describe in more detail the changes in depositional environment and to improve consistency with the units defined by Lazarev et al., (2019), although our units still do not correspond perfectly. From oldest to youngest, the units used here are: (G1) a basal 675 meter interval dominated by mudstone and interpreted to reflect deposition in a deep lacustrine to marine environment (directly equivalent to G1 of Lazarev et al., (2019)); (G2-A) a 175 meter sandstone-siltstone sequence that is separated from G1 by an angular unconformity and is interpreted as a shallow lacustrine or marine environment (directly equivalent to unit G2 of Lazarev et al., (2019)); (G2-B) a 550 meter interval of sandstone with minor mudstone horizons that represents a mixed environment between a meandering fluvial and braid plain (roughly equivalent to the bottom half of unit G3a of Lazarev et al., (2019)); (G2-C) a 355 meter unit of mudstone with isolated bodies of sandstone and abundant plant fossils and coal horizons, interpreted as a shallow lacustrine, most likely swampy, environment (roughly equivalent to the upper half of unit G3a of Lazarev et al., (2019)); and (G3) a 35 meter unit of sandstone and conglomerate interpreted as a mixture between meandering and braided fluvial (roughly equivalent to the base of unit G3b of Lazarev et al., (2019)). Here we present provenance results from 5 total samples within the Goy section, including 1 sample for which we analyze detrital zircon U-Pb (G-200). One sample (G-175) was only used for point counts. In addition, we report tephra geochemistry for 1 ash sample (G-A) from the Goy section plus 3 different ash horizons within the area mapped by Forte et al., (2013). Ash G-A is ~35 cm thick in total with a basal ~17 cm section of unconsolidated light ash with isolated biotite crystals overlain by alternating thin (1-2 cm) layers of intercalated mudstone and mafic rich layers, followed by a final ~10 cm layer of mudstone with interbedded pumice clasts. The analyzed sample comes from the basal 10 cm section. The sample from Ash TG, from within the area mapped by Forte et al., (2013), was collected from a steeply north dipping ~15 cm thick white unconsolidated ash horizon overlain by a ~20 cm thick, more crystal rich darker horizon. Ashes WQ-A and WQ-B were both collected from a nearly horizontal fill terrace. Both ashes were distinctively white, unconsolidated and only a few cm thick. They were separated from each other by ~30 cm where WQ-B overlies WQ-A.

3.6 Other Samples for Characterizing Sediment Sources

The 13 samples of modern stream sediment (Figure 1) typically comprised >4 kg of medium- to coarse-grained modern river sand collected from the active channel at locations chosen to characterize particular source terrains within the adjacent mountain ranges. The source areas include the Greater Caucasus Paleozoic core (Enguri), Jurassic-Cretaceous Greater Caucasus Basin sediments (Aragvi, Zaqatala, Kumuk, Kish, and Damiraparan), Dzirula Massif (Kvirila), Achara-Trialet and western Lesser Caucasus (Mtkvari, which is the upstream equivalent of the Kura), and Lesser Caucasus Arc (Tovuz, Shamkir, and Zayam). Where applicable, samples were collected up-stream of major dams (e.g., Enguri). For these samples, we present bulk geochemistry as described in the methods section below. Detrital zircon U-Pb age populations for four of these rivers (Enguri, Kumuk, Mtkvari, and Tovuz) were presented by Cowgill et al., (2016). For the 11 volcaniclastic samples from the Vandam, we present bulk geochemistry for all and point counts for a subset (6). A detrital zircon population was published for one of these samples (AB0862 = SEGC) by Cowgill et al., (2016).

4. ANALYTICAL METHODS

We apply a variety of methods to the provenance samples, including point counts, bulk sediment/rock major and trace element geochemistry, and detrital zircon geochronology (Table 2). Additionally, we use major element chemistry of glass shards isolated from ash horizons to refine stratigraphic correlations between the sections and allow us to better track temporal and spatial changes in provenance within the Kura Fold-Thrust Belt (Table 3). This section summarizes the sample types and analytical techniques, Section 5 presents the statistical frameworks within which we analyze each different dataset, and Section 6 presents our results. For both the presentation of methods and results, we focus first on the volcanic glass geochemistry as this is critical for establishing the stratigraphic correlations, which in turn are necessary for presenting and interpreting the provenance results.

4.1 Major Element Geochemistry of Volcanic Glass

Major element fingerprinting of volcanic glass shards within tephra deposits is a useful stratigraphic correlation tool (e.g., Lowe, 2011; Lowe et al., 2017). For this study, geochemical analyses were conducted on volcanic glass shards (125-250 µm) manually separated from 8 tephra samples collected from locations throughout Georgia and Azerbaijan, and additional 9^{th} sample (B-A) from Bozdagh did not yield any usable glass shards. Five of the samples came from measured sections described previously, where as the other three (TG, WQ-A, and WQ-B) were collected in similarly aged units in the eastern Kura Fold-Thrust Belt mapped by Forte et al., (2013), which we include largely for reference for future work in this region. Locations of the samples are provided in Table 3. All tephra samples were separated and cleaned following common tephra preparation procedures (e.g., Roman et al., 2008). Specifically, samples were first wet sieved at Arizona State University (ASU) using 20-40-60-80 mesh sieves. The 40-60 mesh fractions were washed with 5% nitric acid to remove any carbonates, rinsed with deionized (DI) water, and then washed with 5% hydrofluoric acid (HF) one to three times, in 2-minute ultrasonic baths to remove clay adhering to the glass shards. Glass shards were then mounted in epoxy rounds, polished, and carbon coated for analysis in an electron microprobe.

Individual glass shards were analyzed for major element oxide abundances (SiO_2, Al_2O_3, K_2O, Na_2O, CaO, MgO, MnO, Fe_2O_3 and TiO_2) using a JEOL JXA-8530F Electron Probe Microanalyzer (EPM) with the JEOL software in the John M. Cowley Center for High Resolution Electron Microscropy at ASU. Using wavelength-dispersive spectrometry (WDS), the instrument was operated at 15 kV, with a 10 nA beam current and a 15 µm defocused beam to minimize alkali loss (Froggatt, 1992; Lowe, 2011). All data were adjusted using atomic number (Z), absorption (A), and fluorescence (F) corrections. If possible, 20 or more glass shards were analyzed for each sample. To assess analytical precision, the Lipari glass INTAV standard (Kuehn et al., 2011) and the Los Posos Rhyolite (RHY5) in-lab standard were run at the start, end and after every 40-60 unknown analyses.

Major element analytical results are reported as un-normalized data averages with 1σ standard deviation error (Table 3). Brief descriptions of the glass and crystals (if present) are also provided in Table 3. Individual shard analyses are reported in the supplement (Table S1). Individual analyses with totals <90% or with otherwise anomalous values (e.g., SiO_2 > 90%) were not included in the averages or later statistics but are still reported in the supplement. Low totals can be a result of alteration (potential leaching) or analytical issues and are not viable for considering stratigraphic correlations.

4.2 Sandstone Composition

Point counting is a well-established method for determining the composition of siliciclastic sediments (particularly sandstone) and for the classification of rock type, tectonic setting, and provenance (e.g., Dickinson, 1970; Dickinson and Suczek, 1979; Ingersoll et al., 1984; Ingersoll, 1990). Here, sandstone compositions for 26 of the total 27 Kura Basin sandstones from within measured sections and 6 samples of Mesozoic volcaniclastic rocks in the Vandam zone were determined through a modified approach towards point counting (Table 4, S2). All but one of the Kura Basin sandstones (G-175) have corresponding bulk-rock geochemistry (described in the next section) determined from the same samples. Rather than use standard optical techniques (e.g., Dickinson, 1970), we follow other workers (e.g., Vortisch et al., 2003) in using an electron microprobe to perform the point counts, which allowed for more detailed characterization of the minerals present and the individual components of lithic clasts than possible with traditional optical techniques. We performed point counts using a Cameca SX-100 Electron Microprobe at the University of California, Davis. A minimum of 115 grains were analyzed in each sample and mineral identifications were made via inspection of energy-dispersive spectra (EDS). Grains were selected using a modified grid analysis where the spacing of the grid varied depending on the sample to accommodate differences in grain size and amount of cementation. To aid in identification, EDS results from unknowns were compared against spectra of standards for particular mineral species. During the analysis, a new category was created for each unique grain type, leading to 345 different categories of minerals and lithics (Table S2). These categories were consolidated to 10 summary categories: calcium rich plagioclase, pyroxene and amphibole, volcanic lithic, albite, potassium and alkali feldspar, general lithics, quartz, sedimentary lithic, carbonate, and other (Table 4). These categories were developed to highlight specific variations observed between samples. Lithic grains were classified as sedimentary or volcanic lithics if they retained a primary texture clearly identifiable as either sedimentary or volcanic. Other lithic grains that lacked clear textural indications were classified as general lithics, which mostly represent either metamorphic or igneous grains. Grains classified as “other” include a wide variety of mono-mineralic grains including various phyllosilicates, accessory minerals such as iron or titanium oxides, barite, pyrite, apatite, zircon and alteration minerals such as chlorite and epidote.

4.3 Sandstone Major and Trace Element Composition

Bulk-rock geochemistry of clastic sediments is used in a wide array of different applications including investigations of the bulk geochemical evolution of the Earth (e.g., Taylor and McLennan, 1985; McLennan and Taylor, 1991; Plank and Langmuir, 1998; McLennan, 2001), evaluating the degree of weathering of source terrains (e.g., Nesbitt and Young, 1982; McLennan, 1993; Fedo et al., 1995; Alvarez and Roser, 2007; Ohta and Arai, 2007; Li and Yang, 2010), classifying the tectonic setting of sediments (e.g., Bhatia, 1983; Bhatia and Crook, 1986; Herron, 1988), and provenance analysis (e.g., Bonjour and Dabard, 1991; Totten et al., 2000; Von Eynatten, 2003; Von Eynatten et al., 2003). It has been suggested that major and trace element geochemistry of bulk-sediments provides a means of discerning provenance that is less biased by effects of chemical alteration and weathering than traditional light element analysis (e.g., Dickinson, 1970) and effects of hydraulic sorting that may influence heavy mineral data and related geochronologic techniques (e.g., Von Eynatten et al., 2003; Pe-Piper et al., 2008).

We analyzed 26 of the total 27 sandstone samples for bulk-rock geochemistry. For all but one sample (G-200), these were the same sample material analyzed for point counts. Interior sections of samples (e.g., removing weathering rinds for sandstones) were selected and ~200 grams of each sample was sent to Activation Laboratories Ltd. where they were crushed and analyzed according to their Code 4Lithoresearch and Code 4B1, which follow protocols similar to those used by Pe-Piper et al. (2008) and yields concentrations for 44 different elements in total (Table S4). In particular, major-and trace element concentrations were measured using lithium metaborate/tetroborate fusion ICP analysis and ICP-MS analysis, respectively.

4.4 U-Pb Detrital Zircon Ages

U-Pb geochronology of detrital zircons is a common and versatile tool for assessing the provenance of siliciclastic sediments (e.g., Fedo et al., 2003; Andersen, 2005; Gehrels, 2012). U-Pb geochronology of individual detrital zircons from samples of seven Kura Basin sandstones were measured by laser ablation multi-collector inductively coupled plasma mass spectrometry (LA-MC-ICPMS) at the Arizona LaserChron Center. Analytical procedures relevant for the time period when these samples were analyzed (2011) are described by Gehrels et al. (2006) and Gehrels et al. (2008). Approximately 110 grains were dated per sample. Because the potential existed for observing young grains (<10 Ma) in many of the samples, a 20 second integration time was used for all samples. Analyses were excluded from plots and statistical treatments based on unacceptable discordance, precision, or in-run fractionation. For extremely young grains (<10 Ma), discordance was largely ignored in choosing whether to include or exclude particular analyses because the calculated $^{206}Pb/^{207}Pb$ for these grains are subject to extremely low precision due to the low concentrations of ^{207}Pb (Gehrels, 2012). Complete analyses are presented in the supplement (Table S5)

To consider potential sources for the Kura Basin DZ samples, we also define composite source populations based on the classification from Tye et al., (2020) as described in section 2.3, against which to compare the basin samples. In detail, to define a composite source population, we combined available published DZ age populations from individual samples into a single, composite sample. We use the same set of samples as Tye et al., (2020), including those from Allen et al. (2006), Wang et al., (2011), Vincent et al., (2013), Cowgill et al., (2016), Trexler et al., (2022), Vasey et al., (2020), and Tye et al., (2020), but supplement with additional samples reported by Forte et al., (2022a). For the samples from Forte et al., (2022a) not classified by Tye et al., (2020), we use multidimensional scaling (Vermeesch, 2013) to assess to which source samples, and by proxy which composite source terrane, these newer samples are most similar. Multidimensional scaling plots suggest that all of the the Forte et al., (2022a) samples are best classified as part of the GCSL composite source. Table 5 lists the samples used from these sources and to which source terrain they are assigned. We also follow Tye et al., (2020) in defining 6 distinct age populations within both the composite sources and basin samples discussed previously.

5. STATISTICAL TREATMENT OF ANALYTICAL RESULTS

5.1 Volcanic Glass Major Elements

In our treatment of the major element data for the volcanic glasses, we primarily follow recommendations from Lowe et al., (2017). Specifically, we explore potential correlations with plots of log-ratios of various major elements pairs, and select one set (CaO/Al_2O_3 and TiO_2/Fe_2O_3) that provided meaningful separation of different tephra beds or components. Prior to plotting, rounded zeroes (quantities measured but present in amounts below the detection limit) were replaced by nonparametric imputation as described by Martín-Fernánez et al., (2003) using the CoDaPack software package (Comas-Cufí and Thió-Henestrosa, 2011). We compare this with the results of a principal component analysis (PCA), a technique for reducing dimensionality (Krzanowski, 2000), applied to all of the major oxides. Prior to PCA, the oxide concentrations are normalized using a standard scaler so that data are normally distributed with a zero mean and unit variance (Lowe, 2011; Lowe et al., 2017).

We also estimate the similarity of the tephras via a modified Euclidean distance measure, D^2, defined by Perkins et al (1995) where,

$$D^2 = \sum_{k=1}^{n} \left[\frac{(x_{k1} - x_{k2})^2}{2\sigma_k^2} \right]$$

and x_{k1} is the concentration of element x_k in the glass of tephra 1, x_{k2} is the concentration of element x_k in the glass of tephra 2, σ_k is the analytical precision of element x_k, and n is the number of elements used in the comparison. We refer to this modified Euclidean distance measure as the "Perkins Distance”. Here we select five of the major oxides, CaO, Fe_2O_3, MgO, MnO, and TiO_2, for this distance calculation. We follow Perkins et al., (1995) and do not include Al_2O_3 and SiO_2 in this calculation because they do not show much variation for the majority of samples and could bias the distance measures. Similarly, we exclude Na_2O and K_2O from the calculation because the concentrations of these elements are sensitive to post-depositional hydration of glass shards. Calculated D^2 measures have a chi-squared distribution, and thus with five elements (five degrees of freedom), two tephras can be considered statistically different at the 95% and 99% confidence levels if D^2 exceeds 11.1 and 15.1, respectively. Correspondingly, D^2 less than these critical values suggest that the respective tephras may be correlative. We report the D^2 values in Table 6.

5.2 Sandstone Major and Trace Elements

Numerous methodologies have been proposed for the use of geochemical data from siliciclastic sediments to establish their tectonic setting or specific provenance. Many early attempts focused on descriptive statistics with the selection of useful pairs or triads of either single elements or element ratios in discriminating source regions or tectonic settings (e.g., Bhatia, 1983; Bhatia and Crook, 1986; Roser and Korsch, 1986; Herron, 1988; Bonjour and Dabard, 1991; Totten et al., 2000). These discrimination diagrams are useful tools for initial data exploration. However, many of them have been shown to be relatively inaccurate in classifying samples when tested using sediments of known provenance or tectonic setting (e.g., Armstrong-Altrin and Verma, 2005). As an alternative to simple bi-plots or ternary diagrams, the numerous elements characterized in a standard geochemical analysis are well suited for multivariate statistics performed on a suite of elements, and may provide more robust discrimination techniques (e.g., Roser and Korsch, 1988). However, as first recognized by Aitchison (1986), compositional data are subject to a constant-sum constraint and thus must co-vary because they are restricted to values between 0 and 1 (or 100%). This constraint violates a fundamental assumption of many multivariate techniques, which is that the values follow a multivariate normal distribution (e.g., Von Eynatten et al., 2003). In response, Aitchison (1986) proposed two different transformations that effectively remove the constant-sum constraint and make compositional data suitable for multivariate analysis. The first transformation is the additive log-ratio (ALR), which is calculated by normalizing all of the measured values by one of the measured values and then taking the natural log of the resultant ratios. The second transformation is the centered log-ratio (CLR), which is calculated in the same manner as ALR but is instead normalized by the geometric mean of all of the parts involved. However, both ALR and CLR introduce additional restrictions that make them unsuitable for certain multivariate statistics (e.g., Pawlowsky-Glahn and Egozcue, 2006). In response, the isometric log-ratio (ILR) transformation was developed to fully convert compositional data into values suitable for any standard multivariate technique (Egozcue et al., 2003). However, the ILR transformation has a tradeoff: while values transformed into ALR or CLR coordinates are still easily interpretable in terms of the original measured values, that is not the case for those converted to ILR coordinates (e.g., Egozcue et al., 2003; Egozcue and Pawlowsky-Glahn, 2005). Because all of the above techniques have both strengths and weaknesses, we explore the geochemical data using multiple different descriptive and multivariate statistical techniques.

First we use bi-plots to characterize the variability of both the samples with unknown provenance within the Kura Basin and the samples that we use to help characterize the source areas (e.g., the modern river sediment and Mesozoic volcaniclastic rocks of the Vandam). As with the glass data above, rounded zeroes were replaced by nonparametric imputation prior to plotting. A version of Table S3 with replaced zeros is also provided in the supplement (Table S4).

We construct the bi-plots using elemental ratios previously identified as being useful in discrimination of either provenance or tectonic setting, specifically the ratios La/Sc, Ti/Nb, Th/Sc, Cr/Th, La_N/Yb_N, and Eu/Eu*. The La/Sc ratio is used by Bhatia and Crook (1986) and tracks compatibility, with high values (enriched in La relative to Sc) suggesting a higher concentration of incompatible elements and hence a more evolved sediment source. The Ti/Nb ratio was used by Bonjour and Dabard (1991) to discriminate between more basic/mafic (high Ti/Nb) and more acidic/felsic (low Ti/Nb) sources. Totten et al. (2000) suggested the use of the Th/Sc and Cr/Th ratios together as indicators of compatibility, with samples characterized by high Th/Sc and low Cr/Th being representative of more continental (evolved) sources and low Th/Sc and high Cr/Th suggesting more mafic sources. For these four elemental ratios, we consider their natural log, thereby converting them to log-ratios sensu Aitchison & Greenacre (2002) because doing so makes graphical interpretation of their relations more clear (e.g., Thomas and Aitchison, 2006). La_N/Yb_N and Eu/Eu* are used by Bhatia (1985). La_N/Yb_N compares values of La and Yb normalized to the respective values for these two rare earth elements in chondrites and indicates relative enrichment in either light rare earth elements (high La_N/Yb_N) or heavy rare earth elements (low La_N/Yb_N). The Eu/Eu* ratio is effectively a measure of the size of the Eu anomaly, with values around 1 indicating no significant Eu anomaly and values less than 0.85 indicating significant Eu depletion (e.g., Taylor and McLennan, 1985). Because both the Eu/Eu* and La_N/Yb_N are commonly reported values, we have not converted these to log-ratios for ease of comparison. Values for the plotted element ratios or derivatives are provided in Table 7.

Second, we use multivariate statistics to conduct two separate analyses using two different suites of elements. The first is a suite of 17 trace elements (Sc, V, Cr, Co, Ni, Rb, Sr, Y, Zr, Nb, La, Gd, Yb, Hf, Ta, Th, U) and one oxide (TiO_2), which is suggested by Pe-Piper et al. (2008) to provide a good discrimination of source geochemistry in detrital samples. The second suite is a set of 10 major elements (SiO_2, Al_2O_3, Fe_2O_3(T), MnO, MgO, CaO, Na_2O, K_2O, TiO_2, and P_2O_5 and excluding LOI, loss on ignition), which is another suite used by Pe-Piper et al. (2008). As noted below, the second suite was not useful. For both suites, rounded zeroes were replaced in the same manner as for the glass geochemistry and bi-plots using the CoDaPack software, which was also used to transform the compositions into isometric log-ratios (ILR) suitable for multivariate analyses (Table S4). Because our main goal is to understand the relations between the samples, rather than the relations between the measured components, the ILR ratio is suitable even though it is not possible to relate the ILR coordinates to specific measured values. For this reason, we do not report loadings for the various multivariate analyses performed as they do not provide useful information.

To characterize variability and evaluate potential populations within the source terrains, we analyzed the ILR transformed compositions for the major and trace element groups of the modern river sediments and Vandam volcaniclastic rocks using hierarchical clustering analysis and principal component analysis. These methods have previously been applied to geochemical investigations of provenance data and are useful for understanding potential groupings (e.g., Smosna et al., 1999; Pe-Piper et al., 2008). Hierarchical clustering essentially evaluates the "closeness" of given samples to each other and the results are typically represented graphically on a dendrogram (Krzanowski, 2000). Principal component analysis is a technique for reducing dimensionality (Krzanowski, 2000) and can also be evaluated graphically, with similarity being indicated by a grouping on a plot of the principal component (Pe-Piper et al., 2008). We performed both the hierarchical clustering and principal component calculations in the "R" software package (Team, 2010), using the "pvclust" library (Suzuki and Shimodaira, 2009) in the hierarchical clustering analysis to generate a dendrogram with boot-strapped p-values (Shimodaira, 2004) to provide an estimation of the robustness of the clusters indicated on the dendrogram. In detail, we used the "Ward" method of clustering and the "Euclidean" distance. In both the cluster analysis and principal component analysis, the suite of major elements did not prove useful in discriminating different populations and in the case of the principal component analysis failed to capture significant portions of the data variance, so these results are not presented, and the major elements set were not used in future analyses.

Thirdly, we used the results of the hierarchical clustering analysis and principal component analysis using the suite of trace element data to inform choices of groups for linear discriminant analysis to classify the unknown samples from the Kura Fold-Thrust Belt. Unlike both hierarchical clustering and principal component analysis, which do not require any a priori assumptions about the relation between samples, linear discriminant analysis is a guided machine learning approach that uses a set of training data divided into known groups to calculate the initial linear discriminant functions (Krzanowski, 2000). These functions are then used to classify unknowns as members of one of these preset groups. We completed these calculations in the "R" software using the "MASS" library (Venables and Ripley, 2002). The modern sediments and Vandam volcaniclastic rocks were used as the training dataset to calculate the linear discriminant functions. Multiple discriminant functions were calculated, using the ILR transformed compositions with different group assignments, which are described in more detail in the results section. To assess the robustness of each set of discriminant functions, cross-validation was performed where iteratively the discriminant functions are re-calculated with one sample from the training data excluded. This sample is then classified according to the calculated discriminant function and the overall percentage of correctly classified training data provides an indication of the robustness of the chosen groups and the accuracy of the functions. Finally, the Kura Fold-Thrust Belt samples were classified using the calculated linear discriminant functions.

5.3 Weathering Indices

Chemical weathering can impact the major element composition of siliciclastic sediment (e.g., Nesbitt and Young, 1982; McLennan, 1993; Fedo et al., 1995). Although this is why many of the geochemical provenance methods we apply focus on trace elements (e.g., Pe-Piper et al., 2008), it is still useful to consider the extent to which weathering may have impacted the fidelity of the geochemical provenance methods (e.g., Chen and Robertson, 2020). One way to assess weathering extent is through the use of quantitative indices that broadly compare the concentration of mobile elements (e.g., Ca^{2+}, Na^{+}, K^{+}) relative to relatively more immobile elements (e.g., Al^{3+}). For the Kura Fold-Thrust Belt samples, we consider three different weathering indices using the major elements, specifically the chemical index of alteration (CIA - Nesbitt and Young, 1982), chemical index of weathering (CIW - Harnois, 1988), and plagioclase index of alteration (PIA - Fedo et al., 1995). All of these were calculated after converting weight percent to number of moles of the corresponding oxides. All three indices include the silicate portion of CaO, denoted CaO*, which requires removing portions of the CaO weight percent that reflect contributions from apatite, calcite, and dolomite. Typically, the weight percent of P_2O_5 is used to estimate and remove the apatite contribution and CO_2 is used to estimate and remove the calcite and dolomite components (e.g., Fedo et al., 1995). In our case, we have analyses of P_2O_5 and so can apply the standard apatite correction, but the analyses did not measure CO_2. Instead, we use a method suggested in McClennan (1993) where after apatite correction, if the number of moles of CaO* is greater than Na_2O, the number of moles of Na_2O is used instead as the value of CaO* in the calculation of the weathering index. Values of CaO* are reported in Table 7.

5.4 Detrital Zircon U-Pb Ages

Multiple approaches have been developed for filtering, displaying (e.g., Vermeesch, 2012), and comparing (e.g., Saylor and Sundell, 2016) populations of detrital zircon U-Pb ages, all of which continue to be the subject of vigorous discussion. For visualizing age distributions, we plot both probability distribution plots (PDPs) and kernel density estimates (KDEs), because both have distinct advantages and disadvantages. We use the "densityplotter" software (Vermeesch, 2012) to generate both the PDPs and KDEs for our new samples and the composite sources. We use three different methods to compare the U-Pb ages from our new basin samples with those from potential source terrains: multidimensional scaling (MDS) plots (Vermeesch, 2013), monte-carlo unmixing models (Sundell and Saylor, 2017), and Bayesian population correlation (BPC) (Tye et al., 2019). In the following we briefly review the premises underlying each approach, with a focus on interpretation of their outputs. For details, we refer interested readers to the individual papers that establish each method.

MDS plots rely on an underlying matrix of pairwise dissimilarity metrics between individual samples - e.g., the D-value of a Kolmogorov-Smirnov test - which are used to produce either a 2D or 3D plot of this dissimilarity, where a single sample plots as a point and the relative proximity of points to each other on the plot provides a qualitative sense of similarity between samples, with closer points being more similar than those farther apart (Vermeesch, 2013). Here, we use the implementation of MDS plots in the "DZmds" Matlab routine (Saylor et al., 2018) to produce a 3D MDS plot for our basin samples and composite sources. For the underlying dissimilarity metric, we use the D-value of the KS test performed on PDPs calculated using the 1-sigma uncertainty values for individual ages.

Unmixing models use monte-carlo sampling of suites of candidate sources, i.e., the composite sources we assemble, to produce synthetic samples that are then statistically compared against unknowns, i.e., our fold-thrust belt samples, to find the mixture of candidate sources that are most statistically similar to a given unknown sample (Sundell and Saylor, 2017). We use the Matlab based "DZmix" from Sundell and Saylor (2017) to perform this unmixing. For each trial within DZmix, the program uses the sample with the smallest number of ages to define the size of the subsample to subsample all input distributions because differences in sample size are known to bias many of the dissimilarity tests (e.g., Saylor and Sundell, 2016). In our case, an unknown sample always has the smallest number of ages. For the subsampling, we use the default value of 50 subsamples per trial. As with the MDS plots, for unmixing models, a particular statistical dissimilarity test must be chosen along with the way of representing the detrital populations (i.e., either PDPs or KDEs) within the test. For this effort, we use PDPs calculated at the 1-sigma uncertainty level and consider unmixing models using the V-values of the Kuiper test, D-values of the KS test, and PDP cross-correlation (see Saylor and Sundell, 2016 for comparisons of these methods). For each sample and statistical test, we run 10,000 trials. For a given set of trials and a given underlying statistical test, the unmixing routine provides both an estimate of the fraction of individual sources that may have contributed to the unknown and the degree of similarity between the synthetic samples and the unknown sample. Note that the degree of similarity increases as values approach 0 for V (Kuiper) and D (KS) but 1 for PDP cross-correlation.

Finally, BPC relies on constructing probability model ensembles (PMEs) for each sample and then uses these PMEs in pairwise comparisons to calculate a degree of similarity, i.e., the BPC value (Tye et al., 2019). As shown by Tye et al., (2019), BPC is relatively insensitive to differences in sample size between samples being compared, removing the need for subsampling as is required with unmixing techniques. Output BPC values vary from 0 to 1, where a value near 1 implies a high degree of similarity. The BPC calculation also estimates uncertainty on these values.

6. RESULTS

6.1 Ash Correlations

Geochemically, 6 of the 8 analyzed ashes contain exclusively rhyolitic shards (Figure S6). Although the other 2 sample (B-B and X-3A), are dominated by rhyolite shards (Mode 1), they also contain secondary populations (Mode 2) that are somewhat geochemically diverse and distinctly lower in silica, having trachyte to trachyandesite compositions (Figure S6). Bi-plots of log ratios and PCA reveal four broad tephra groupings, one of which includes the Mode 2 shards (Figure 2). Key observations from the bi-plots and PCA for correlating the measured sections are: (1) tephras X-3B and X-2A within the two younger Xocashen sections are similar, consistent with other stratigraphic correlations based on the Apsheron-Baku boundary in both sections (van Baak, 2010; van Baak et al., 2013) and (2) tephras X-3A in Xocashen, B-B in Bozdagh, and G-A in Goy are similar. Note that the pairs of Mode 1 and Mode 2 shards in X-3A and B-B also appear similar to each other, although the Mode 2 shards have significant scatter (Figure 2, S6). Although Mode 2 shards are absent from the sample of G-A tephra, we did observe in the G-A ash a distinctively more mafic interval that we unfortunately did not sample (Figure S7).

Outside of the measured sections, tephras WQ-A and WQ-B were both sampled from a single outcrop of unit Unit G3 in the Goy area (Forte et al., 2013), with WQ-A stratigraphically below WQ-B by ~40 cm. These two samples group with each other but are distinct from all other samples analyzed here, indicating they likely represent tephras from a third, distinct eruptive source. Tephra TG was collected from a thrust slice of Unit 2G in the Goy area and was assumed by Forte et al., (2013) to correlate with tephra G-A in the Goy section. However, the new geochemical data indicate TG correlates with tephra X-3B and X-2A in Xocashen, not with G-A.

For all the tephras, the correlations derived from the bi-plots are largely identical to those interpreted from statistical distance (Table 6). In detail, the statistical distance measure does not suggest that the more mafic mode 2 of tephras X-3A and B-B are correlative, but this likely reflects the relatively large variability in the geochemistry and small number of shards analyses, with only one shard from X-3A classified as mode 2.

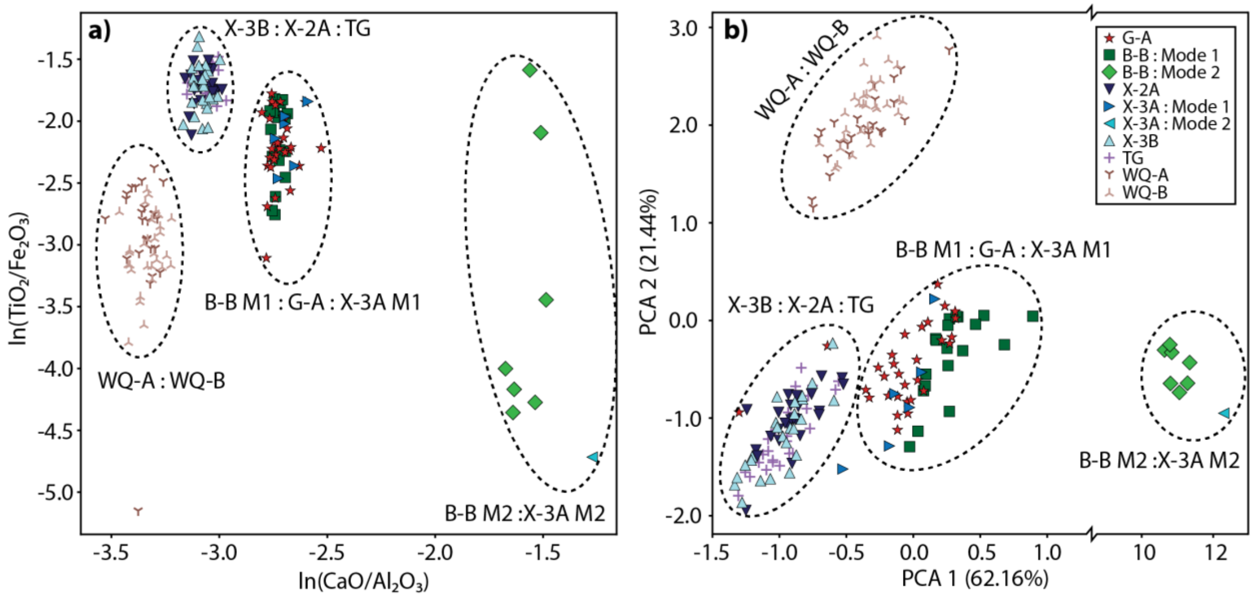

Figure 2 – Plots of tephra shards geochemistry. a) Plot of natural log of element ratios highlighting separation of different ash populations and emphasizing the existence of two modes within ashes X-3A and B-B. b) Plot of principal component analysis of ash shard geochemistry suggesting similar groupings as the log ratios. Notice a significant break in the x-axis, reflecting the extreme differences of mode-2 in both B-B and X-3A.

6.2 Stratigraphic Correlations

The new ash geochemistry establishes new ties between Xocashen, Bozdagh, and the Goy sections. Additionally, magnetostratigraphy in Xocashen (van Baak et al., 2013) and Goy (Lazarev et al., 2019) strengthen the correlations between these two sections. Combining these data with prior age calls from geologic mapping (Abdullaev et al., 1957; Ali-Zade, 2005; Forte, 2012) and biostratigraphy (Forte et al., 2013, 2015a; van Baak et al., 2013; Lazarev et al., 2019) allows us to correlate the different sections both to each other and the regional timescale (Figure 3). A summary of the key datasets informing our correlations are: (1) magneto- and biostratigraphy allow for direct correlation between Xocashen and Goy and both the regional timescale and global paleomagnetic timescale (van Baak, 2010; van Baak et al., 2013; Lazarev et al., 2019), (2) new ash geochemistry allow for direction correlation between portions of Xocashen, Bozdagh, and Goy (Figure 2), (3) maximum depositional ages from U-Pb ages of detrital zircons in Sarica and Vashlovani allow connection between the global absolute timescale and thus regional timescale (Forte et al., 2015a), and (4) mixtures of biostratigraphy, lithostratigraphy, depositional environment interpretations derived thereof and inferred relations to Capsian stages, allow for further correlation between stratigraphy in all sections and the regional timescale (e.g., Abdullaev et al., 1957; Ali-Zade, 2005; Forte, 2012; Forte et al., 2013, 2015a; van Baak et al., 2013; Lazarev et al., 2019). Below we consider specific correlations between units within the measured sections and their respective correlations to the Caspian regional timescale.

Based on these data, Vashlovani unit V1 correlates to the combined Meotian-Pontian period and does not correlate to any portions of the other sections. Vashlovani unit V2 and Sarica unit S1 correlate to the Productive Series and each other. Within Sarica, Forte et al., (2015a) previously used a small sub-population of zircons from sample S-210 near the top of unit S1 to determine a maximum depositional age (MDA) of 2.5 ± 0.24 Ma. Considering the uncertainty, this MDA is consistent with deposition during Productive Series time if the age of the Productive-Akchagyl boundary is 2.7 Ma as reported by Krijgsman et al. (2019), but it is inconsistent if the boundary is at 2.95 Ma as reported by Lazarev et al. (2021). Although resolving this question is beyond the scope of the present work, it does indicate that the exact position of the Productive-Akchagyl boundary in the Sarica section may be unclear. For our purposes, we assume that the entirety of S1 is within the Productive Series to be consistent with Forte et al., (2015a).

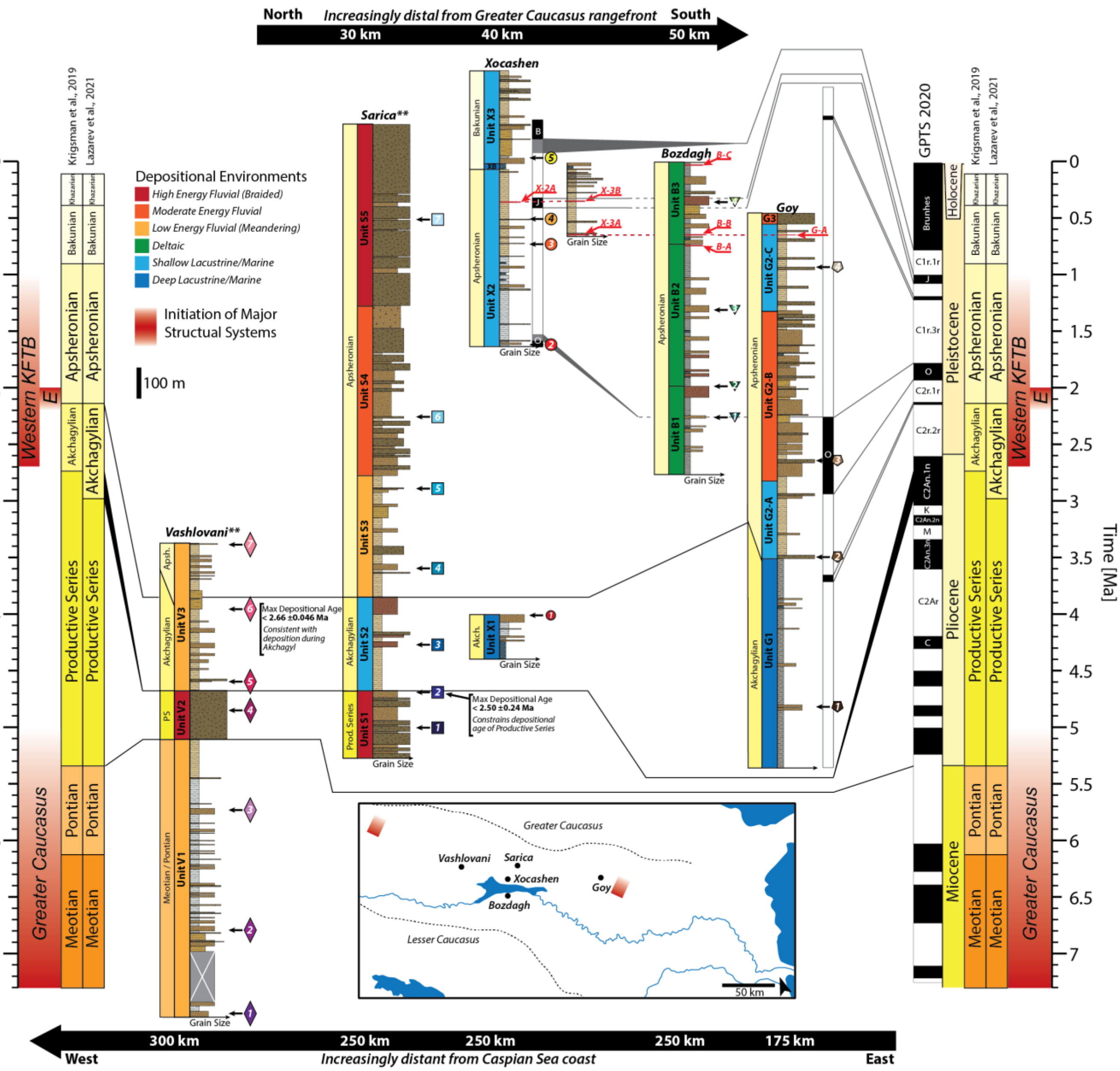

Figure 3 – Stratigraphic correlations of the measured sections based on ash geochemistry, published magnetostratigraphy (van Baak et al., 2013; Lazarev et al., 2019), and previous mapping (Abdullaev et al., 1957; Ali-Zade, 2005; Forte, 2012; Forte et al., 2015a). Colored symbols with numbers to the right of each column indicate samples analyzed here. Units within each section are colored by depositional environment as indicated in legend. Black lines show our correlations between the sections, the global

geomagnetic polarity timescale (GPTS - Ogg, 2020), and the regional timescales of Krijgsman et al. (2019) and Lazarev et al. (2021), which differ in Akchagyl duration. In Vashlovani and Goy sections the diagonal boundaries between Akchagylian and Apsheronian indicate uncertainty in the exact location of the boundary within the measured section. Inset map shows locations of stratigraphic sections (black dots) and areas (boxes with red gradients) where timing of the Kura Fold-Thrust belt initiation is constrained to the east (Forte et al., 2013; Lazarev et al., 2019) and west (Sukhishvili et al., 2020). Vertical bars with red shading indicate initiation ages of major structures in the region (E = Eastern KFTB).

Based on prior results from Forte et al. (2013, 2015a)The basal portion of unit V3 in Vashlovani, S2 in Sarica, X1 in Xocashen-1, and G1 in Goy all correlate to each other and the Akchagylian period. Forte et al., (2015a) previously reported a relatively large population of young zircon grains in sample V-1240 from Vashlovani unit V3, which they used to establish an MDA of 2.66 ± 0.046 Ma. At the time of publication of Forte et al., (2015a), the maximum depositional age corresponded to a long hiatus between the Akchagyl and Apsheron (van Baak et al., 2013), making it unclear if the sample was deposited during the Akchagyl or Aspheron. Subsequent work has refined the age of the Akchagyl-Apsheron boundary to 2.1 Ma (e.g., Krijgsman et al., 2019; Lazarev et al., 2021). Thus, the MDA from V-1240 is now consistent with deposition during either early- or mid-Akchagylian time, depending on which timescale is chosen.

The upper portion of Vashlovani unit V3, Sarica units S3-S5, Xocashen-2 unit X2, Bozdagh units B2-B3, and Goy units G2-A, G2-B, G2-C, and G3 all correlate to each other and the Aphseronian period. Although correlation between Xocashen ash X-3A and Goy ash G-A may seem problematic in light of the magnetostratigraphy results from these two sections, they are compatible when differences in sedimentation rates are considered. The apparent problem is that Xocashen ash X-3A is only ~90 meters below the interpreted base of the Jaramillo normal period, whereas Goy ash G-A occurs ~370 meters below the base of the Cobb Mountain normal subchron (which occurs ~150 ka before the Jaramillo), far below the base of the Jaramillo in the extended Goy section as measured by Lazarev et al., (2019) The correlation works however, because the average sedimentation rate in the upper part of the Xocashen section was only 0.4-0.9 m/ka, based on the magnetostratigraphy and uncertainty in the placements of the top of the Olduvai and base of the Jaramillo (van Baak et al., 2013), whereas the magnetostratigraphically derived sedimentation rate was ~1.68 m/ka in the upper section of Goy (Lazarev et al., 2019). Assuming that these are the same ash horizons (and thus have the same age), we can express the average sedimentation rate in Xocashen (r_1) between X-3A and the base of the Jaramillo chron as 90 m / t ,where t is the time in thousands of years between the deposition of the ash and the base of the Jaramillo, and the sedimentation rate in Goy (r_2) between the G-A and the base of the Cobb Mountain as 370 m / (t + 150). Solving for t gives us an expression between the two sedimentation rates and assuming the 1.68 m/ka rate for the upper section of Goy from Lazarev et al., (2019) suggests an average sedimentation rate of 0.78 m/ka in Xocashen. This value is within the range of section-averaged sedimentation rates at Xocashen, although it is on the higher end, suggesting that the ash based correlation is permissible with the existing magnetostratigraphy.

Finally, Xocashen-2 units XB and X3 correlate to the Bakunian period and are not directly represented in other sections. However, the upper bounds of the Apsheronian in both Sarica and Bozdagh are not well constrained. Thus, the upper parts of the Sarica and/or Bozdagh sections may be of Bakunian age, but we do not implement such a correlation here as we have no direct evidence.

6.3 Sandstone Composition

Complete counts of components within the Kura Basin sandstones and selected samples of Vandam volcaniclastic rocks are included in Table S2 and the distilled results from binning components into the broad categories described in the methods are reported in Table 4. Within the Kura Basin samples, relative abundance of components varies significantly, both between different measured sections and between samples within a single measured section (Figure 4). The most variable set of components were calcium-rich plagioclase, volcanic lithics, and pyroxene/amphibole. Although clinopyroxene dominates the pyroxene/amphibole category, various types of amphibole and both clino- and orthopyroxene are also present. Although calcium-rich plagioclase, volcanic lithics, and pyroxene/amphibole components are very abundant in some samples (e.g., S-90 or S-210), they are virtually absent in others (e.g., Xocashen and Goy sections). Results from analysis of Vandam volcaniclastic rocks suggest a relatively high proportion of clinopyroxene and both calcium-rich plagioclase and albite (Table 4). In the section that follows, we highlight some distinct variations within particular measured sections within the Kura Basin and the Vandam volcaniclastic rocks in the southeastern Greater Caucasus.

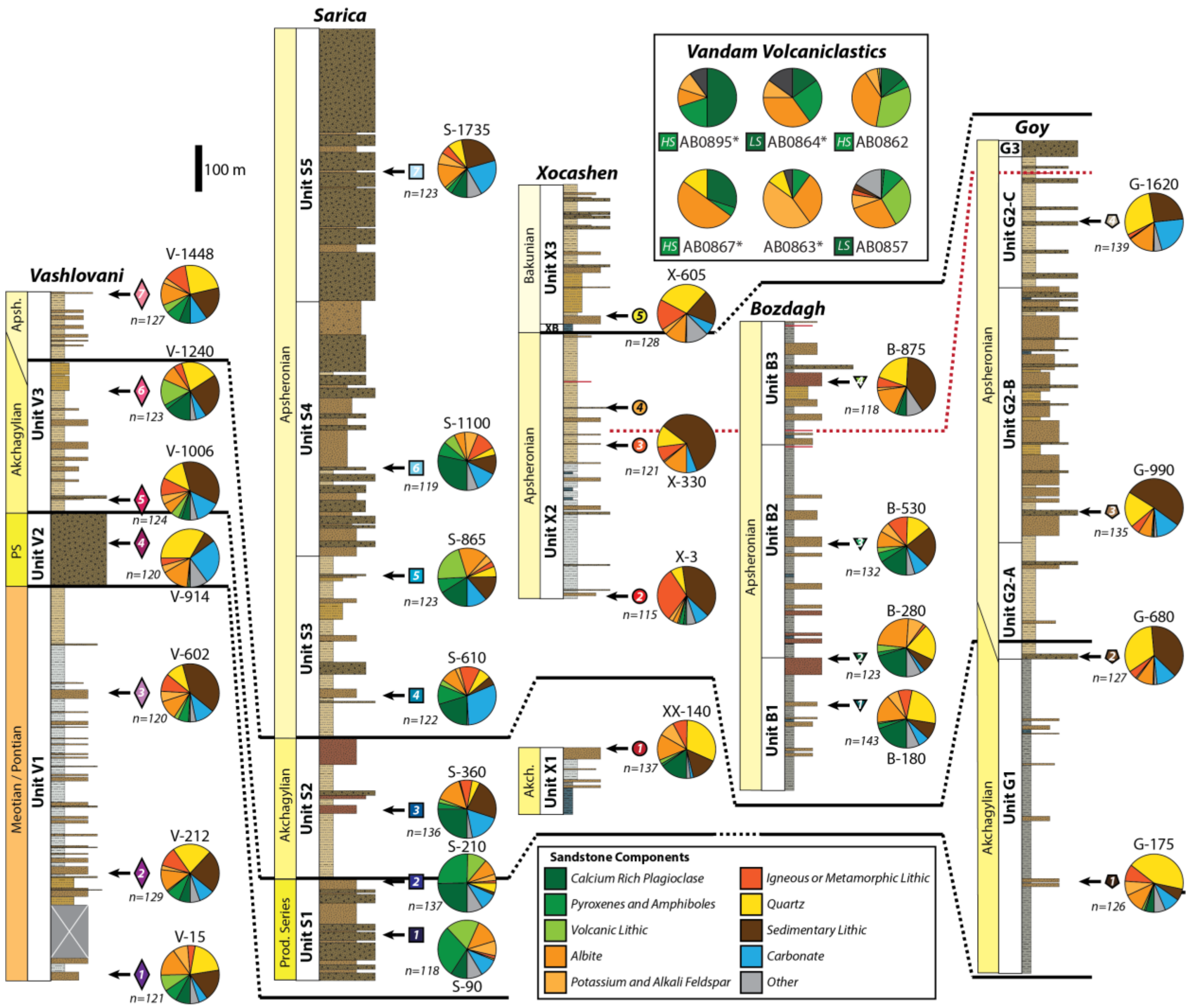

*Figure 4 – Sandstone point count results displayed as pie charts. Black lines indicate stratigraphic correlations from Figure 3; inset shows point count results from Vandam volcaniclastic rocks for comparison (HS = High Si group identified via geochemistry, LS = Low Si group identified via geochemistry, * = modal mineralogy instead of point counts).*

Within the Vashlovani section, the relative proportions of the different components do not change significantly, except for sample V-914 (Figure 4), which is from a small sand bed within a distinctive, thick package of conglomerate interpreted as a pseudo-condensed interval spanning the entire Productive Series-time in this region (Figure 3; Forte et al., 2015a). Unlike the samples above and below V-914, which contain significant proportions of all three types of lithic clasts, sample V-914 is dominated by mono-mineralic components and is virtually devoid of lithic grains.

The Sarica section contains the highest proportions of calcium-rich plagioclase, volcanic lithics, and pyroxene/amphibole of any of the measured sections. In the two lowest samples, S-90 and S-210, these three components account for greater than 50% of the composition of the rock. The cumulative abundance of these three components decreases to 30-40% in the middle of the section (samples S-360, S-610, S-865, and S-1100) and ~15% by the top of the section (sample S-1735). The decrease in the cumulative abundance of these three components is compensated by a corresponding increase in the proportions of carbonate and sedimentary lithic grains.

Most of the variability within the Xocashen section exists between the two individual measured intervals, i.e., Xocashen-1 and -2, that together make up the composite Xocashen measured section (Figure 4). Sample X-140, from the lower measured section (Xocashen-1), contains a significant component of calcium-rich plagioclase, whereas this component is mostly absent from samples in the Xocashen-2 section. The three samples from the Xocashen-2 section are dominated by sedimentary lithics, igneous and metamorphic lithics, and quartz, although the relative proportions of these components vary between the samples (Figure 4).

Within the Bozdagh section, the three lower samples (B-180, B-280, and B-530) contain relatively large proportions of calcium-rich plagioclase and alkali feldspars. In contrast, the uppermost sample (B-875) contains much less calcium-rich plagioclase and is instead dominated by sedimentary lithics and quartz. All four Bozdagh samples contain small amounts of clinopyroxene, despite the variation in calcium-rich plagioclase.

All of the Goy samples are dominated by either quartz or sedimentary lithics (Figure 4). Only the lowest sample, G-175, contains any significant amount of calcium-rich plagioclase, volcanic lithics, or clinopyroxene/amphibole. Sample G-175 also contains relatively abundant pyrite framboids within the carbonate matrix of the sandstone. Up-section, sample G-680 contains rounded clasts of carbonate with small inclusions that are morphologically similar to framboids, but compositionally are iron oxide, which Forte et al., (2013) previously interpreted to represent some amount of local sediment reworking. The main change up-section is an increase in the relative percentage of carbonate clasts from ~10% in G-175 to nearly 25% in G-1620.

We also analyzed six samples of Mesozoic volcaniclastic rocks from the Vandam zone (Figure 4, Table 4). Of these, only two (AB0862 and AB0857) had a sufficiently clastic texture to lend themselves to point counts. The other four samples (AB0863, AB0864, AB0867, and AB0895) had interlocking igneous textures. For the latter samples, instead of performing point counts, we estimated the modal mineralogy in terms of components identified in the sandstones. The two clastic samples are overwhelmingly dominated by volcanic lithics and albite, but also contain minor amounts of calcium-rich plagioclase, clinopyroxene and potassium feldspar (Figure 4). The mineralogy of the four igneous samples is variable, but all generally contain small amounts of quartz (0-15%) and are dominated by feldspar, the composition of which differs between samples (Figure 4). All four igneous samples contain clinopyroxene (5-25%) and all but AB0863 contain some percentage of calcium-rich plagioclase, with a maximum of ~50% in sample AB0895.

6.4 Major and Trace Element Composition

We obtained major and trace element geochemical analyses for a total of 27 sandstone samples from the Kura Fold-Thrust Belt, 13 samples of modern river sediment, and 11 samples of Mesozoic Vandam volcaniclastic rocks, complete results for which are in Table S3. In the following, we present a descriptive statistical treatment of the geochemical data in the form of bi-plots. Additionally, we discuss results of the hierarchical clustering analysis and principal component analysis to define populations within potential sources and linear discriminant analysis to classify the Kura Basin sandstones in terms of these identified source populations.

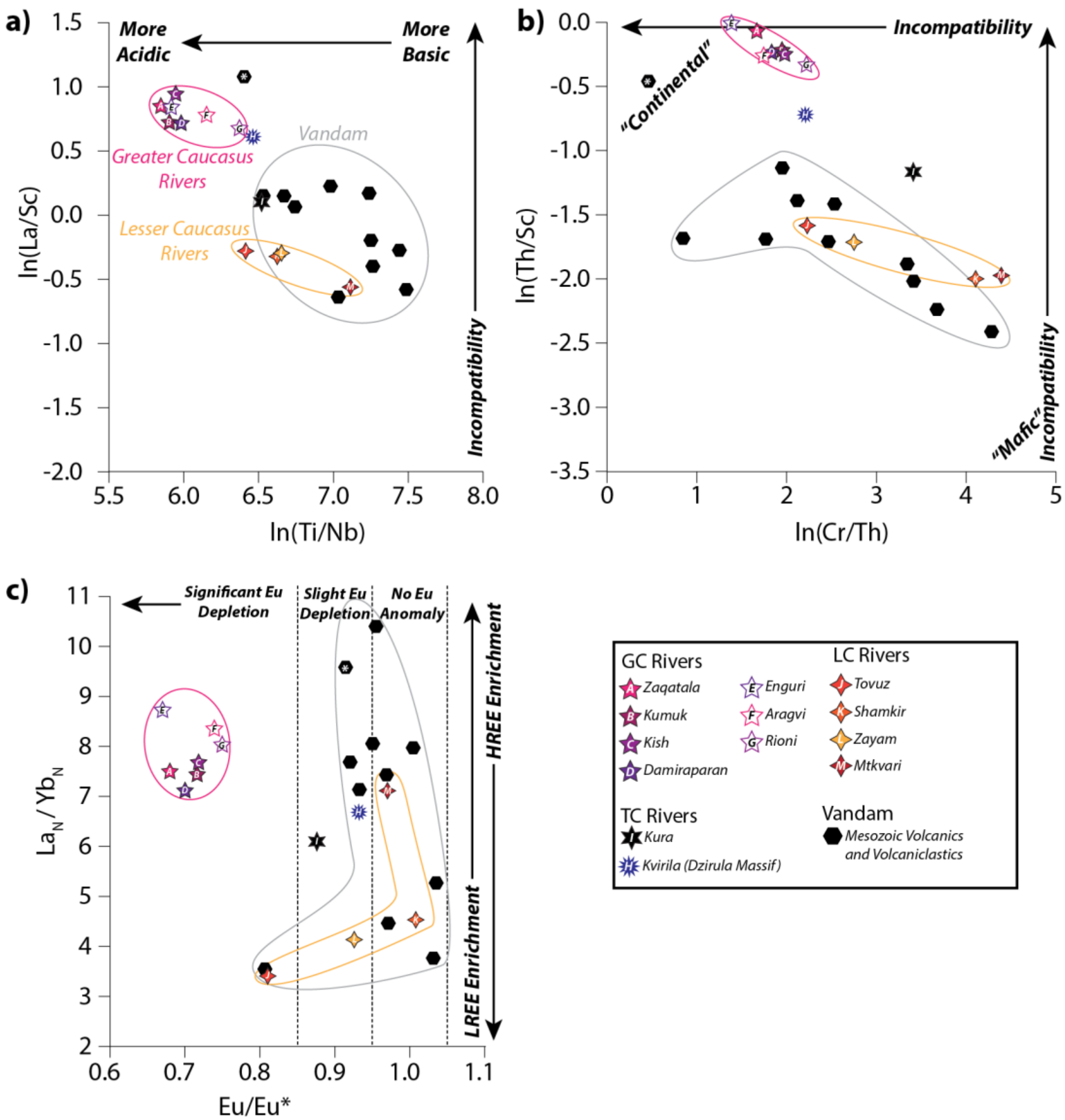

Figure 5 –Characterization of potential sediment sources via bulk geochemical analyses of modern river sediment and selected Mesozoic volcanic and volcaniclastic rocks from the southeastern Greater Caucasus. GC = Greater Caucasus, LC = Lesser Caucasus, TC = Transcaucasus, i.e., between the Lesser and Greater Caucasus. Colored lines on the plots enclose the compositional space that characterizes the Greater Caucasus (pink), Lesser Caucasus (orange) and Vandam (gray) sources. a) Natural log ratios of trace element ratios suggested to discriminate on the basis of incompatibility (La/Sc - Bhatia and Crook, 1986) and acidic (felsic) vs basic (mafic) sources (Ti/Nb - Bonjour and Dabard, 1991). b) Natural log ratios of Cr/Th and Th/Sc, which together should separate more "Continental" from more "Mafic" sources (Totten et al., 2000). c) Comparison of Eu/Eu vs La_N/Yb_N as suggested by Bhatia (1985).*

6.4.1. Bi-Plots

For the samples from known source areas (Figure 5), the bi-plots shows that rivers draining the Greater Caucasus (GC, N=7) are generally geochemically distinct from both the 4 rivers draining the Lesser Caucasus (LC, N=4) and the Vandam zone exposures (N=11) (Figure 5). In contrast, the Lesser Caucasus rivers and the Vandam volcaniclastic rocks overlap in all three of the compositional spaces defined by the selected elemental ratios (La/Sc vs. Ti/Nb, Th/Sc vs. Cr/Th, and La_N/Yb_N vs. Eu/Eu*). The Greater Caucasus rivers represent a relatively acidic (felsic), incompatible source enriched in light REE and depleted in Eu, whereas both the Lesser

Caucasus rivers and Vandam volcaniclastic rocks are more mafic, contain higher proportions of compatible elements, and have a less pronounced Eu anomaly. The Kvirila River, which drains the Dzirula massif, and the Kura River sample from the center of the basin vary in their associations between plots, sometimes plotting between the zones defined by the GC and the combined LC and GC Volcanic bedrock (Figure 5a). Vandam volcanic sample AB0863 is consistently an outlier, being more enriched in incompatible elements relative to the other Vandam volcaniclastic rocks, consistent with its different modal mineralogy (Table S2). The relatively close grouping of samples from the modern rivers and Vandam volcaniclastic rocks allows us to define three broad compositional fields within each bi-plot outlining Greater Caucasus, Lesser Caucasus, and Vandam-like sources (Figure 5).

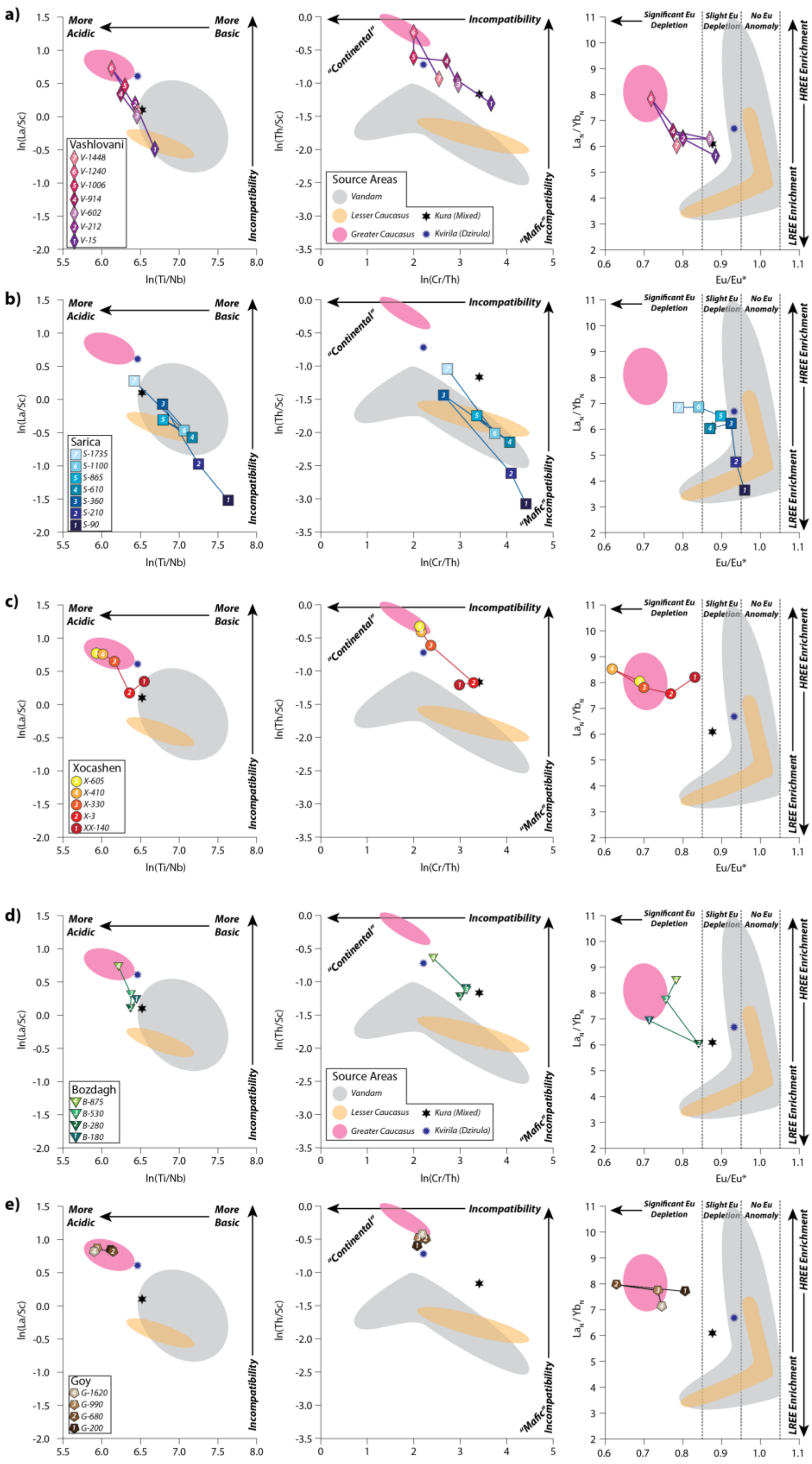

a)
b)
c)
d)
e)
More Acidic
More Basic
Incompatibility
ln(La/Sc)
ln(Ti/Nb)
ln(Th/Sc)
ln(Cr/Th)
"Continental"
"Mafic"
La_N / Yb_N
Eu/Eu*
Significant Eu Depletion
Slight Eu Depletion
No Eu Anomaly
HREE Enrichment
LREE Enrichment
Vashlovani
V-1448
V-1240
V-1006
V-914
V-602
V-212
V-15
Sarica
S-1735
S-1100
S-865
S-610
S-360
S-210
S-90
Xocashen
X-605
X-410
X-330
X-3
XX-140
Bozdagh
B-875
B-530
B-280
B-180
Goy
G-1620
G-990
G-680
G-200
Source Areas
Vandam
Lesser Caucasus
Greater Caucasus
Kura (Mixed)
Kvirila (Dzirula)

Figure 6 – Characterization of sandstone samples from the Kura Fold-Thrust Belt using the same three bi-plots of geochemical ratios and source-area fields as in Figure 5, with stars showing the two Kura Basin river samples. Colored blobs on this figure show the same source-area fields outlined on Figure 5: Greater Caucasus (pink), Lesser Caucasus (orange) and Vandam (gray). Symbols on the plots use the same shape, color, and numbering scheme as on Figures 3 and 4. Each row shows the three bi-plots for the stratigraphic sections at a) Vashlovani, b) Sarica, c) Xocashen, d) Bozdagh, ,and e) Goy.

For the sandstone samples of unknown provenance in the Kura Fold-Thrust Belt (Figure 6), the patterns on the bi-plots vary between the individual measured sections but in all cases show a general up-section trend in which samples from the lower (older) portions of the measured section generally plot closer to the Lesser Caucasus-Vandam field, whereas those from higher (younger) intervals plot closer to the Greater Caucasus field (Figure 6). The Sarica section shows the strongest affinity with the LC-Vandam source, with the two lowest samples being even more incompatible and mafic than either the LC or Vandam sources (Figure 6b). Both Xocashen (Figure 6c) and Goy (Figure 6e) plot relatively close to the GC field, but with the base of Xocashen overlapping with the Vandam field. The Bozdagh samples plot mostly between the GC and LC-Vandam fields, similar to the mid-basin Kura River and Kvirila River (Figure 6d). The Vashlovani section shows a steady progression from LC-Vandam to GC between samples V-15 and V-1240, but the youngest sample, V-1448, shows an abrupt shift back towards the LC-Vandam region of the plots (Figure 6a).

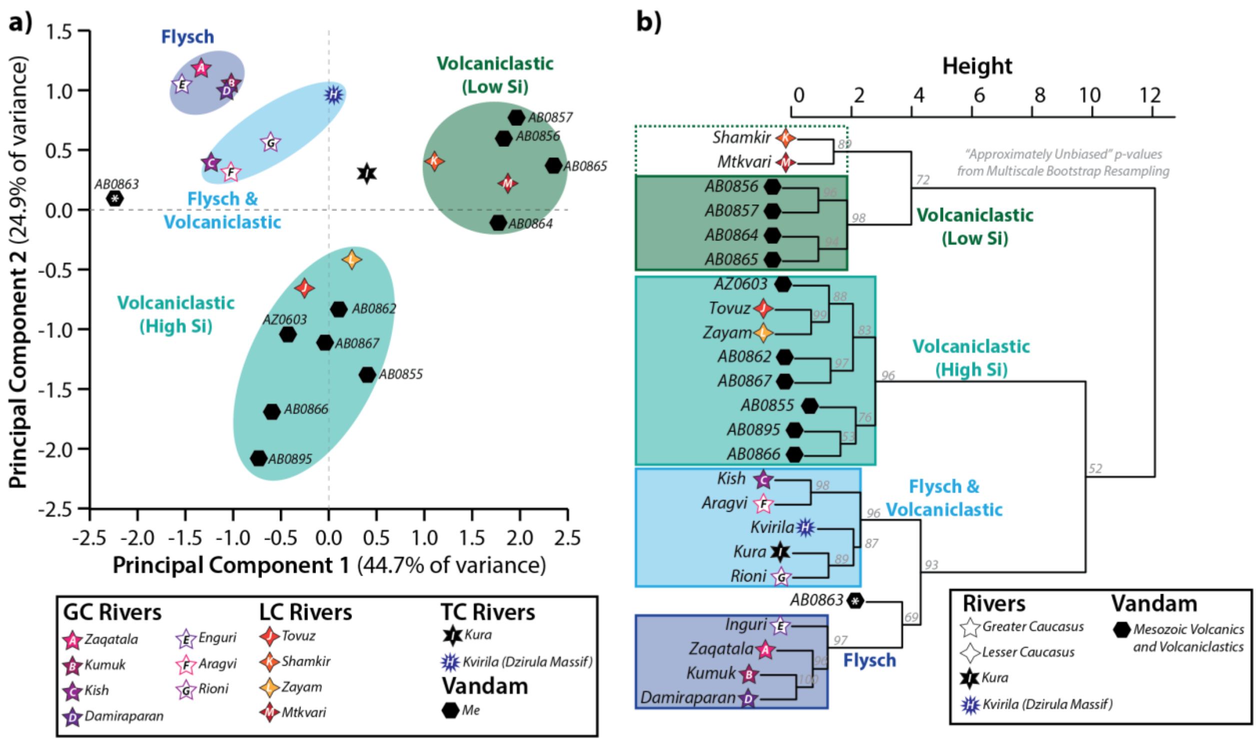

Figure 7 – Source area characterization from multivariable statistics of trace elements. a) Result of principal component analysis (PCA) highlighting separation of potential source terrains into four semi-distinct zones with one outlier (AB0863); the Kura River sample plots in the middle of these fields, consistent with the expectation that it is a mixture of all 4 potential sources.GC = Greater Caucasus, LC = Lesser Caucasus, TC = Transcaucasus. b) Result of hierarchical clustering analysis highlighting a similar separation as suggested by the PCA in 7a.

6.4.2 Multivariate Characterization of Potential Source Areas

Analyses of the ILR-transformed trace-element suite in terms of both principal components (Figure 7a) and hierarchical clustering (Figure 7b) largely confirm the first order observations from the bi-plots and similarly identify sample AB0863 as an outlier. Here again, the Greater Caucasus Rivers are distinct from both the Lesser Caucasus Rivers and Vandam, with the latter two not readily distinguishable from one another (Figure 7). In detail, the multivariate analyses reveal more subtle divisions within these broader groups, dividing each into two recognizable sub-populations. For the two sub-populations of GC rivers, we informally refer to these as a “flysch” member and a “flysch and volcanoclastic” member and collectively as a “GC” sources. This largely reflects that in both the PCA and hierarchical clustering analysis, the latter plots closer to the volcanic and volcanoclastic fields and thus may represent some amount of mixing between a more dominantly flysch derived end-member source and these volcanic or volcaniclastic sources. For the two sub-populations of the LC-Vandam, we refer to these as the “High Si” and “Low Si” groups, where the majority of samples in the former group have weight percent $SiO_2 > 55\%$ and the latter have weight percent $SiO_2 < 55\%$.

In the principal component analysis, the first two principal components are able to account for ~70% of the variance and yield an identical separation as the cluster analysis between samples within the LC-Vandam group, indicating two clear populations (Figure 7a). The division within the GC rivers indicated by the cluster analysis is present in the principal component analysis but is less distinct and the mid-basin Kura River plots between the GC and the two populations of LC-Vandam group (Figure 7a).

It is important to note that while at the gross scale, the geochemically defined sources define geographically distinct sources, i.e., GC vs LC and Vandam vs Transcaucasus (i.e., between the GC and LC), at finer scales they lack clear spatial relationships. For the GC affiliated rivers, there is no clear along-strike pattern in terms of the two sub-populations. This extends to the Vandam source, and in this case, bedrock samples that are differentiated into the two distinct groups come from outcrops only a few km from each other.

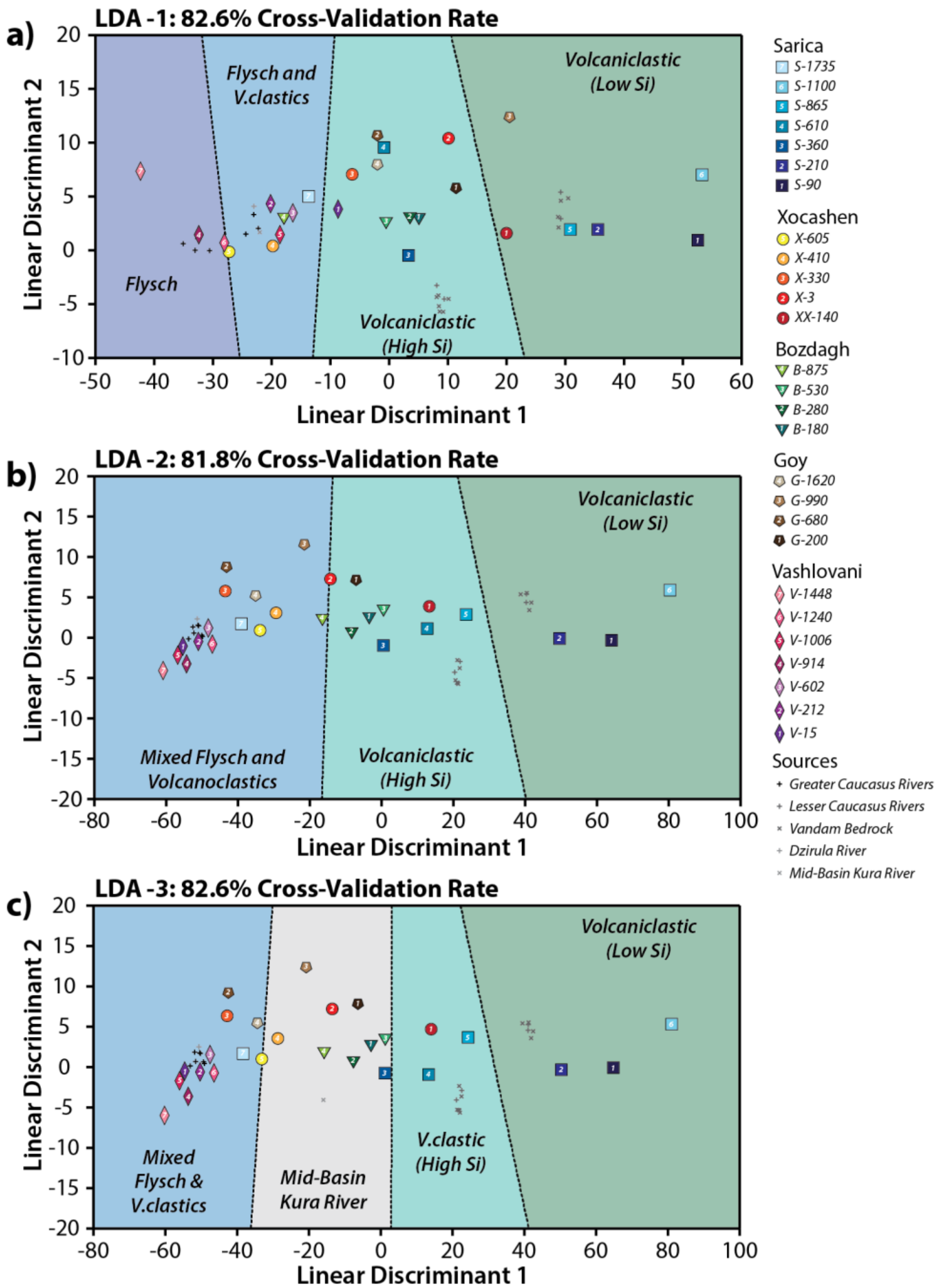

Figure 8 – Results of linear discriminant analysis considering three different source divisions. Cross-validation rate, shown at the top of each LDA, are similar between all analyses.

6.4.3. Linear Discriminant Analysis

We use the four populations identified in the hierarchical clustering and principal component analyses to define initial groups for linear discriminant analyses (LDA) (Tables 8, 9). While largely similar, the results of the principal component analysis and cluster analysis do not completely overlap in terms of divisions between populations. Thus, we run 6 different LDAs to test multiple different initial groups. Here we present results from the 3 highest-performing LDAs, which have correct rates of classification from cross-validation of >80% (Figure 8 and

Table 8), similar to the methodology of Von Eynatten et al.,(2003). We present all 3 because there is no robust statistical or geological reason to favor one over the others. The three lower-performing LDAs have correct classification rates from cross-validation of 40-70%, including one that uses geographically defined groups in which all Vandam volcaniclastic rocks are considered one group and all Lesser Caucasus river sediments are considered another.

The three high-performing LDAs use different groupings for the Greater Caucasus fields and constant groupings for the two sets of Vandam volcaniclastic rocks and LC rivers as identified in the principal component and clustering analyses. In LDA-1, the Greater Caucasus Rivers are divided as indicated by the cluster analysis, with the mid-basin Kura included in the training data as part of the Flysch & Volcaniclastic group (Figure 8 and Table 8). In LDA-2, all of the Greater Caucasus Rivers are combined in a single group, in accordance with the principal component analysis, and the mid-basin Kura River is excluded from the training dataset. LDA-3 is identical to LDA-2 except the mid-basin Kura River is included as a separate group. The outlier Vandam sample AB0863 is excluded from all three LDAs (Figure 8).

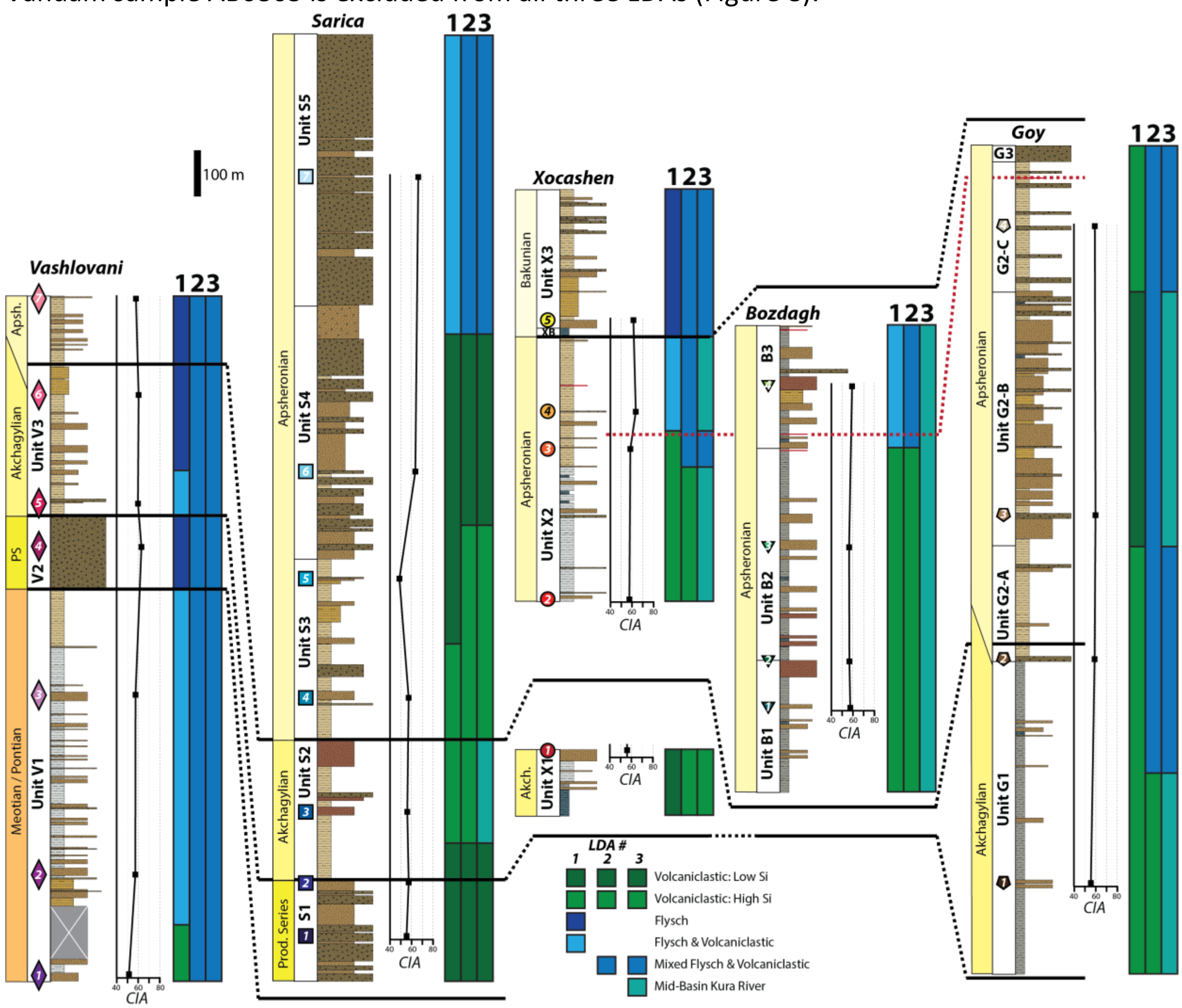

Figure 9 – Results of three different LDAs considered as a function of stratigraphic position. Also shown are the chemical index of alteration (CIA - Nesbitt and Young, 1982). Comparisons of CIA to other weathering indices are shown in Figure S8. Note that generally we do not have constraint on where within the sections between samples provenance would change, so the location of the changes shown here are schematic.

The results of using LDA-1 or LDA-2 to classify the Kura Basin sediments are largely similar (Figure 8, 9, and Table 9). Nearly all of the Vashlovani section is classified as being derived exclusively from the Greater Caucasus, with the LDA-1 classification suggesting that the section was sourced variably from mostly either the flysch or flysch & volcaniclastic source, consistent with the results of LDA-2 (Figure 9). Within the Sarica section, both LDA-1 and 2 imply predominantly a LC-Vandam source, except for the youngest sample S-1735. The two classifications also largely agree in terms of which LC-Vandam source but differ in the classification of sample S-865. The classification of the Xocashen section suggests a LC-Vandam source for the lower two samples and a GC source for the upper three samples. Similarly, Bozdagh records LC-Vandam sources for the lower three samples and a GC source for the upper sample. The largest disagreement between LDA-1 and -2 comes in the classification of the Goy section. LDA-1 classifies the entire section as being derived from the LC-Vandam source and LDA-2 classifies only the lowest most sample as LC-Vandam source, with the upper three sections classified as a GC source.

Classifying using LDA-3, which includes the mid-basin Kura River as a separate source, produces similar results as LDA-1 and LDA-2 for some of the section but dramatically different results for others (Figure 8, 9, Table 9). Vashlovani is again classified as solely sourced from the Greater Caucasus and Sarica remains mostly unchanged with the only difference being the classification of sample S-360 as similar to the mid-basin Kura River. However, all of the Bozdagh samples are reclassified as being similar to the mid-basin Kura River. Both Xocashen and Goy are partially reclassified, resulting in alterations between GC and Kura sources, although the lowest sample in Xocashen remains as sourced from LC-Vandam.

6.4.4 Weathering Indices

The values of the CIA, CIW, and PIA all follow similar trends within a given section and thus we focus just on the CIA. Relationships between the CIA, CIW, and PIA are available in the supplement (Figure S8). Across all sections, values of the CIA occupy a narrow range between 48-66, indicating relatively low to modest amounts of weathering (e.g., McLennan, 1993). CIA generally increases up section within all of the columns except Bozdagh where it remains largely constant throughout (Figure 9). In general, CIA appears to increase in sync with the transitions from more volcanic/volcaniclastic-related sources to more flysch-related sources as indicated by the geochemical classifications (Figure 9).

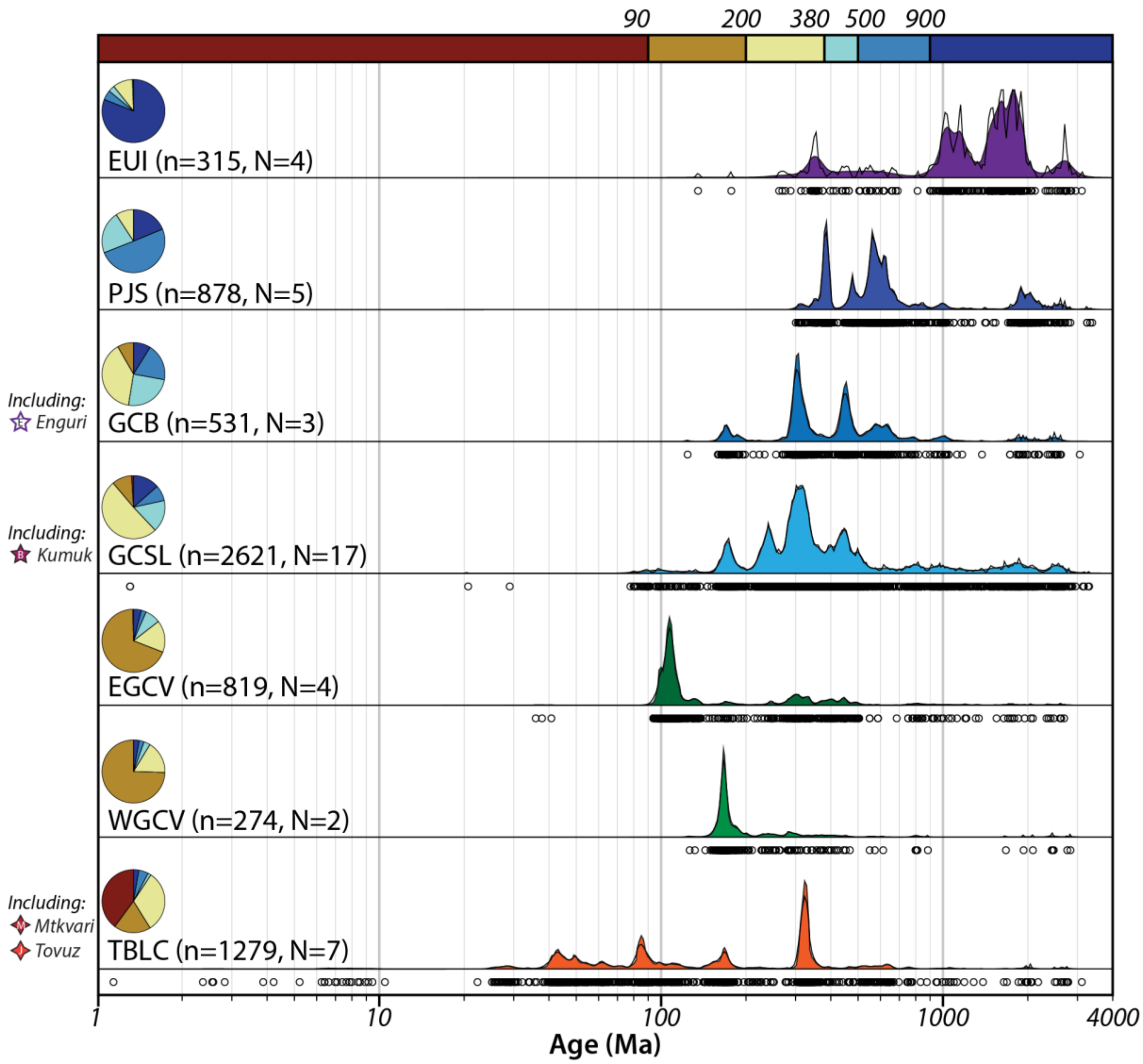

Figure 10 – Composite detrital zircon populations used to define source terranes, following the definitions by Tye et al., (2020). See text for additional discussion of source terranes. Plot was generated using DensityPlotter (Vermeesch, 2012) with KDEs colored and PDEs hollow. Colors of KDEs are for reference in subsequent figures. Colored bar across the top shows diagnostic age ranges suggested by Tye et al., (2020). Pie charts show the proportions of these diagnostic ages within each composite sample. Both the total number of zircons that define each source (n) and total samples contributing to the source (N) are shown. Composite samples are detailed in Table 4 and reported by Allen et al., (2006), Wang et al., (2011), Cowgill et al., (2016), Vasey et al., (2020), Tye et al., (2020), Trexler et al., (2022), and Forte et al., (2022a).

6.5 Detrital Zircon U-Pb Ages

6.5.1 Age Distributions

We present PDPs and KDEs for both the composite DZ sources (Figure 10) and 7 Kura Fold-Thrust Belt DZ samples (Figure 11) to enable visual comparison prior to statistical comparison below. It is important to note that the definition of source terranes is different between the U-Pb detrital zircons and the geochemical classifications, a point we return to in the discussion. The vast majority of ages within the thrust belt samples are Mezosoic and Paleozoic, although there are some Cenozic grains in the two Bozdagh samples (B-280 and B-875) and the lower Sarica and upper Vashlovani samples (S-210 and V-1240, respectively. The only samples with sizeable portions of Proterozoic and older grains are the lower Vasholvani sample (V-15) and both those from Bozdagh (Figure 11). Within the context of the distinctive age populations defined by Tye et al., (2020), the vast majority of samples are dominated by mixtures of <90 Ma Lesser Caucasus arc associated materials, 90-200 Ma age grains associated with either the Lesser Caucasus arc of Greater Caucasus rifting, or 200-380 Ma grains associated with the Variscan orogeny. For all samples except V-15, older age populations make up less than 25% of the total grains. Both S-210 and V-1240 are notable for containing statistically significant numbers of extremely young grains with mean ages of 2.5 ± 0.24 Ma (n=3) and 2.66 ± 0.046 Ma (n=47), respectively, which Forte et al., (2015a) used to determine maximum depositional ages.

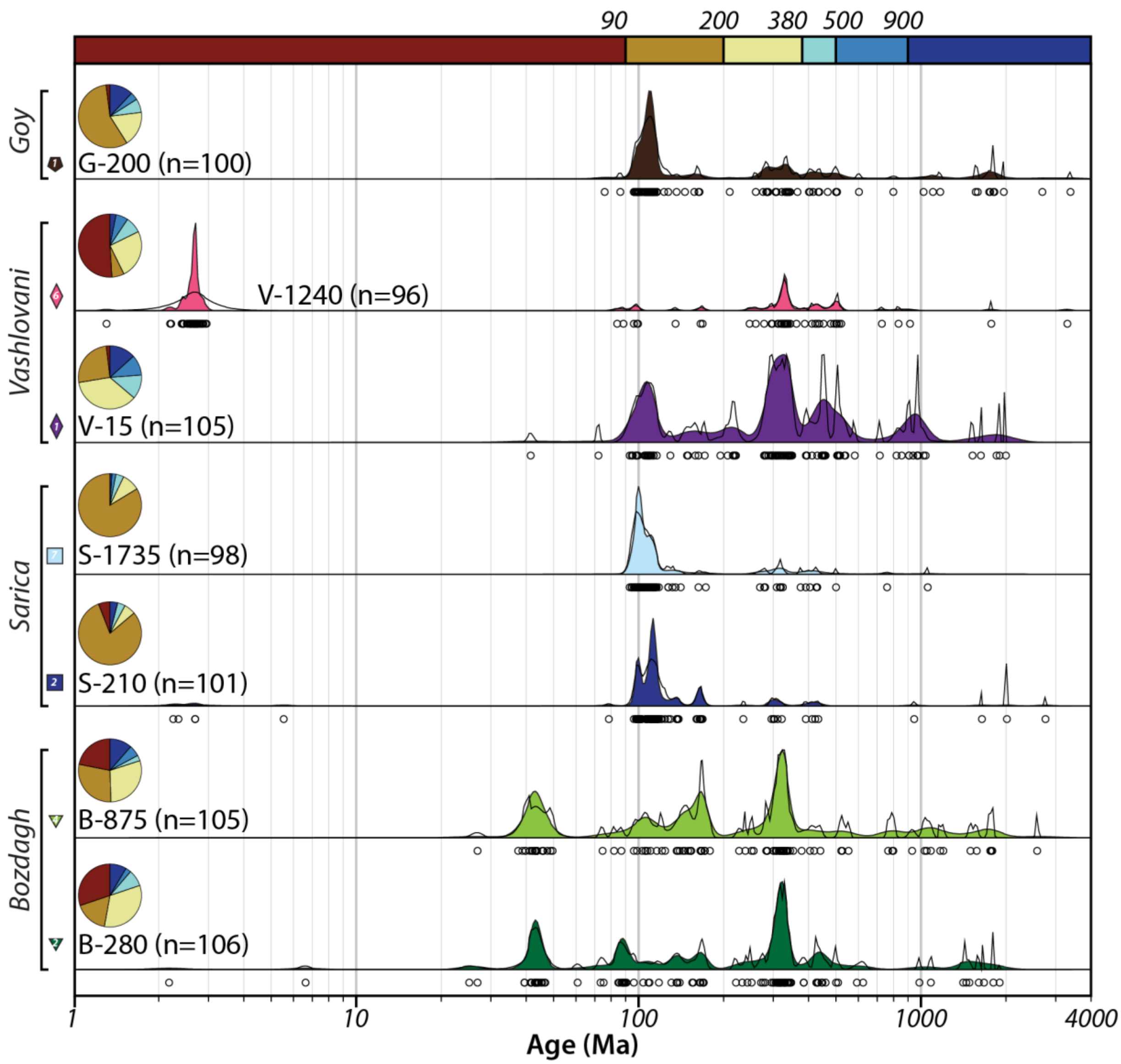

Figure 11 – Detrital zircon populations for the 7 new Kura Fold-Thrust Belt samples. Setup of figure is identical to Figure 10.

6.5.2 Statistical Comparisons with Sources

As described in Section 5.4, we compare the U-Pb ages from our new basin samples with those from potential source terrains using three different methods: multidimensional scaling (MDS) plots (Vermeesch, 2013), monte-carlo unmixing models (Sundell and Saylor, 2017), and Bayesian population correlation (BPC) (Tye et al., 2019). We first consider the results of each of these three methods individually (Figure 12) before synthesizing their results. We removed the populations of very young grains from samples S-210 and V-1240 prior to conducting the statistical comparisons because these grains most likely reflect contemporaneous, or nearly contemporaneous, regional volcanism at the time of deposition. Thus we assume they do not represent the provenance. Because none of the composite sources have age populations of this age, including these grains would effectively mask the provenance signature in the statistical methods we employ. That problem is particularly acute for V-1240 because the young grains constitute nearly 50% of the total population in this sample. We present the results of both the monte-carlo mixing models (Figure 12a, Table 10) and the BPC comparison (Figure 12b) from west to east.

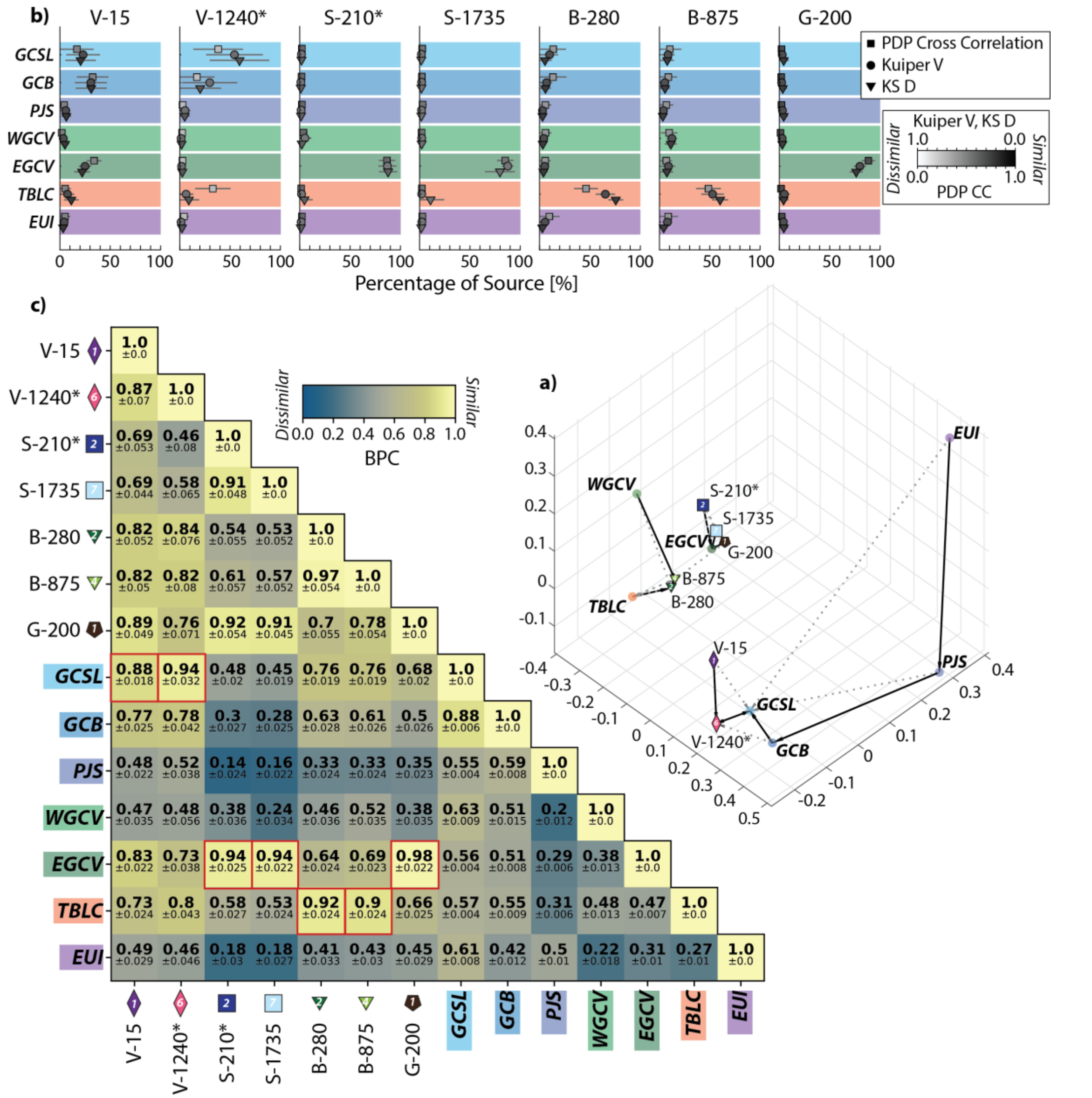

*Figure 12 – Results from three different statistical comparisons of detrital zircon ages from the fold-thrust belt samples with those from the composite sources. Samples V-1240 and S-210 were modified (indicated by *) by removing the young populations of grains that define the MDAs to reduce bias (see text for explanation). a) Multidimensional scaling plot from DZmds (Saylor et al., 2018). Solid lines indicate closest neighbor, dashed lines indicate next closest neighbor. b) Results of unmixing model using DZmix (Sundell and Saylor, 2017) showing estimated percentage contribution of each composite source based on three different statistical metrics. c) Results of Bayesian population correlation (Tye et al., 2019) between KFTB samples and composite sources. Red boxes indicate composite source and KFTB sample with the highest similarity based on BPC.*

The MDS plot (Figure 12a) indicates (1) close correspondence between fold-thrust belt samples S-210, S-1735, and G-200 with the EGCV source, (2) relatively close correspondence between basin samples B-280 and B-875 and the TBLC source and to a lesser extent the WGCV source, (3) moderate correspondence between basin samples V-15 and V-1240 with the GCSL and/or GCB sources, and (4) none of the fold-thrust belt samples have particularly strong correspondence with either the PJS or EUI sources. Finally, the MDS plot also shows that the individual amalgamated sources are largely distinct from each other (Figure 12), which is a point noted by Tye et al., (2020) based on their BPC analysis.

In the monte-carlo mixing models (Figure 12b, Table 10), both Vashlovani samples (V-15 and V-1240) show moderate percentages (20-50%) of sourcing from the GCSL and GCB. Sample V-15 also has a moderate percentage (20-30%) from the EGCV source that is not seen in V-1240 whereas V-1240 has some possible sourcing from TBLC that is not seen in V-15, although in this latter case the scatter of the dots on the plot indicates disagreement between the 3 different statistical tests. In addition, there is a higher fraction of GCSL in V-1240 than V-15, indicating an up-section increase in the influence of this source. In Sarica, both S-210 and S-1735 are almost exclusively sourced from the EGCV source. In Bozdagh, both B-280 and B-875 are most strongly influenced by the TBLC source, with low levels (< 15%) of influence from a number of the other sources, including WGCV, GCSL, and even EUI. The one sample from Goy, G-200 is nearly exclusively sourced from EGCV, making it largely similar to the two Sarica samples.

In the BPC comparison (Figure 12c), the two Vashlovani samples have the highest degree of similarity with the GCSL source along with elevated similarity with the GCB, EGCV, and TBLC sources. In detail, the second highest similarity in V-15 is to EGCV whereas in V-1240 it is to TBLC. Both Sarica samples show only a strong similarity with EGCV (>0.9) with the next highest similarity being TBLC, but at lower values (<0.6). Both Bozdagh samples are very similar to the TBLC source (>0.9), but also show some similarity with the GCSL source (>0.7). Finally, the G-200 sample from Goy is very similar to the EGCV source (0.98), with the next similar sources being GCSL and TBLC (both <0.7).

Taken together, the results of all three methods are broadly consistent with each other. All methods indicate a close correspondence between samples from the same section, with samples from the top and bottom of the same section being more generally similar to one another than to samples from different sections, even if those samples are more closely time-equivalent. In addition, the three methods indicate broadly consistent sources for the individual samples, although there are some exceptions. Vashlovani and Bozdagh show both the most complicated sourcing and the largest amount of disagreement between the methods. For Vashlovani, all methods indicate significant contributions from GCSL and GCB, but vary in the extent to which they include EGCV or TBLC. All three methods indicate TBLC as the primary source for Bozdagh, but with some minor inputs from other sources, including GCSL, EGCV, and WGCV, but the proportions or importance of these vary between methods. In contrast, in both Sarica and the lower Goy sample, all methods consistently indicate nearly exclusive sourcing from the EGCV source.

Quaternary	V-15	V-1240	S-210	S-1735	B-280	B-875	G-200
[1]WF-4	0.71 ±0.033	0.52 ±0.039	0.28 ±0.038	0.32 ±0.033	0.65 ±0.038	0.59 ±0.037	0.51 ±0.037
[1]WF-5	0.77 ±0.032	0.51 ±0.036	0.28 ±0.034	0.28 ±0.029	0.66 ±0.035	0.65 ±0.034	0.5 ±0.031
Akchagyl							
[1]WF-3	0.62 ±0.042	0.63 ±0.045	0.44 ±0.042	0.3 ±0.041	0.65 ±0.045	0.67 ±0.043	0.51 ±0.042
Surakhany							
[3]Yas-1	0.63 ±0.048	0.4 ±0.054	0.31 ±0.052	0.29 ±0.047	0.6 ±0.057	0.62 ±0.053	0.59 ±0.051
[3]Yas-1	0.71 ±0.048	0.43 ±0.054	0.36 ±0.048	0.3 ±0.048	0.65 ±0.052	0.64 ±0.05	0.59 ±0.047
Sabunchy							
[3]II-99	0.72 ±0.051	0.47 ±0.056	0.42 ±0.054	0.37 ±0.05	0.66 ±0.055	0.67 ±0.052	0.64 ±0.053
[3]II-146	0.76 ±0.049	0.52 ±0.059	0.39 ±0.053	0.4 ±0.051	0.71 ±0.056	0.68 ±0.054	0.68 ±0.052
Balakhany IX							
[2]BA7	0.53 ±0.061	0.33 ±0.072	0.29 ±0.065	0.26 ±0.061	0.52 ±0.068	0.56 ±0.072	0.58 ±0.061
[2]BA9	0.6 ±0.059	0.35 ±0.069	0.31 ±0.064	0.27 ±0.059	0.56 ±0.069	0.55 ±0.068	0.59 ±0.061
[3]II-27	0.78 ±0.046	0.55 ±0.056	0.39 ±0.05	0.38 ±0.047	0.68 ±0.052	0.7 ±0.051	0.64 ±0.048
Balakhany X							
[3]II-15	0.8 ±0.044	0.6 ±0.054	0.43 ±0.049	0.41 ±0.044	0.71 ±0.05	0.7 ±0.051	0.67 ±0.048
Fasila							
[3]AZ-K9	0.59 ±0.048	0.38 ±0.052	0.34 ±0.047	0.27 ±0.05	0.59 ±0.052	0.59 ±0.049	0.57 ±0.048
[3]NKG198	0.78 ±0.053	0.5 ±0.057	0.35 ±0.052	0.36 ±0.05	0.67 ±0.055	0.72 ±0.056	0.68 ±0.053
NKP							
[3]NKP181	0.77 ±0.045	0.53 ±0.054	0.45 ±0.047	0.43 ±0.047	0.73 ±0.052	0.75 ±0.051	0.7 ±0.05

Productive Series (Surakhany – NKP)

Kirmaky Suite	V-15	V-1240	S-210	S-1735	B-280	B-875	G-200
[3]KS70	0.76 ±0.05	0.48 ±0.057	0.43 ±0.053	0.36 ±0.049	0.7 ±0.053	0.68 ±0.053	0.64 ±0.051
[3]KS98	0.73 ±0.048	0.55 ±0.052	0.37 ±0.05	0.35 ±0.046	0.66 ±0.052	0.68 ±0.052	0.61 ±0.047
[2]LKS5	0.68 ±0.061	0.49 ±0.067	0.39 ±0.064	0.34 ±0.058	0.65 ±0.068	0.68 ±0.064	0.63 ±0.063
[2]LKS3	0.62 ±0.067	0.44 ±0.071	0.3 ±0.066	0.29 ±0.065	0.59 ±0.07	0.62 ±0.07	0.62 ±0.065
[3]AZ-K3	0.58 ±0.048	0.36 ±0.052	0.27 ±0.05	0.25 ±0.047	0.52 ±0.052	0.55 ±0.052	0.53 ±0.048
PK							
[3]PK23	0.66 ±0.047	0.48 ±0.053	0.34 ±0.049	0.32 ±0.047	0.62 ±0.052	0.67 ±0.048	0.62 ±0.047
Productive Series							
[1]EF-6	0.85 ±0.035	0.52 ±0.039	0.65 ±0.039	0.62 ±0.035	0.97 ±0.036	0.96 ±0.038	0.83 ±0.036
Meotian-Pontian							
[1]CF-2	0.9 ±0.031	0.59 ±0.034	0.5 ±0.032	0.52 ±0.029	0.76 ±0.034	0.81 ±0.033	0.72 ±0.032
Pontian							
[1]EF-5	0.84 ±0.037	0.54 ±0.042	0.4 ±0.041	0.37 ±0.037	0.81 ±0.04	0.81 ±0.039	0.64 ±0.039
Oligo-Miocene							
[1]WF-1	0.78 ±0.064	0.58 ±0.07	0.44 ±0.064	0.42 ±0.057	0.76 ±0.066	0.79 ±0.068	0.68 ±0.064
[1]WF-2	0.8 ±0.033	0.55 ±0.036	0.37 ±0.034	0.37 ±0.033	0.72 ±0.036	0.73 ±0.035	0.65 ±0.034
[1]EF-3	0.79 ±0.034	0.48 ±0.038	0.31 ±0.038	0.34 ±0.034	0.74 ±0.037	0.74 ±0.036	0.58 ±0.037
[1]EF-4	0.8 ±0.032	0.54 ±0.035	0.3 ±0.035	0.34 ±0.032	0.75 ±0.034	0.75 ±0.034	0.6 ±0.033
Mid Miocene							
[1]CF-1	0.49 ±0.033	0.4 ±0.038	0.33 ±0.034	0.28 ±0.032	0.82 ±0.035	0.81 ±0.036	0.41 ±0.036
Late K - Paleogene							
[1]EF-1	0.77 ±0.033	0.56 ±0.035	0.31 ±0.034	0.36 ±0.032	0.7 ±0.037	0.67 ±0.035	0.6 ±0.034
[1]EF-2	0.8 ±0.034	0.53 ±0.037	0.35 ±0.035	0.34 ±0.031	0.7 ±0.034	0.71 ±0.032	0.61 ±0.035

Productive Series (Kirmaky Suite – Productive Series)

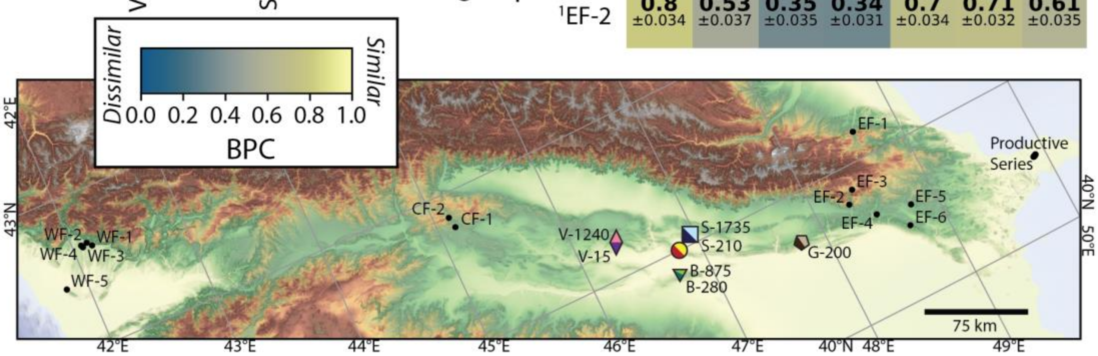

Figure 13 - BPC comparisons of detrital zircon populations of Kura Fold-Thrust Belt sandstone samples with samples from [1]Tye et al., (2020), [2]Allen et al., (2006), and [3]Abullayev et al., (2018). Location of samples shown in map at bottom of figure. All Productive Series samples except EF-6 come from the location labeled "Productive Series" on the map.

6.5.3 Statistical Comparisons with Other Foreland Basin Samples

To better place the Kura Fold-Thrust Belt U-Pb DZ samples into context with prior DZ work within the Greater Caucasus foreland, we use BPC to compare available samples (Figure 13). The prior samples come from four broad geographic regions, (1) the Rioni Foreland (samples WF-1 through WF-5; Tye et al., 2020), (2) the Gombori Range between the Kura and Kartli Basins (samples CF-1 and CF-2; Tye et al., 2020), (3) the eastern tip of the Kura Fold-Thrust Belt and Greater Caucasus (samples EF-1 through EF-6; Tye et al., 2020), and (4) various samples of the Productive Series on the Apsheron Peninsula (Allen et al., 2006; Abdullayev et al., 2018). The BPC analysis indicates generally low similarity between our 7 Kura Fold-Thrust Belt samples and others in the foreland. Vashlovani is the most diverse, with the basal sample (V-15) showing similarity (0.9 to 0.8) with foreland samples CF-2, EF-6, EF-5, WF-2, and EF-4, whereas the upper sample (V-1240) shows low correspondence (<0.63) with all foreland samples. Both Sarica samples have low similarity (<0.65) with all foreland samples.The Bozdagh samples show strong similarity (>0.95) with sample EF-6, and some similarity (>0.8) with foreland samples EF-5, and CF-1. The single Goy sample is similar (0.83) to Productive Series sample EF-6.

Finally, it is worth noting that for the individual KFTB samples that do show similarity with other foreland samples, there are mixed indications in terms of clear relationships between samples on the basis of temporal or spatial proximity. For example, even though the majority of the KFTB samples are of Akchagyl age or younger, none show particularly strong correspondence with similarly aged or younger sediments (samples WF-3 through WF-5; Figure 13). In contrast, sample V-15 at the base of Vashlovani, shows its strongest correspondence with CF-2, a similarly aged (Meotian-Pontian) sample that is relatively close to Vashlovani.

7. DISCUSSION

7.1 Reconciling Results of Different Provenance Methods

7.1.1 Source Definitions

With few exceptions, the samples defining sources within the Greater and Lesser Caucasus based on bulk geochemistry and detrital zircon U-Pb geochronology are not spatially co-located, i.e., they do not come from the same exact location or represent the same exact sample. For those that are colocated, specifically the modern sediment samples from the Enguri, Kumuk, Mtkvari, and Tovuz rivers and bedrock sample AB0862 for which Cowgill et al., (2016) report the U-Pb DZ ages and we report the bulk geochemistry, the results suggest that the geochemical sources defined here and the DZ sources defined by Tye et al., (2020) cannot be mapped directly into each other. Within the GC, geochemically both the Enguri and Kumuk rivers are classified as part of the GC flysch source, but in the DZ classification, the Enguri river is grouped with Greater Caucasus basement (GCB) whereas the Kumuk river is grouped with the Greater Caucasus siliciclastic (GCSL). Further, the Enguri watershed contains bedrock and nested catchments that are classified as GCB, GCSL, and PJS DZ sources (Figure 1). Similar complications can be found when considering DZ sources within watershed boundaries of individual basins for which we classified the geochemistry, as was seen for the Enguri watershed. For example, the Aragvi, Kish, and Damiraparan Rivers within the GC all contain, or are directly adjacent to, samples classified as being part of the GCSL source, but span both GC affiliated geochemical sources, with the Aragvi and Kish Rivers being part of the flysch and volcaniclastic source whereas the Damiraparan River is part of the flysh source.

Similar patterns are observed in the Lesser Caucasus and/or volcanic and volcaniclastic associated sources. At the broadest level, as demonstrated by Tye et al., (2020) the volcanics and volcaniclastics along the southern GC rangefront which define the WGCV and EGCV DZ sources can be differentiated from the rivers draining the Lesser Caucasus and that define the TBLC DZ source. In contrast, geochemically, rivers draining, or bedrock from, either the volcanic and volcaniclastics in the eastern GC, i.e., the Vandam, and those from the LC are not able to be differentiated, consistent with prior suggestions of a genetic link between these two regions (e.g., Kopp and Shcherba, 1985). At the individual river level, both the Tovuz and Mtkvari River were classified as a part of the Transcaucasus Basement and Lesser Caucasus Arc (TBLC) source on the basis of their U-Pb ages, and while they geochemically are both categorized as a volcanic or volcaniclastic source, the Mtkvari is contained within the Low Si subpopulation whereas Tovuz is contained within the High Si subpopulation. Similarly, bedrock samples defined geochemically as either of the LC-Vandam sources are contained within watersheds of catchments from which modern sediment U-Pb age populations were used by Tye et al., (2020) to define the EGCV source. This includes bedrock sample AB0862, which geochemically is classified here as from the High Si source, but whose DZ population is part of the samples used to define the EGCV DZ source (Cowgill et al., 2016; Tye et al., 2020).

Point counts on some of the same bedrock samples from the Vandam region in the GC (Figure 4, Tables 4, S2) allow us to consider potential differences between the two LC-Vandam geochemical sub-populations in the context of mineralogy and texture, but ultimately do not reveal clear distinguishing characteristics. Both geochemical populations span samples that are texturally volcanic compared to volcanoclastic and the clast counts and/or modal mineralogy do not reveal systematic differences. The only clarifying detail from the point counts of the Vandam volcaniclastic samples relates to AB0863, which is an outlier in all geochemical classifications. Compared to the other bedrock samples, AB0863 is completely devoid of calcium rich plagioclase and has relatively low amounts of pyroxene or amphibole, instead being dominated by albite and potassium and/or alkali feldspar. This would broadly suggest that the calcium rich plagioclase, pyroxenes, and amphiboles that are largely absent from AB0863 are important in terms of defining both of the volcanic and volcaniclastic sources from a bulk geochemical perspective.

7.1.2 Basin Samples

An alternative way to compare the results and implications of the different provenance methods is through the Kura basin samples from the measured sections. For this purpose, we develop comparisons between the results of the linear discriminant analysis and the point counts (Figure 14), and then between the linear discriminant analysis and the Bayesian population correlation for the detrital zircon data (Figure 15). For the LDA results in both comparisons, we consider just the values of the first linear discriminant (i.e., the x-axis in Figure 8) for the different LDAs. Because the decision boundaries within the LDAs are nearly vertical, the first linear discriminant is relatively effective as a single numeric metric of source affinity. Further, for this comparison, we only consider the first and second LDA results because the values of the first discriminant are the same for the second and third LDAs. The difference between second and third LDAs instead relate to the location of the decision boundaries and interpretation of sources that result from which field the unknown samples plot within (Figure 8). To compare the LDA results to the point counts, we first perform a random forest regression using the percentage of the point count components to predict the value of linear discriminant 1 for both LDA-1 and LDA-2. Random forest regression is a useful method for assessing the importance of sets of multivariate data in contributing to a single variable, in this case, the value of the linear discriminant (e.g., Grömping, 2009). For each LDA, we use the results of the random forest regression to identify the most important components from the point counts and assess the extent to which they alone or in aggregate correlate to the LDA. Finally, to compare the LDA results to the detrital zircon data, we consider the BPC value for the EGCV, GCSL, and TBLC sources, as these are most diagnostic in the DZ comparison statistics we considered (e.g., Figure 12).

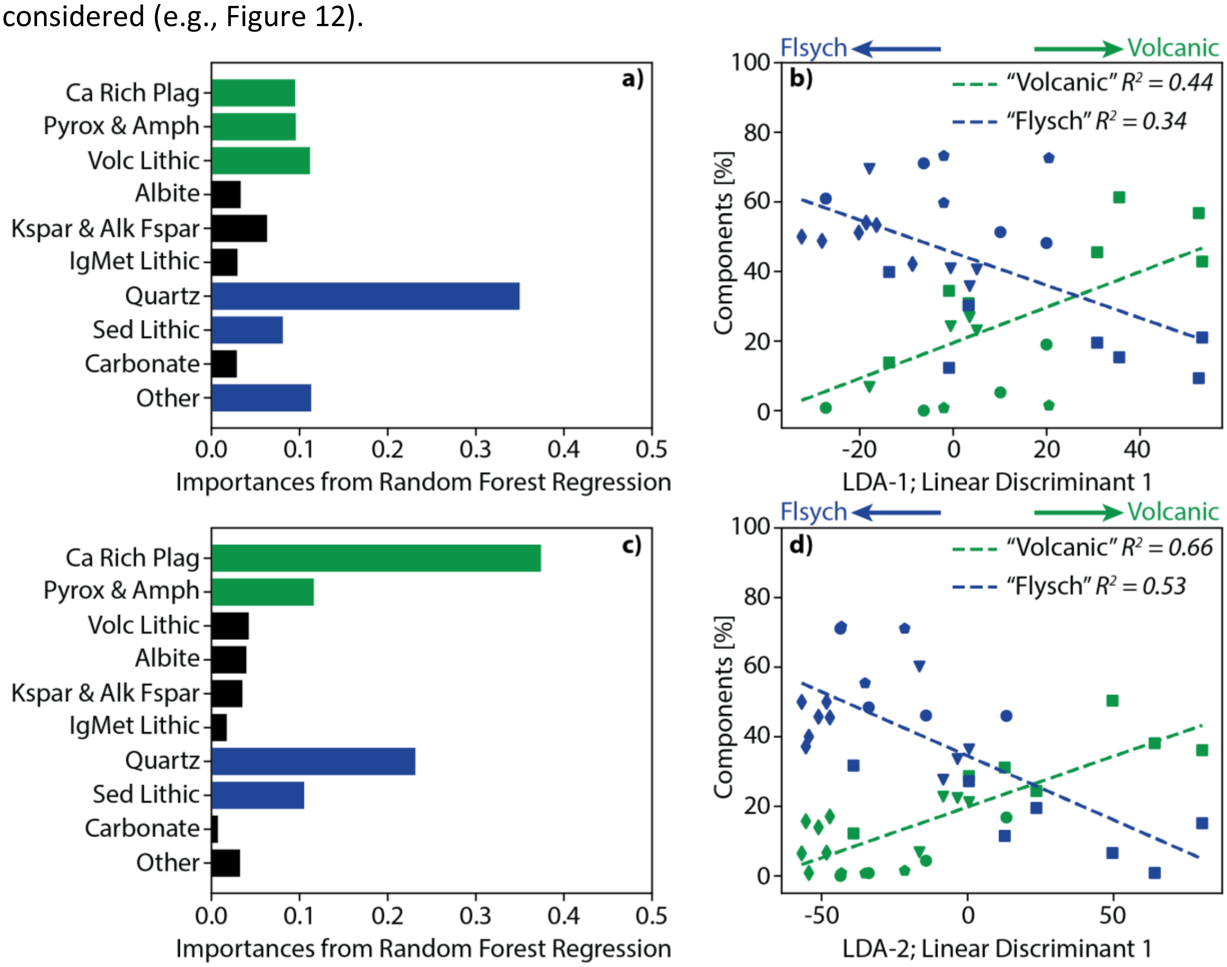

Figure 14 – Comparison of linear discriminant analyses of bulk geochemistry and point counts. a) Results of random forest regression that assesses the ability of a given point count category to predict the value of linear discriminant 1 within LDA-1. Green bars indicate components most associated with a "volcanic" source, and blue bars indicate components most associated with a "flysch" source. Black bars indicate these are components that are less diagnostic for distinguishing between sources. b) Plots and linear regressions between summed percentages of components related to either volcanic or flysch source as identified in 13a and linear discriminant 1 of LDA-1. c, d) Same as 13a but considering linear discriminant 1 for LDA-2.

The random forest regression highlights that the 6 most important components for LDA-1 are the calcium rich plagioclase, pyroxenes & amphiboles, volcanic lithics, quartz, sedimentary lithics, and the miscellaneous “other” components (Figure 14a). Comparing directly to linear discriminant 1 from LDA-1 suggests that the combined percentage of the first three components (calcium rich plagioclase, pyroxene & amphibole, and volcanic lithics) is positively correlated with LD1 whereas the combined percentage of the last three components (quartz, sedimentary lithic, and the generic “other” grains) is negatively correlated with LD1 (Figure 14b). This analysis is consistent with the former three components broadly being associated with a “volcanic” source and the latter three components associated with a “flysch” source. For LDA-2, the random forest regression is similar, but suggests that the “volcanic” source is predominantly defined by the calcium rich plagioclase and pyroxenes & amphibole components and that the “flysch” source is predominantly defined by the quartz and sedimentary lithic components. The linear relationships between these respective components and the value of linear discriminant 1 have higher correlation coefficients than in the LDA-1 result (Figure 14).

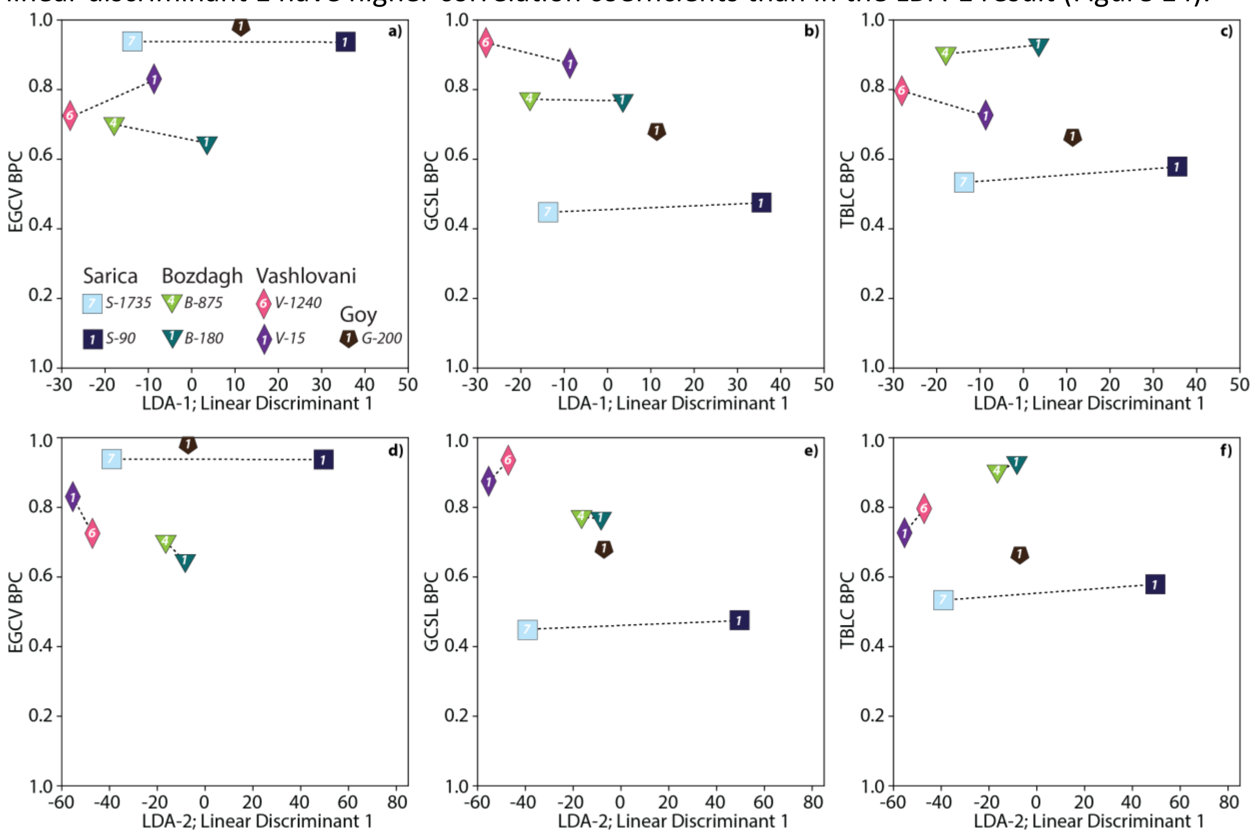

Figure 15 – Comparisons between linear discriminant analyses of bulk geochemistry and Bayesian population correlation of detrital zircon populations. We consider BPC values for the EGCV, GCSL, and TBLC sources as these are the best represented in the KFTB sandstones. a) Comparison of linear discriminant 1 from LDA-1 and BPCs with the EGCV source. b) Comparison of linear discriminant 1 from LDA-1 and BPCs with the GCLS source. c) Comparison of linear discriminant 1 from LDA-1 and BPCs with the TBLC source. d) Comparison of linear discriminant 1 from LDA-2 and BPCs with the EGCV source. e) Comparison of linear discriminant 1 from LDA-2 and BPCs with the GCLS source. f) Comparison of linear discriminant 1 from LDA-2 and BPCs with the TBLC source.

In contrast, comparing the LDA results and those from detrital zircon suggests relatively little relationship between the two (Figure 15). This comparison is more challenging to interpret because of the small number of samples that have DZ results compared to geochemistry or point counts, but broadly we see marginal differences between the top and bottom of sections in terms of DZ results, even for those that span a wide range in the LDA, e.g., Sarica. Depending on the particular DZ source considered, small trends can be observed, e.g., a positive correlation between EGCV BPC and LDA-1 and a negative correlation between GCSL BPC and LDA-1 for Vashlovani, but the magnitudes of the BPC differences are small compared to differences between sections, e.g., Sarica compared to Vashlovani. This comparison also highlights a similar result from comparing the geochemical and U-Pb DZ classification of the source terranes, specifically that samples that share similar geochemical classifications, e.g., the top of Sarica and both Vashlovani samples, can have strong affinities with different DZ sources (Figure 15).

7.1.3 Summary and Implications

While there are important nuances as discussed in the prior sections, broadly the comparisons between the different provenance methods suggest that; (1) results of the point counts and bulk geochemistry within a given section agree on a first-order history of sourcing for the Kura Fold-Thrust Belt samples, but (2) where available the detrital zircon results indicate a potentially different history of sourcing. Specifically, in terms of either point counts or bulk geochemistry, most of the locations exhibit an up-section shift from a predominantly volcanic and volcaniclastic source to a more flysch dominated source, whereas the detrital zircon analyses from the top and bottom of select sections mostly do not suggest comparable changes in source. There are several possible explanations for this disagreement, including (1) sediment recycling and selective weathering within the foreland basin; (2) climatically mediated preferential weathering of unstable components; (3) the non-unique source characterizations via different methods described in the previous sections; (4) sensitivity of different provenance methods to different components of the sediments themselves; or (5) biasing of detrital zircon signals by spatial variable erosion, fertility of source terrains, or other filtering processes. Ultimately, we favor the first option as the primary explanation, but we consider each of these in turn. In this, we largely focus on understanding the variation in the Sarica section as it is the most extreme.

The first, and our preferred, option suggests that the preserved provenance signals may in part reflect an up-section increase in sediment recycling such that the source of the sediment transitions from first-cycle (or less initially recycled) material eroded from the Greater Caucasus to increasing fractions of recycled versions of this same material as the Kura Fold-Thrust Belt develops. Of particular importance is that the primary components that appear to define the volcanic and volcaniclastic sources mineralogically and geochemically, e.g., calcium rich plagioclase, pyroxene, and amphibole, are also species that are expected to weather at rates several orders of magnitude faster than components that define the flysch source, e.g., quartz (e.g., Lasaga et al., 1994 and references therein). The potential importance of chemical weathering of these components is also consistent with prior work in the GC region, where Morton (2003) highlighted the importance of dissolution of clinopyroxene and amphiboles in Productive Series sediments in terms of considering potential sourcing. Thus, in the Sarica section, we envision a scenario where the base of the section, deposited prior to fold-thrust development, reflects sourcing from the Greater Caucasus and is a mixture of both the volcanic/volcaniclastic- and flysch-type sources, but based on the detrital zircons, likely dominated by the volcanic/volcaniclastic-type source, a point we return to in section 7.2. As portions of the fold-thrust belt north of the Sarica section began to deform, these progressively become a source of sediment for the Sarica region. As this occured, exposed rocks of a similar provenance to what is seen at the base of Sarica are weathered, eroded, and transported, resulting in the preferential breakdown of the components reflective of the volcanic/volcaniclastic source. As a result, fewer of these volcanic/volcaniclastic components are preserved up section, resulting in the up-section shift in point-count and geochemical signatures. However, the zircon signal from these recycled sediment remains effectively the same as the original source material from the GC. Additionally, growth of KFTB topography to the north of Sarica would likely begin diverting GC sourced rivers, limiting influx of new detrital zircons into the section. This explanation is also broadly consistent with the up-section increases in CIA values seen in Sarica and the majority of the other sections, though even at their extreme, the CIA values do not suggest deep weathering (Figure 9). It is thus viable that Xocashen and Goy, which on the basis of the point counts and geochemistry exhibit a similar up-section trend as Sarica, also reflect a transition from a GC source to a recycled, and more local GC-derived source within the KFTB. However, without comparable DZ data in Xocashen or Goy, this hypothesis is less definitive and highlights a need for future work. Finally, while we argue that sediment recycling is important for interpreting the provenance signal in the majority of our Kura Fold-Thrust Belt sections, it may not be dominant in all sections. Specifically, both Bozdagh and Vashlovani may reflect limited recycling. For Bozdagh, point counts, geochemistry, and U-Pb detrital zircon populations all suggest a similar history of sourcing throughout and the CIA values within Bozdagh are also largely similar throughout the section. Similarly, Vashlovani shows a change up-section in all three methods suggesting a diminishing volcanic and volcaniclastic source. It is in part these observations from Vashlovani and Bozdagh that cause us to prefer the sediment recycling explanation as opposed to a climatically mediated, regional increase in chemical weathering rates, the second option we discuss below.

The second option has some overlap with the first, but instead considers whether an up-section increase in climatic conditions conducive to intense chemical weathering could preferentially alter the provenance signals based on framework and certain heavy minerals and explain the discrepancy between these and detrital zircon ages. In our example, if climatically mediated weathering rates increased significantly between the timing of deposition of the basal sections compared to the top, this could potentially explain the divergence between the geochemical and point count and the DZ methods. The up-section increase in CIA (Figure 9) and other weathering indices (Figure S8) observed in many of the sections could also be consistent with this mechanism. However, in detail, there are challenges with this explanation. Paleoclimatic records within the KFTB are sparse, but from what is available in surrounding regions, it’s not clear that a climatic shift that would lead to more intense chemical weathering is coincident with the changes observed in the sections. In the Lokbatan section on the Apsheron Peninsula, compound-specific biomarkers indicate a gradual shift from dry and warmer conditions to cooler and more humid conditions from ~3.6 to 2 Ma (middle Productive Series to top the Akchagyl, Figure 3). While the increase in humidity could lead to increased weathering, we see the majority of change after the Akchagyl during the Apsheron and Baku (Figure 4, 9). During the Apsheron, sediments preserved along the northern flank of the Lesser

Caucasus, at the Damanisi hominin site (~44E) instead suggest an abrupt shift from warmer and wetter conditions to cooler and more arid conditions at 1.77 Ma (Messager et al., 2010a, 2010b) and subsequent increasing aridity (Kvavadze and Vekua, 1993; Gabunia et al., 2000). An analogous shift from more humid to arid conditions after the early Pleistocene is seen in palynological records from Shamb lake in Armenia, but spans a relatively narrow time range from 1.3 to 1.08 Ma (Joannin et al., 2010). While debate continues with respect to the exact interpretation of these climatic shifts (e.g., Blain et al., 2014) and changes in the LC climate do not necessarily imply the same changes in the KFTB climate, these would all broadly be inconsistent with a regional shift to more intense weathering conditions able to explain the up-section decrease in the volcanic and volcaniclastic component. Finally, in the context of this possible mechanism, it is important to note that not all of the sections exhibit the same weathering pattern (e.g., Bozdagh), which is inconsistent with regional climatic change as the fundamental controlling mechanism.

For the third option, it is difficult to rule out that some portion of the disagreements between DZ versus point counts and geochemical methods reflect that source definitions are not the same. However, the degree of difference in both a spatial and temporal sense, is hard to attribute completely to this effect. For example, in Sarica, given the clear geochemical affinity between the upper portions of this section and a flysch source, it is hard to reconcile a DZ source that seems to be completely volcanic and volcaniclastic (EGCV) solely based on differences in source definitions (Figure 15).

The fourth option is that the disagreement between DZ and geochemical or point count methods relates to the sensitivity of these different techniques to different parts of the provenance signal (e.g., Pe-Piper et al., 2008; Malkowski et al., 2019). However, the level of agreement between point counts, which primarily reflect framework grains and major phases, and the geochemical classifications via trace elements, which tend to largely reflect the heavy mineral fraction (e.g., Pe-Piper et al., 2008), is not consistent with fundamentally different signals being recorded in framework vs heavy mineral grains, the latter of which the detrital zircons would be a part (e.g., Figure 14). This in part also depends on the makeup of the original heavy mineral fraction, i.e., is it dominated by refractory minerals like zircon or does it have large percentages of heavy minerals more prone to weathering. Similarly, while it is not uncommon for provenance signals from detrital zircons and geochemical methods to vary within the same sediment package, this is more often the case when these two methods are applied to sediments of substantially different grainsizes, e.g., sandstones vs mudstones (e.g., Malkowski et al., 2019). In our case, the analyses were mostly preformed on the exact same samples, and in all cases targeted sandstones of similar grain sizes.

A fifth and final option is that the DZ records within the foreland specifically may reflect biasing from either (1) differential erosion rates of sources, (2) differences in fertility of zircons within the contributing sources (e.g., Amidon et al., 2005b, 2005a; Malkowski et al., 2019), or (3) hydrodynamic fractionation of age populations on the basis of grain size or shape (e.g., Garzanti and Andò, 2007; Lawrence et al., 2011; Ibañez-Mejia et al., 2018; Malkowski et al., 2019). However, none of these processes seem likely in the Kura Basin example. In terms of fertility, considering the zirconium concentration in flysch vs volcanic and volcaniclastic modern rivers as a proxy (e.g., Malkowski et al., 2019), does not reveal systematic differences (Table S3). To return to the Sarica example, the persistence of a volcanic and volcaniclastic like DZ source at the top of the section despite a shift to a more flysch like source from the other methods would require that the volcanic and volcaniclastic sources have a greater concentration of zircons (and thus zirconium) than rivers draining primarily flysch. However, the data suggest the opposite, with rivers draining the flysch generally having slightly higher zirconium concentration (Table S3). Alternatively, differential erosion where the volcanic and volcaniclastic sources would be expected to erode faster to contribute more sediment and thus dominate the DZ signal, also does not appear to be a robust explanation. In the modern GC, the volcanic and volcaniclastic sources largely appear along the extreme southern edge of the range (Figure 1), but recent decadal (Vezzoli et al., 2014, 2020), millennial (Forte et al., 2022b) and long-term exhumation rates (Forte et al., 2022a) from throughout the GC all largely suggest that exhumation rates are at a minimum along the flanks and increase toward the center of the range. Further, this would still require differences in zircon fertility between the sources given the clear geochemical and framework grain shift toward a more flysch like source. Finally, there are not clear correlations between grain size or shape and either distinct age populations or particular sources (Figure S9), suggesting that hydrodynamic fractionation is not a likely explanation for the dominance of the EGCV source within Sarica. In detail, the distribution of zircon sizes in the volcanic or volcaniclastic samples are skewed slightly toward larger grains and zircon sizes in flysch samples are skewed slightly toward smaller grains, but the bulk of the grains from both sets of sources overlap and there is no clear pattern in terms of grain shape (Figure S9).

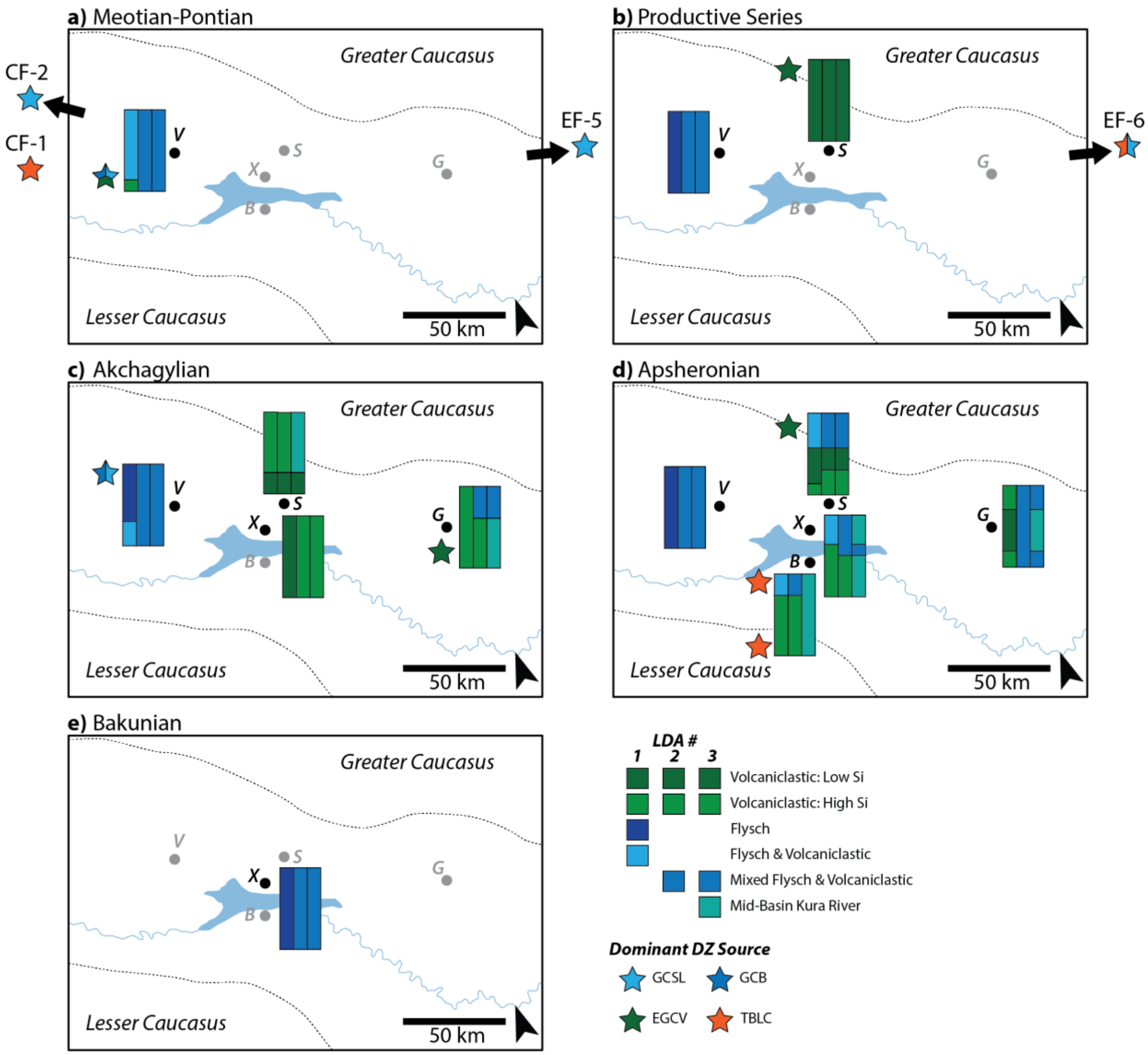

Figure 16 – Summary of provenance changes through time and space as indicated by both geochemistry and detrital zircons during a) Meotian-Pontian, b) Productive Series, c) Akchagylian, d) Apsheronian, and e) Bakunian stages. Map is focused on central KFTB samples and sections, but results from samples from Tye et al., (2020) outside of this region are shown schematically. Grayed out section locations reflect that there is no data for that time period from that section. Note that this map is not palinspastic and does not reflect that the distances between sections and the GC or LC rangefronts would have been different at the time of deposition.

7.2 Implications for Greater Caucasus and Kura Fold-Thrust Belt Tectonics

Visualization of changes in sourcing through time and space presented in Figure 16 provide a framework within which to consider the evolution of sediment provenance in the Kura Fold-Thrust Belt. We consider this as a function of individual regional stages between the Meotian and Bakunian, and integrating additional DZ samples from Tye et al., (2020) where relevant. Finally, we summarize our preferred interpretation of the implications of the provenance for GC and KFTB tectonics, with a focus on the across-strike traverse of sections from Sarica, Xocashen, and Bozdagh (Figure 16).

7.2.1 Meotian-Pontian

Vashlovani is the only location that includes a record of the Meotian-Pontian within our measured sections. The base of Vashlovani reflects a mixed flysch and volcanic or volcaniclastic source, specifically with a dominant EGCV DZ signature, with some indication of a potential reduction of the volcaniclastic component up-section within the Meotian-Pontian. At present, regions directly north of Vashlovani within the GC rangefront expose very limited amounts of volcanic or volcaniclastic material (Figure 1), suggestive of either there being a larger exposure area of these volcanic or volcaniclastic materials during the Meotian-Pontian, enhancement of the volcanic or volcaniclastic components via excess erosion in these units, or lateral transport from areas exposing more of these units in the GC range front.

Outside of the sections, at the western (CF-2) and eastern (EF-5) tips of the KFTB, undifferentiated Meotian-Pontian and Pontian sediments, respectively, record a predominantly flysch source with a GCSL DZ signature during this time period (Tye et al., 2020). Without a clear sense of where, stratigraphically, CF-2 is located with respect to the Meotian-Pontian samples within Vashlovani, it is difficult to compare the implications of the differences between the sourcing of this sample, but for EF-5, given its Pontian depositional age, suggests a more exclusively flysch type source compared to Vashlovani during the same approximate time period. At the western terminus of the KFTB and considering sample CF-1 from the middle Miocene that precedes the Meotian-Pontian, we see a potentially similar up-section change from a more volcanic/volcaniclastic source to more flysch dominated source by the deposition of CF-2 (Tye et al., 2020). Importantly however, based on BPCs presented by Tye et al., (2020), CF-1 seems more similar to a Lesser Caucasus (TLBC) derived source than either of the GC volcanic or volcaniclastic DZ sources. Tye et al., (2020) suggest that the presence of a Lesser Caucasus affiliated source in CF-1 reflects material that when deposited was more proximal to the Lesser Caucasus, but has subsequently translated toward the Greater Caucasus via north directed underthrusting of Kura Basin lithosphere beneath the GC. This remains a viable and likely hypothesis, but given the clear geochemical relationships between the Lesser Caucasus volcanics and volcaniclastics and those exposed at least in the eastern Greater Caucasus (e.g., Figures 5, 7), an alternative hypothesis is that there was sufficient variability in a formerly larger thrust slice of volcanic and volcaniclastic material within the GC rangefront that zircons sourced from this thrust sheet could in part look more like those preserved in the surficial Lesser Caucasus today. More detailed stratigraphy in the region around the Gombori Range, and specifically information on paleo-currents, could help to clarify this point, i.e., do the strata from which the CF-1 sample comes record a dominantly south directed (GC sourced) or north directed (LC sourced) paleocurrents? Similarly, a better sense of the volcanic stratigraphy within the Jurassic and Cretaceous Lesser Caucasus could provide an indication of whether there are regions of similarly mono-age peaks like we see in the volcanic and volcaniclastic sources within the GC.

Deposition in Vashlovani and elsewhere during the Meotian-Pontian (~7 to 5.5 Ma) is coincident with increases in exhumation rate observed throughout the Greater Caucasus between ~10-5 Ma (e.g., Avdeev and Niemi, 2011; Vincent et al., 2020; Forte et al., 2022a; Tye et al., 2022). This similarity of timing is broadly consistent with the idea that the onset of rapid exhumation of the GC prior to the Meotian-Pontian had established the GC as a dominant sediment source for regions within the southern foreland (e.g., Tye et al., 2020).

7.2.2 Productive Series

Both Vashlovani and Sarica record portions of the Productive Series, but they suggest relatively different sourcing at this time (Figure 16b). Vashlovani records a dominantly flysh source, but with some limited volcanic and volcaniclastic input remaining. In contrast, Sarica is almost exclusively sourced from volcanics and volcaniclastics with an EGCV detrital zircon signature. Present-day catchments north of Sarica within the GC reflect mixtures of the volcanic and flysh type sources, so the dominance of volcanic/volcaniclastic input in the Productive Series within Sarica appears to require greater proportions of this source at the time of deposition than is seen today, similar to the lower part of Vashlovani. Again, explanations for this pattern are either a physically larger exposure of the volcanic and volcaniclastic source within the southern range front at the latitude of Sarica, lateral transport from an area of the GC rangefront with a larger volcanic package, or enhanced erosion of this source during Productive Series time.

Near the eastern terminus of the KFTB, Productive Series sample EF-6 from Tye et al., (2020) records a mixed affinity with both Lesser (TBLC) and Greater Caucasus (GCSL) DZ sources, but here we consider whether EF-6, like its central KFTB counterparts, might instead reflect sourcing from the GC, not the LC. Tye et al., (2020) interprets the TBLC component to reflect eastward transport of Lesser Caucasus material, either directly from the Lesser Caucasus via an axial drainage or erosion of Kura Basin sediments, most likely related to the coincident draw down of the Caspian Sea (e.g., Popov et al., 2006, 2010; Krijgsman et al., 2010; Forte and Cowgill, 2013; van Baak et al., 2017) and resulting incision by the Kura River (e.g., Kroonenberg et al., 2005). However, at present, both Vashlovani and Sarica are at a greater distance from the GC range front than EF-6 (e.g., Figure 1, 13) and thus it is strange that EF-6 would reflect transport from the Lesser Caucasus or incised Kura Basin sediments while both Vashlovani and Sarica were dominantly sourced from the GC at this same time. Tye et al., (2020) largely follows suggestions from Morton et al., (2003) of a paleo-Kura river almost exclusively sourced from the Lesser Caucasus and that was located relatively near the GC rangefront, but this contradicts evidence of an entrenched Kura paleo-canyon near the modern axis of the basin during Productive Series time (e.g., Kroonenberg et al., 2005). In detail, the interpretation of a LC source for eastern KB Productive Series sandstones from Morton et al., (2003) relies primarily on the presence of unstable components within the heavy mineral assemblages of these samples, including abundant clinopyroxenes, amphiboles, and epidotes. The similarity between these assemblages and the modern and paleo-Kura River sourced Productive Series sandstones led Morton et al., (2003) to argue that the PS sandstones necessarily must be sourced from the Lesser Caucasus. Morton et al., (2003) do report heavy mineral assemblages from rivers draining the eastern tip of the Greater Caucasus that contain significant proportions of amphibole, epidote, and clinopyroxene, but in lesser amounts than in the modern Kura River, with more stable minerals (e.g., feldspar, quartz) dominating the extreme eastern Greater Caucasus assemblages. Morton et al., (2003) attribute the higher abundance of stable minerals in the Greater Caucasus rivers to the presence of Jurassic and Cretaceous sediments within the catchments and suggest that the presence of the unstable minerals may be due to recycling of

Paleo-Kura sourced Productive Series sediments from portions of the river catchments containing these rocks. However, our analysis suggests that the Vandam domain of the southeastern Greater Caucasus proper also may contribute to these heavy mineral assemblages indicative of more mafic, less evolved source terranes, as such, the underlying association of these unstable components necessarily with a LC source, at least on the basis of heavy minerals alone, is questionable.

To fully reconcile the apparently contradictory results of a potential sourcing of central KFTB sandstones during Productive Series time from the southern margin of the GC coincident with eastern KFTB sandstones from the LC would require; (1) palinspastic restoration of the positions of the Sarica, Vashlovani, and EF-6 locations during Productive Series time – in turn requiring estimates of shortening within the respective regions of the GC and KFTB, (2) constraint on the location of the GC rangefront along-strike during Productive Series time, and (3) ideally some independent constraint on the first order drainage-network structure within the foreland basin during Productive Series time beyond the location of the trunk Kura River. Generally, none of these details are sufficiently constrained to fully resolve this question, but we again highlight that more zircon age variability in a former and larger GC hosted volcanic and volcanic source could be an alternative and parsimonious explanation for the observations during the Productive Series in EF-6.

Focusing on the Sarica and Vashlovani sections, we interpret the dominance of GC provenance and the coarseness of the Productive Series deposits to result from continued rapid exhumation of the GC and progradation of coarse clastic materials into the foreland basin (e.g., Burbank et al., 1988; Allen and Heller, 2012). The depositional character of these deposits also likely reflects the regional context of the coincident Caspian lowstand (e.g., Forte et al., 2015a). The one Productive Series sample from Vashlovani is notable for (1) being largely devoid of lithic grains, (2) a reduction in lithic components (Figure 4), and (3) a temporary increase in CIA (Figure 9), all of which are consistent with an increase in reworking or weathering. This could reflect local reworking resultant from deformation and uplift of Kura Basin sediments, i.e., initiation of the KFTB, but given that these changes are short lived and that overlying basal Akchagylian sediments look very similar to underlying upper Meotian-Pontian sediments in Vashlovani (e.g., Figure 4, 8), we favor an explanation related to the unique Caspian low-stand during the Productive Series deposition and potentially increased weathering during this period.

7.2.3 Akchagylian

The Akchagylian is present in Vashlovani, Sarica, Xocashen, and Goy (Figure 16c). With the exception of Vashlovani, all sections show a strong affinity for volcanic and volcaniclastic sources near their base and with Goy specifically showing affinity to an EGCV DZ source. In both Sarica and Goy, up-section toward the Apsheron boundary, there is a slight decrease in this volcanic and volcaniclastic source as indicated by point counts and geochemistry. This is not seen within Xocashen, but the Akchagyl-Apsheron boundary is not captured within our sampled stratigraphy there. Similar to other sections, the base of Goy which shows a strong affinity with a volcanic or volcaniclastic source both geochemically (Figures 6, 8, 9) and in terms of detrital zircons (Figure 11, 12) is at odds with modern geology, where the portion of the GC rangefront north of Goy is an embayment largely devoid of volcanic and volcaniclastic material, which could be explained similarly as in other samples described previously.

In Sarica, the marked decrease in volcanic and volcaniclastic components, especially noticeable in the point counts (Figure 4), but also detected geochemically (Figures 6, 8, 9), could either reflect (1) a decrease in the contribution of volcanic and volcaniclastic inputs reflecting a decrease in the importance of this source within the GC at the longitude of Sarica or (2) the beginning of sediment recycling reflective of initiation of KFTB structures north of Sarica and reduction in the volcanic and volcaniclastic component through weathering of unstable phases as described previously. Presumably, detrital zircon ages from this horizon would help to constrain these options, i.e., if the DZ signature remained dominated by EGCV zircons this would suggest sediment recycling, whereas if the DZ signature began to reflect more GCSL or other non-volcanic GC inputs, this would support a decreasing extent of an EGCV source along the southern range front. In the absence of this data, we instead consider the regional tectonic context of the KFTB to help narrow the options. Further west within the KFTB, the Akchagyl may reflect the initiation of deformation (e.g., Sukhishvili et al., 2020), but the potential time range also includes much of the Apsheron (e.g., Figure 3). Similarly, Vashlovani during the Akchagyl, which is in a somewhat similar structural position within the KFTB as Sarica, seems to still record sourcing from the GC as opposed to more local KFTB, i.e., recycled GC, sources. This is exemplified by the geochemistry (Figures 6, 8, 9) and detrital zircon (Figure 11, 12) sample(s) during the Akchagyl reflecting a consistent change up-section to a reduced volcanic and volcaniclastic input, and point counts that still suggest volcanic and volcanic clastic inputs (Figure 4). Thus, for Sarica, we favor an explanation for provenance during the Akchagyl as still recording sourcing primarily from the GC. This would imply that the timing of KFTB initiation at the longitude of Sarica likely occurs after the Akchagyl and that the change in provenance from the Productive Series to Akchagyl, reflects a reduction in flux of the volcanic and volcaniclastic source area from the GC.

7.2.4 Apsheronian and Bakunian

The Apsheronian is represented in all measured sections (Figure 16e), though the extent of its exposure in Vashlovani is uncertain considering the unclear boundary between the Akchagyl and Apsheron in this location (Figure 3). Through the duration of the Apsheron, geochemistry and point counts suggest that Sarica, Xocashen, and Bozdagh all show decreases in volcanic or volcaniclastic components. This is also broadly coincident with an up-section coarsening in all three columns. However, in Xocashen much of that coarsening occurs after the Apsheron, during the Baku period, and the coarsening in Bozdagh is not as pronounced as in the other two sections. For both Sarica and Xocashen, we interpret these up-section changes as most likely reflecting initiation of the KFTB. For Sarica, this would suggest that structures north of the section location likely began to exhume sometime during the early Apsheron (Unit S3) or possibly across the Akchagyl-Apseron boundary, similar to the timing of initiation of deformation in the Goy region (Forte et al., 2013; Lazarev et al., 2019). For Xocashen, coarsening and reduction in the volcanic and volcaniclastic component occurred later in the Apsheron and/or into the Baku compared to Sarica. This later timing in Xocashen could reflect either a delay related to coarse clastic progradation or that the Sarica fold itself, which is the structure directly north of and across the Adjinour playa from Xocashen, initiated and began to exhume, providing material for southern regions. In the latter case, this would suggest in-sequence propagation, from the structure north of Sarica during the early Apsheron followed by Sarica during the later Apsheron and into the Baku (Figure 16).

While Bozdagh shows a reduction in volcaniclastic source components and a slight coarsening upwards, the relatively consistent interpretation of a deltaic environment and TBLC DZ signatures at the top and bottom of the section do not further constrain KFTB initiation. Instead, the provenance of Bozdagh suggests that it was likely sourced by a river not unlike the modern Kura or other present day axial rivers, i.e., an east flowing longitudinal river that drains both the GC and LC (Figure 16). As such, the reduction up-section of the volcanic and volcaniclastic component in Bozdagh could reflect a broad reduction in the exposed area of volcanic and volcaniclastic sources in the GC. From paleocurrent data in the western terminus of the KFTB, we know that the development of the KFTB itself significantly perturbed the foreland drainage network as former south flowing rivers were defeated and reversed to drain into the piggy-back Alazani basin during the Akchagyl-Apsheron period (Sukhishvili et al., 2020). Thus, if Bozdagh represents a paleo-Kura like drainage, then the up-section changes in provenance in the Bozdagh section could also reflect progressive sequestering in the KFTB and nascent Alazani basin of material derived from the southeastern GC throughout the Apsheron.

Finally, in Goy, the angular conformity between Akcaghyl and Apsheron sediments is thought to date the timing of initiation in the KFTB at this longitude (Forte et al., 2013; Lazarev et al., 2019). By the base of the Apsheron, the provenance of Goy appears to be dominated by flysch type sources, though coupled with the coarsening upward seen from unit G2-A to G2-B and unit G3 in Lazarev et al., (2019), the independent constraint on the KFTB having initiated by that point suggests this could also be a recycling signal. Detrital zircon data from higher in the Goy section would likely clarify whether this is the case.

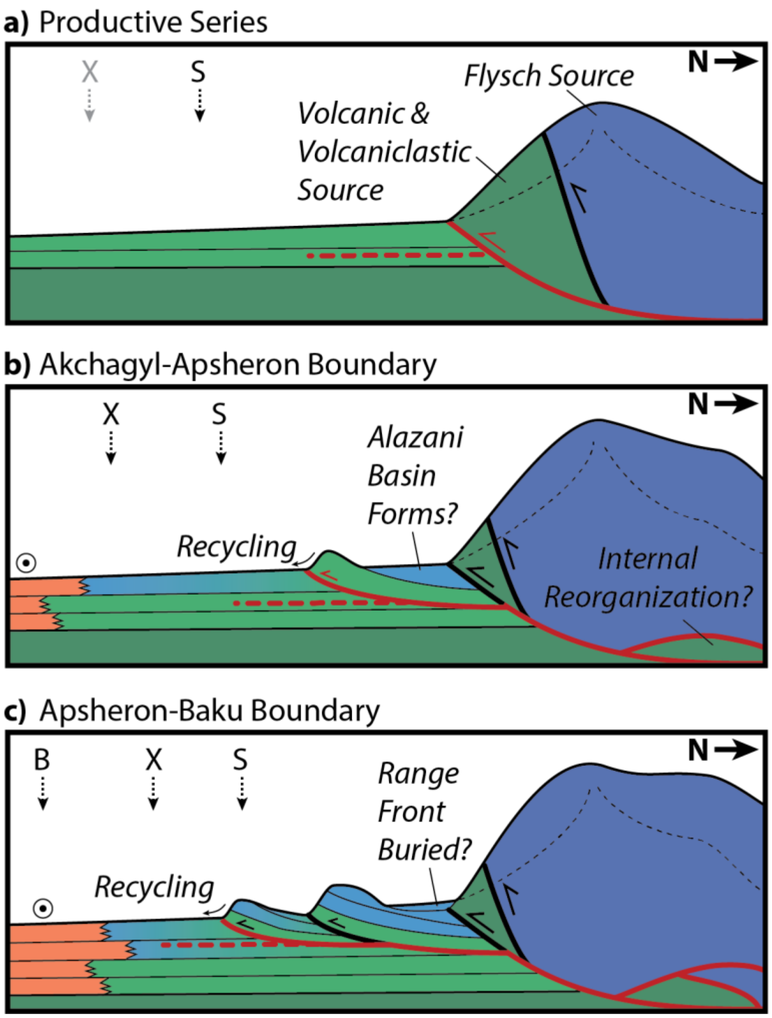

Figure 17 – Schematic cross-sections through the central KFTB during the a) Productive Series, b) Akchagyl-Apsheron boundary, and c) Apsheron-Baku boundary. Diagram is not to scale, but we schematically depict advection of the sections toward the GC via continued underthrusting and reduction in distance between sections as KFTB structures initiate and accommodate shortening. Grayed out section locations indicate there is no data for that time from that section. Approximate location of Bozdagh (B), Xocashen (X), and Sarica (S) measured sections are shown. Blue colors indicate flysh sources or stratigraphy that appears to be sourced from flysch, green colors indicate volcanic/volcaniclastic sources, and orange indicated sourcing from the mixed GC and LC as seen in Bozdagh or the modern Kura River. The concentric circle indicates approximate location of axial drainage (Kura River).

7.2.5 Summary of Tectonic Implications from Provenance

Figure 17 summarizes our preferred sequence of events within the central KFTB at the longitude of the Sarica, Xocashen, and Bozdagh sections based on the new provenance data and prior work. During the Productive Series, the southern rangefront of the eastern GC exposed a mixture of thrust-bounded sections of volcanic and volcaniclastic rocks, overlain by, and in thrust contact with flysch (Figure 17a). We hypothesize that at this time, the range-front fault thrusting Mesozoic volcanics over Cenozoic basin fill was the primary active structure in the range, prior to the development of the KFTB. This model does not preclude other structures from being active at the time and we do not have direct constraint on history of any of the individual structures within the GC that we consider here from our data, but the localization of deformation near the rangefront is consistent with in-sequence propagation of structures and the subsequent evolution of the system as we interpret below from the provenance data.

Moving into the Akchagyl and basal Apsheron, exposure of the volcanic and volcaniclastic rocks progressively decreases as the thrust slice(s) that contain these rocks are exhumed and eroded via south-directed thrusting along the rangefront fault system(s). On the basis of the provenance and stratigraphy, it is at this time that we suggest deformation began to propagate into the foreland, initiating the KFTB and formation of the Alazani basin (Figure 17b). This implies broadly synchronous timing for KFTB initiation along strike, with Akchagyl to basal Apsheron initiation at the longitude of Sarica, Xocashen, and Bozdagh matching KFTB initiation estimated both to the west (Sukhishvili et al., 2020) and east (Forte et al., 2013; Lazarev et al., 2019). Synchronous initiation along strike is contrary to previous suggestions of east-younging diachronous initiation that was inferred from sparse data (e.g., Forte et al., 2010). Based on recent comparisons of low-temperature thermochronology and ^{10}Be exhumation rates (Forte et al., 2022a), Akchagyl to basal Apsheron initiation of the KFTB is coincident with a larger structural reorganization within the range that caused deformation within the interior of the GC to expand to the north, possibly related to duplexing at depth along the basal GC thrust system (Forte et al., 2015b). In addition, initiation of the KFTB likely resulted in initial slowing of activity on the rangefront fault system and the onset of increasing embayment of the rangefront via erosion and burial as the Alazani piggyback basin began to fill (e.g., Forte et al., 2010; Mosar et al., 2010).

Finally, we interpret that later in the Apsheronian and moving into the Baku stage, the Sarica fold itself likely began to form, providing coarser grained and further recycled material to be deposited southward in Xocashen (Figure 16c). Such timing implies in-sequence propagation of the KFTB at this longitude, which contrasts with the out-of-sequence propagation seen in portions of the eastern terminus of the belt (Forte et al., 2013) and GC (Tye et al., 2022). Throughout the depositional history, we suggest that Bozdagh experienced deposition from a paleo-Kura like axial drainage. This axial drainage subsequently entrenched between the Bozdagh and Xocashen folds sometime during the Baku stage or later, when both the Xocashen and Bozdagh folds began to form, but our data do not provide direct constraints on the timing of either of these structures other than we would assume they initiate during the Baku or post-Baku.

Ultimately, our preferred sequence of events within the KFTB is consistent with recent work suggestive of more synchronous initiation of the KFTB along strike (Forte et al., 2013; Lazarev et al., 2019; Sukhishvili et al., 2020) and thus is consistent, at least in a structural sense, with widening of the orogen in response to a regional shift to more arid conditions (Whipple and Meade, 2004, 2006; Forte et al., 2013). However, it remains unclear if a climatically induced widening also explains the potentially coincident internal structural reorganization and northward shift of the locus of exhumation within the GC (Figure 17; e.g., Forte et al., 2015b, 2022a). Internal deformation within the orogen coincident with widening is not an unexpected in response to either changes in taper angle (e.g., Whipple and Meade, 2004, 2006; Hoth et al., 2006) or as part of accretion cycles (e.g., Hoth et al., 2007), but establishing the coincidence of KFTB initiation and internal GC reorganization requires better timing of both, especially the internal reorganization. Remaining uncertainty in the exact timing of initiation of the central

KFTB structures along the traverse between Sarica and Bozdagh could be reduced via infilling the detrital zircon geochronology record.

Our results highlight that multiproxy sediment provenance work, paired with additional stratigraphic and structural characterization of regions within the KFTB, has a high probability of constraining the timing of initiation throughout the thrust belt. Such additional timing information is important for clarifying the drivers of fold-thrust belt initiation and deformation front expansion within the GC. In contrast, tying the structural changes to a potential climatic trigger for initiation requires more paleoclimatic context for the KFTB sediments.

7.3 Implications for Provenance Studies in Forelands

More broadly, results of our work provide some general insights for sediment provenance investigations within other foreland fold-thrust belts. Detrital zircon U-Pb geochronology is unquestionably the go-to method for sediment provenance investigations across a range of tectonic settings (e.g., Gehrels, 2014; Žák et al., 2020; Jian et al., 2022). However, this method is not without challenges in terms of uniquely interpreting the provenance history while accounting for sources of biases or complications (e.g., Cawood et al., 2003; Amidon et al., 2005a; Andersen, 2005; Link et al., 2005; Lawrence et al., 2011; Raines et al., 2013; Spencer et al., 2018; Malkowski et al., 2019). The results of our analysis echo those of other recent work (e.g., Malkowski et al., 2019), namely that interpretation of detrital zircon geochronology is the most robust when done in concert with other indicators of sediment provenance. In our particular example, the inclusion of point counts and bulk rock geochemistry are critical for recognizing the potential role of sediment recycling within the KFTB, and further provide constraint on the timing of initiation of the belt – a conclusion that would most likely not be apparent from DZ U-Pb populations alone. The specific details largely relate to the local geology of the region in question, i.e., the association of particular zircon populations and sources with unstable mineral components, but the underlying implication remains, which is that pairing DZ analyses with other provenance methods helps to both avoid misinterpretation of the DZ results while also providing additional insight into the tectonic history of actively deforming regions. One of the reasons for the propagation of DZ as an effectively default provenance method, beyond the ubiquity and durability of zircons in many sediments, is the relative ease and low cost of the analyses (e.g., Gehrels, 2012). In this respect, we emphasize that bulk rock geochemistry of either the same sandstone samples used for DZ geochronology, as we present here, and/or interbedded mudstones (e.g., Pe-Piper et al., 2008; Malkowski et al., 2019) represents a similarly easy and cost effective provenance technique that pairs well with DZ geochronology, and may reveal additional details of the provenance and interpreted tectonic history from forelands.

8. CONCLUSIONS

The results of our multiproxy provenance analysis of Kura Fold-Thrust Belt sandstones and potential source regions within the Greater and Lesser Caucasus help to clarify the structural evolution of both the southeastern Greater Caucasus and Kura-Fold-Thrust Belt. In addition, these data provide additional context and considerations for future provenance work within the Kura Basin or Fold-Thrust Belt. Notable conclusions from this work include:

1. Source characterization, and thus resulting indications of sediment provenance within the foreland, from point counts, bulk major and trace element geochemistry, and detrital zircon geochronology broadly overlap, but have some important differences. Source terranes defined on the basis of geochemistry or framework grains span geographically broader regions than those defined by detrital zircon populations. Specifically, while prior work characterizing detrital zircon source terranes identifies 7 distinct sources, we are able to differentiate on 4 using sediment geochemistry. The four sources comprise one pair of broadly flysch-dominated sources that also include exposures of GC basement and pre-flysch sedimentary packages and a second pair of broadly volcanic and volcaniclastic dominated sources that include exposures of both the Vandam zone within the eastern Greater Caucasus and rivers draining the Lesser Caucasus.
2. Despite the expectation that point counts and bulk trace element geochemistry should be sensitive to different components of the provenance signal, within the Kura Fold-Thrust Belt sandstones at least, these two methods are broadly correlative and provide similar information with respect to potential provenance histories. This suggests that with respect to these two methods, future provenance work in the Kura Fold-Thrust Belt could largely focus on inclusion of bulk trace element geochemistry, which is a substantially less work intensive methodology than point counts.
3. The majority of Kura Fold-Thrust Belt sections record an up-section change in apparent provenance from a more volcanic and volcaniclastic like source to a more flysch like source on the basis of geochemistry and point counts. In contrast, U-Pb ages from detrital zircons suggest relatively minimal changes between the bottom and top of sections, and instead reveal different sourcing between the sections. We interpret that the divergence between the provenance methods in part reflects an up-section increase in sediment recycling and local reworking related to initiation of structures within the belt, and as such, can be used to estimate the timing of the initiation of the Kura Fold-Thrust Belt.
4. Integrating provenance changes from the different methods suggests that before the Akchagyl-Apsheron boundary (~2.1 Ma), a progressive up-section reduction in the volcanic and volcaniclastic component observed within the Kura Fold-Thrust Belt reflects a progressive decrease in the spatial extent of this source in southeastern Greater Caucasus. We interpret this decrease over time to reflect progressive exhumation and erosion of a thrust-bounded slice(s) of the Vandam and equivalent rocks along the rangefront fault system.
5. After the Akchagyl-Apsheron boundary, we interpret the diminishing volcanic and volcaniclastic component to reflect the onset of Kura Fold-Thrust Belt deformation within the central part of the belt, where the mafic to intermediate, unstable components diagnostic of the volcanic and volcaniclastic source terranes are selectively weathered during recycling and local reworking. This implies that the initiation age of the central Kura Fold-Thrust Belt overlaps with timing constrained in the western and eastern termini of the belt and further indicating that the belt initiated nearly synchronously along-strike.

6. Finally, the results from the Kura Fold-Thrust Belt highlight the utility of pairing diverse sediment provenance methods within actively deforming regions as this may allow both for better characterization of potential biases and complications that could otherwise hinder correct interpretation, but also have the potential to expand the ability to recognize important drivers of provenance change.

ACKNOWLEDGEMENTS

We thank Boris Avdeev, Zak Murturzayev, Tea Mumladze, Ana Menabde, David Kandelaki, Christian van Baak, and Iuliana Vasiliev with help in collecting the samples presented here. We additionally thank Tea Godoladze, Misha Elashvili, Zurab Javakhishvili, Talat Kangarli, and Ibrahim Murturzayev for assistance in accessing the field areas and general logistic support. We thank Christopher Campisano for the use of his lab facility at ASU for processing the ash samples for tephra geochemistry, Axel Wittmann for his assistance during microprobe analyses at ASU, Sarah Roeske for her assistance during microprobe analyses at UC Davis, and the staff of the U of A LaserChron facility for their assistance during the detrital zircon analyses. Finally, we thank Charles Trexler and Alex Tye for helpful conversations regarding the provenance of sediments and their structural context within the Greater Caucasus region. This material is based upon work originally supported by National Science Foundation grants EAR-0810285 (Cowgill), with additional funding provided to Forte by NSF grant EAR-1450970, the UC Davis Department of Geology Cordell Durrell Fund, Geological Society of America, and American Association of Petroleum Geologists. Manuscript preparation was supported by NSF grants EAR-1524631 and EAR-2050623 (Cowgill).

TABLE CAPTIONS

Table 1 – Coordinates of top and bottom the measured sections.

Table 2 – Coordinates of provenance samples including original sample names, sample names used in the manuscript, and the analyses performed (G – bulk geochemistry, PC – point counts, DZ – detrital zircon U-Pb geochronology).

Table 3 – Coordinates of ash samples and means and standard deviations of major elements of the ash shards extracted from the ash samples.

Table 4 – Summary point count and modal mineralogy results.

Table 5 – Samples and references for those samples used to define composite DZ sources

Table 6 – Perkins statistical distance between ash samples from within measured sections

Table 7 – Element ratios used in Figures 5 and 6.

Table 8 – LDA values for source samples and resultant source designations.

Table 9 – LDA values for KFTB samples and resultant source classifications.

Table 10 – Results of unmixing source populations using DZmix.

REFERENCES

Abdullaev, R.N., Agabekov, M.G., and Gavrilov, M.D., 1957, K-38-XXIX: Geological map of the USSR.

Abdullayev, N.R., Weber, J., van Baak, C.G.C., Aliyeva, E., Leslie, C., Riley, G.W., O'Sullivan, P., and Kislitsiyn, R., 2018, Detrital zircon and apatite constraints on depositional ages, sedimentation rates and provenance: Pliocene Productive Series, South Caspian Basin, Azerbaijan: Basin Research, p. 1–28, doi:10.1111/bre.12283.

Adamia, S., Alania, V., Chabukiani, A., Kutelia, Z., and Sadradze, N., 2011a, Greater Caucasus (Cavcasioni): A long-lived North-Tethyan Back-Arc Basin: Turkish Journal of Earth Sciences, v. 20, p. 611–628.

Adamia, S., Lordkipanidze, M.B., and Zakariadze, G.S., 1977, Evolution of an active continental margin as exemplified by the alpine history of the Caucasus: Tectonophysics, v. 40, p. 183–199.

Adamia, S., Zakariadze, G.S., Chkhotua, T., Sadradze, N., Tsereteli, N., Chabukiani, A., and Gventsade, A., 2011b, Geology of the Caucasus: A Review: Turkish Journal of Earth Sciences, v. 20, p. 489–544.

Agabekov, M.G., Kerimov, K.M., Moshashvili, A.B., and Khain, V.Ye., 1976, New data on the structure of the central part of the Kura trough: Geotectonics, v. 10, p. 350–354.

Aghayeva, V., Sachsenhofer, R.F., van Baak, C.G.C., Bayramova, S., Ćorić, S., Frühwirth, M.J., Rzayeva, E., and Vincent, S.J., 2023, Stratigraphy of the Cenozoic succession in eastern Azerbaijan: Implications for petroleum systems and paleogeography in the Caspian basin: Marine and Petroleum Geology, p. 106148, doi:10.1016/j.marpetgeo.2023.106148.

Agustí, J., Vekua, A., Oms, O., Lordkipanidze, D., Bukhsianidze, M., Kiladze, G., and Rook, L., 2009, The Pliocene-Pleistocene succession of Kvabebi (Georgia) and the background to the early human occupation of Southern Caucasus: Quaternary Science Reviews, v. 28, p. 3275–3280.

Aitchison, J., 1986, The statistical analysis of compositional data (D. R. Cox, D. V. Hinkley, D. Rubin, & B. W. Silverman, Eds.): London, Champan and Hall, 416 p.

Aitchison, J., and Greenacre, M., 2002, Biplots of compositional data: Applied Statistics, v. 51, p. 375–392.

Alania, V., Beridze, T., Enukidze, O., Chagelishvili, R., Lebanidze, Z., Maqadze, D., Razmadze, A., Sadradze, N., and Tevzadze, N., 2021a, The geometry of the two orogens convergence and collision zones in Central Georgia: New data from seismic reflection profiles, *in* Bonali, F.L., Pasquaré Mariotto, F., and Tsereteli, N. eds., Building Knowledge for Geohazard Assessment and Management in the Caucasus and other Orogenic Regions, Dordrecht, Springer Netherlands, NATO Science for Peace and Security Series C: Environmental Security, p. 73–88, doi:10.1007/978-94-024-2046-3.

Alania, V., Chabukiani, A.O., Chagelishvili, R.L., and Enukidze, O.V., 2015, Growth structures , piggy-back basins and growth strata of the Georgian part of the Kura foreland fold – thrust belt : implications for Late Alpine kinematic evolution, *in* Sosson, M., Stephenson, R.A., and Adamia, S.A. eds., Tectonic Evolution of the Eastern Black Sea and Caucasus, Geological Society of London Special Publication, v. 428, doi:10.1144/SP428.5.

Alania, V., Tibaldi, A., Bonali, F.L., Enukidze, O., and Russo, E., 2021b, Structural Architecture of the Western Greater Caucasus Orogen: New Data from a Crustal-Scale Structural Cross-Section, *in* Bonali, F.L., Pasquaré Mariotto, F., and Tsereteli, N. eds., Building Knowledge for Geohazard Assessment and Management in the Caucasus and other Orogenic Regions, Dordrecht, Springer Netherlands, NATO Science for Peace and Security Series C: Environmental Security, p. 59–71, doi:10.1007/978-94-024-2046-3_5.

Aliyeva, E.G.-M., 2005, Reservoirs of the lower Pliocene Productive Series at the western flank of the South Caspian Basin: Lithology and Mineral Resources, v. 40, p. 267–278.

Ali-Zade, A.A., 2005, Geological Map of Azerbaijan Republic.:

Allen, P.A., and Heller, P.L., 2012, Dispersal and preservation of tectonically generated alluvial gravels in sedimentary basins, *in* Busby, C.J. and Azor, A. eds., Tectonics of Sedimentary Basins: Recent Advances, Blackwell Publishing, p. 111–130.

Allen, M.B., Jackson, J., and Walker, R., 2004, Late Cenozoic reorganization of the Arabia-Eurasia collision and the comparison of short-term and long-term deformation rates: Tectonics, v. 23, p. doi:10.1029/2003TC001530-doi:10.1029/2003TC001530.

Allen, M.B., Morton, A.C., Fanning, C.M., Ismail-Zadeh, A., and Kroonenberg, S.B., 2006, Zircon age constraints on sediment provenance in the Caspian region: Journal of the Geological Society of London, v. 163, p. 647–655.

Alvarez, N.O.C., and Roser, B.P., 2007, Geochemistry of black shales from the Lower Cretaceous Paja Formation, Eastern Cordillera, Colombia: Source weathering, provenance, and tectonic setting: Journal of South American Earth Sciences, v. 23, p. 271–289.

Amidon, W.H., Burbank, D., and Gehrels, G.E., 2005a, Construction of detrital mineral populations: insights from mixing of U-Pb zircon ages in Himalayan rivers: Basin Research, v. 17, p. 463–485, doi:10.1111/j.1365-2117.2005.00279.x.

Amidon, W.H., Burbank, D., and Gehrels, G.E., 2005b, U-Pb zircon ages as a sediment mixing tracer in the Nepal Himalaya: Earth and Planetary Science Letters, v. 235, p. 244–260.

Andersen, T., 2005, Detrital zircons as tracers of sedimentary provenance: limiting conditions from statistics and numerical simulation: Chemical Geology, v. 216, p. 249–270.

Armstrong-Altrin, J.S., and Verma, S.P., 2005, Critical evaluation of six tectonic setting discrimination diagrams using geochemical data of Neogene sediments from known tectonic settings: Sedimentary Geology, v. 177, p. 115–129.

Avdeev, B., and Niemi, N.A., 2011, Rapid Pliocene exhumation of the central Greater Caucasus constrained by low-temperature thermochronometry: Tectonics, v. 30, doi:10.1029/2010TC002808.

van Baak, C.G.C., 2010, Glacio-Marine transgressions of the early and middle Pleistocene Caspian Basin, Azerbaijan: Utrecht University, 21 p.

van Baak, C.G.C. et al., 2017, Paratethys response to the Messinian salinity crisis: Earth-Science Reviews, v. 172, p. 193–223, doi:10.1016/j.earscirev.2017.07.015.

van Baak, C.G.C., Grothe, A., Richards, K., Stoica, M., Aliyeva, E., Davies, G.R., Kuiper, K.F., and Krijgsman, W., 2019, Flooding of the Caspian Sea at the intensification of Northern Hemisphere Glaciations: Global and Planetary Change, v. 174, p. 153–163, doi:10.1016/j.gloplacha.2019.01.007.

van Baak, C.G.C., Vasiliev, I., Stoica, M., Kuiper, K.F., Forte, A.M., Aliyeva, E., and Krijgsman, W., 2013, A magnetostratigraphic time frame for Plio-Pleistocene transgressions in the South Caspian Basin, Azerbaijan: Global and Planetary Change, v. 103, p. 119–134, doi:10.1016/j.gloplacha.2012.05.004.

Bande, A., Horton, B.K., Ramírez, J.C., Mora, A., Parra, J.L., and Stockli, D.F., 2012, Clastic deposition, provenance, and sequence of Andean thrusting in the frontal Eastern Cordillera and Llanos foreland basin of Columbia: Geological Society of America Bulletin, v. 124, p. 59–76.

Banks, C.J., Robinson, A.G., and Williams, M.P., 1997, Structure and regional tectonics of the Achara-Trialet fold belt and the adjacent Rioni and Karli foreland basins, Republic of Georgia, *in* Robinson, A.G. ed., Regional and petroleum geology of the Black Sea and surrounding region, p. 331–346.

Bhatia, M.R., 1983, Plate tectonics and geochemical compisitions of sandstones: The Journal of Geology, v. 91, p. 611–627.

Bhatia, M.R., 1985, Rare earth element geochemistry of Australian Paleozoic graywackes and mudrocks: Provenance and tectonic control: Sedimentary Geology, v. 45, p. 97–113.

Bhatia, M.R., and Crook, K.A.W., 1986, Trace element characteristics of graywackes and tectonic setting discrimination of sedimentary basins: Contributions to Mineralogy and Petrology, v. 92, p. 181–193.

Blain, H.A., Agust??, J., Lordkipanidze, D., Rook, L., and Delfino, M., 2014, Paleoclimatic and paleoenvironmental context of the Early Pleistocene hominins from Dmanisi (Georgia, Lesser Caucasus) inferred from the herpetofaunal assemblage: Quaternary Science Reviews, v. 105, p. 136–150, doi:10.1016/j.quascirev.2014.10.004.

Bonjour, J.-L., and Dabard, M.-P., 1991, Ti/Nb ratios of clastic terrigenous sediments used as an indicator of provenance: Chemical Geology, v. 91, p. 257–267.

van der Boon, A., van Hinsbergen, D.J.J., Rezaeian, M., Gürer, D., Honarmand, M., Pastor-Galán, D., Krijgsman, W., and Langereis, C.G., 2018, Quantifying Arabia–Eurasia convergence accommodated in the Greater Caucasus by paleomagnetic reconstruction: Earth and Planetary Science Letters, v. 482, p. 454–469, doi:10.1016/j.epsl.2017.11.025.

Burbank, D., Beck, R.A., Raynolds, R.G.H., Hobbs, R.S., and Tahirkheli, R.A.K., 1988, Thrusting and gravel progradation in foreland basins: A test of post-thrusting gravel dispersal: Geology, v. 16, p. 1143–1146.

Capaldi, T.N., Horton, B.K., McKenzie, N.R., Mackaman-Lofland, C., Stockli, D.F., Ortiz, G., and Alvarado, P., 2020, Neogene Retroarc Foreland Basin Evolution, Sediment Provenance, and Magmatism in Response to Flat Slab Subduction, Western Argentina: Tectonics, v. 39, doi:10.1029/2019TC005958.

Carrapa, B., Strecker, M.R., and Sobel, E.R., 2006, Cenozoic orogenic growth in the Central Andes: Evidence from sedimentary rock provenance and apatite fission track thermochronology in the Fiambalá Basin, southernmost Puna Plateau margin (NW Argentina): Earth and Planetary Science Letters, v. 247, p. 82–100.

Cawood, P.A., Nemchin, A.A., Freeman, M., and Sircombe, K., 2003, Linking source and sedimentary basin: Detritral zircon record of sediment flux along a modern river system and implications for provenance studies: Earth and Planetary Science Letters, v. 210, p. 259–268.

Chen, G., and Robertson, A.H.F., 2020, User's guide to the interpretation of sandstones using whole-rock chemical data, exemplified by sandstones from Triassic to Miocene passive and active margin settings from the Southern Neotethys in Cyprus: Sedimentary Geology, v. 400, p. 105616, doi:10.1016/j.sedgeo.2020.105616.

Comas-Cufí, M., and Thió-Henestrosa, S., 2011, CoDaPack 2.0: a stand-alone, multi-platform compositional software, *in* Egozcue, J.J., Tolosana-Delgado, R., and Ortego, M.I. eds., 4th International Workshop on Compositional Data Analysis, Sant Feliu de Guixols.

Cowgill, E., Forte, A.M., Niemi, N.A., Avdeev, B., Tye, A.R., Trexler, C.C., Javakishvirli, Z., Elashvili, M., and Godoladze, T., 2016, Relict basin closure and crustal shortening budgets during continental collision: An example from Caucasus sediment provenance: Tectonics, v. 35, p. 2918–2947, doi:10.1002/2016TC004295.

Cowgill, E., Niemi, N.A., Forte, A.M., and Trexler, C.C., 2018, Reply to Comment by Vincent et al.: Tectonics, v. 37, p. 1017–1028, doi:10.1002/2017TC004793.

DeCelles, P.G., Gehrels, G.E., Quade, J., Ojha, T.P., Kapp, P.A., and Upreti, B.N., 1998, Neogene foreland basin deposits, erosional unroofing, and the kinematic history of hte Himalayan fold-thrust belt, western Nepal: Geological Society of America Bulletin, v. 110, p. 2–21.

Dhont, D., and Chorowicz, J., 2006, Review of the neotectonics of the Eastern Turkish-Armenian Plateau by geomorphic analysis of digital elevation model imagery: International Journal of Earth Science, v. 95, p. 34–49.

Dickinson, W.R., 1970, Interpreting detrital modes of graywacke and arkose: Journal of Sedimentary Petrology, v. 40, p. 695–707.

Dickinson, W.R., and Suczek, C.A., 1979, Plate tectonics and sandstone compositions: American Association of Petroleum Geologists Bulletin, v. 63, p. 2164–2182.

Egozcue, J.J., and Pawlowsky-Glahn, V., 2005, Groups of parts and their balances in compositional data analysis: Mathematical Geology, v. 37, p. 795–828.

Egozcue, J.J., Pawlowsky-Glahn, V., Mateu-Figueras, G., and Barceló-Vidal, C., 2003, Isometric logratio transformations for compositional data analysis: Mathematical Geology, v. 35, p. 279–300.

Fedo, C., Nesbitt, H.W., and Young, G.M., 1995, Unraveling the effects of pottassium metasomatism in sedimentary rocks and paleosols, with implications for paleoweathering conditions and provenance: Geology, v. 23, p. 921–924.

Fedo, C., Sircombe, K., and Rainbird, R.H., 2003, Detrital zircon analysis of the sedimentary record, *in* Hanchar, J.M. and Hoskin, P.W.O. eds., Zircon, p. 277–303.

Forte, A.M., 2012, Late Cenozoic Evolution of the Greater Caucasus Mountains and Kura Foreland Basin: Implications for Early Orogenesis: University of California, Davis.

Forte, A.M., and Cowgill, E., 2013, Late Cenozoic base-level variations of the Caspian Sea: A new review of its history and proposed driving mechanisms: Palaeogeography, Palaeoclimatology, Palaeoecology, v. 386, p. 392–407, doi:10.1016/j.palaeo.2013.05.035.

Forte, A.M., Cowgill, E., Bernardin, T., Kreylos, O., and Hamann, B., 2010, Late Cenozoic deformation of the Kura fold-thrust belt, southern Greater Caucasus: Geological Society of America Bulletin, v. 122, p. 465–486.

Forte, A.M., Cowgill, E., Murtuzayev, I., Kangarli, T., and Stoica, M., 2013, Structual geometries and magnitude of shortening in the eastern Kura fold-thrust belt, Azerbaijan: Implications for the development of the Greater Caucasus Mountains: Tectonics, v. 32, doi:10.1002/tect.20032.

Forte, A.M., Cowgill, E., and Whipple, K.X., 2014, Transition from a singly vergent to doubly vergent wedge in a young orogen: The Greater Caucasus: Tectonics, v. 33, p. 2077–2101, doi:10.1002/2014TC003651.

Forte, A.M., Gutterman, K., Van Soest, M.C., and Gallagher, K., 2022a, Building a Young Mountain Range: Insight into the Growth of the Greater Caucasus Mountains from Detrital Zircon (U-Th)/He Thermochronology and 10Be Erosion Rates: Tectonics, doi:10.1029/2021TC006900.

Forte, A.M., Leonard, J.S., Rossi, M.W., Whipple, K.X., Heimsath, A.M., Sukhishvili, L., Godoladze, T., and Kadirov, F., 2022b, Low variability runoff inhibits coupling of climate, tectonics, and topography in the Greater Caucasus: Earth and Planetary Science Letters, v. 584, doi:10.1016/j.epsl.2022.117525.

Forte, A.M., Sumner, D.Y., Cowgill, E., Stoica, M., Murtuzayev, I., Kangarli, T., Elashvili, M., Godoladze, T., and Javakishvirli, Z., 2015a, Late Miocene to Pliocene stratigraphy of the Kura Basin, a subbasin of the South Caspian Basin: Implications for the diachroneity of stage boundaries: Basin Research, doi:10.1111/bre.12069.

Forte, A.M., Whipple, K.X., and Cowgill, E., 2015b, Drainage network reveals patterns and history of active deformation in the eastern Greater Caucasus: Geosphere, v. 11, doi:10.1130/GES01121.1.

Froggatt, P.C., 1992, Standardization of the chemical analysis of tephra deposits. Report of the ICCT Working Group: Quaternary International, v. 13–14, p. 93–96, doi:10.1016/1040-6182(92)90014-S.

Gabunia, L., Vekua, A., and Lordkipanidze, D., 2000, The environmental contexts of early human occupation of Georgia (Transcaucasia): Journal of Human Evolution, v. 38, p. 785–802, doi:10.1006/jhev.1999.0383.

Gamkrelidze, I.P., 1986, Geodynamic evolution of the Caucasus and adjacent areas in alpine time: Tectonophysics, v. 127, p. 261–277.

Garber, K.L., Finzel, E.S., and Pearson, D.M., 2020, Provenance of Synorogenic Foreland Basin Strata in Southwestern Montana Requires Revision of Existing Models for Laramide Tectonism: North American Cordillera: Tectonics, v. 39, doi:10.1029/2019TC005944.

Garzanti, E., and Andò, S., 2007, Chapter 20 Heavy Mineral Concentration in Modern Sands: Implications for Provenance Interpretation, *in* Developments in Sedimentology, Elsevier, v. 58, p. 517–545, doi:10.1016/S0070-4571(07)58020-9.

Garzanti, E., Vezzoli, G., Lombardo, B., Andó, S., Mauri, E., Monguzzi, S., and Russo, M., 2004, Collision-orogen provenance (Western Alps): Detrital signatures and unroofing trends: The Journal of Geology, v. 112, p. 143–164.

Gehrels, G.E., 2014, Detrital Zircon U-Pb Geochronology Applied to Tectonics: Annual Review of Earth and Planetary Sciences, v. 42, p. 127–149, doi:10.1146/annurev-earth-050212-124012.

Gehrels, G.E., 2012, Detrital Zircon U-Pb geochronology: Current Methods and New Opportunties, *in* Busby, C.J. and Azor, A. eds., Recent advances in tectonics of sedimentary basins, Blackwell Publishing, p. 47–62.

Gehrels, G.E., Valencia, V., and Pullen, A., 2006, Detrital zircon geochronology by laser-ablation mutlicollector icpms at the Arizona Laserchron Center, *in* Olszewski, T. ed., Geochronology: Emerging Opportunities, Paleontological Society Short Course, Philadelphia, The Paleontological Society, v. 12.

Gehrels, G.E., Valencia, V., and Ruiz, J., 2008, Enhanced precision, accuracy, efficiency, and spatial resoultion of U-Pb ages by laser ablation-multicollector-inductively coupled plasma-mass spectrometry: Geochemistry Geophysics Geosystems, v. 9, doi:10.1029/2007GC001805.

Grömping, U., 2009, Variable Importance Assessment in Regression: Linear Regression versus Random Forest: The American Statistician, v. 63, p. 308–319, doi:10.1198/tast.2009.08199.

Gunnels, M., Yetrimishli, G., Kazimova, S., and Sandvol, E., 2020, Seismotectonic evidence for subduction beneath the Eastern Greater Caucasus: Geophysical Journal International, v. 224, p. 1825–1834, doi:10.1093/gji/ggaa522.

Harnois, L., 1988, The CIW index: A new chemical index of weathering: Sedimentary Geology, v. 55, p. 319–322.

Herron, M.M., 1988, Geochemical classification of terrigenous sands and shales from core or log data: Journal of Sedimentary Petrology, v. 58, p. 820–829.

van Hinsbergen, D.J.J., Torsvik, T.H., Schmid, S.M., Matenco, LC., Maffione, M., Vissers, R.L.M., Gurer, D., and Spakman, W., 2019, Orogenic architecture of the Mediterranean region and kinematic reconstruction of its tectonic evolution since the Triassic: Gondwana Research, doi:10.1016/j.gr.2019.07.009.

Hoth, S., Adam, J., Kukowski, N., and Oncken, O., 2006, Influence of erosion on the kinematics of bivergent orogens: Results from scaled sandbox simulations, *in* Willett, S.D., Hovius, N., Brandon, M.T., and Fisher, D. eds., Tectonics, Climate, and Landscape Evolution, Geological Society of America, v. 398, p. 201–225.

Hoth, S., Hoffmann-Rothe, A., and Kukowski, N., 2007, Frontal accretion: An internal clock for bivergent wedge deformation and surface uplift: Journal of Geophysical Research, v. 112, p. B06408–B06408, doi:10.1029/2006JB004357.

Ibañez-Mejia, M., Pullen, A., Pepper, M., Urbani, F., Ghoshal, G., and Ibañez-Mejia, J.C., 2018, Use and abuse of detrital zircon U-Pb geochronology—A case from the Río Orinoco delta, eastern Venezuela: Geology, doi:10.1130/G45596.1.

Ingersoll, R.V., 1990, Actualistic sandstone petrofacies: Discriminating modern and ancient source rocks: Geology, v. 18, p. 733–736.

Ingersoll, R.V., Bullard, T.F., Ford, R.L., Grimm, J.P., Pickle, J.D., and Sares, S.W., 1984, The effect of grain size on detrital modes: A test of the Gazzi-Dickinson point-coutning method: Journal of Sedimentary Petrology, v. 54, p. 103–116.

Jackson, J., 1992, Partitioning of strike-slip convergent motion between Eurasia and Arabia in eastern Turkey and the Caucasus: Journal of Geophysical Research, v. 97, p. 12,412-471,479.

Jian, D., Williams, S.E., Yu, S., and Zhao, G., 2022, Quantifying the Link Between the Detrital Zircon Record and Tectonic Settings: Journal of Geophysical Research: Solid Earth, v. 127, doi:10.1029/2022JB024606.

Joannin, S. et al., 2010, Early Pleistocene climate cycles in continental deposits of the Lesser Caucasus of Armenia inferred from palynology, magnetostratigraphy, and 40Ar/39Ar: Earth and Planetary Science Letters, v. 291, p. 149–158.

Jones, R.W., and Simmons, M., 1996, A review of the stratigraphy of Eastern Paratethys (Oligocene-Holocene): Bulletin of the Natural History Museum of London, v. 52, p. 25–49.

Khain, V.Ye., 1975, Structure and Main Stages in the Tectono-Magmatic Development of the Caucasus: An Attempt at Geodynamic Interpretation: American Journal of Science, v. 275 A, p. 131–156.

Kopp, M.L., and Shcherba, I.G., 1985, Late alpine development of the east Caucasus: Geotectonics, v. 19, p. 497–507.

Kovda, I., Mora, C.I., and Wilding, L.P., 2008, PaleoVertisols of the northwest Caucasus: (Micro)morphological, physical, chemical, and isotopic constraints on early to late Pliestocene climate: Journal of Plant Nutrition and Soil Science, v. 171, p. 498–508.

Kremenetskiy, A.A., Lapidus, A.V., and Voronovskiy, S.N., 1990, New data on the age and oil and gas potential of the basement of Kura depression, based on ultradeep well logs: Doklady of the National Academy of Sciences of the USSR, v. 312, p. 139–142.

Krijgsman, W. et al., 2019, Quaternary time scales for the Pontocaspian domain: Interbasinal connectivity and faunal evolution: Earth-Science Reviews, v. 188, p. 1–40, doi:10.1016/j.earscirev.2018.10.013.

Krijgsman, W., Stoica, M., Vasiliev, I., and Popov, V.V., 2010, Rise and fall of the Paratethys Sea during the Messinian salinity crisis: Earth and Planetary Science Letters, v. 290, p. 183–191.

Kroonenberg, S.B. et al., 2005, Two deltas, two basins, one river, one sea: The modern Volga Delta as an analogue for the Neogene Productive Series, South Caspian Basin, *in* River Deltas-Concepts, Models, and Examples, p. 231–256.

Krzanowski, W.J., 2000, Principles of Multivariate Analysis; A user's perspective (A. C. Atkinson, J. B. Copas, D. A. Pierce, M. J. Schervish, & D. M. Titterington, Eds.): Oxford University Press, 586 p.

Kuehn, S.C., Froese, D.G., and Shane, P.A.R., 2011, The INTAV intercomparison of electron-beam microanalysis of glass by tephrochronology laboratories: Results and recommendations: Quaternary International, v. 246, p. 19–47, doi:10.1016/j.quaint.2011.08.022.

Kvavadze, E., and Vekua, A., 1993, Vegetation and climate of the Dmanisi man period (East Georgia) from palynological data: Acta Palaeobotanica, v. 23, p. 343–355.

Lasaga, A.C., Soler, J.M., Ganor, J., Burch, T.E., and Nagy, K.L., 1994, Chemical weathering rate laws and global geochemical cycles: Geochimica et Cosmochimica Acta, v. 58, p. 2361–2386, doi:10.1016/0016-7037(94)90016-7.

Laskowski, A.K., DeCelles, P.G., and Gehrels, G.E., 2013, Detrital zircon geochronology of Cordilleran retroarc foreland basin strata, western North America: CORDILLERAN FORELAND DZ GEOCHRONOLOGY: Tectonics, v. 32, p. 1027–1048, doi:10.1002/tect.20065.

Lawrence, R.L., Cox, R., Mapes, R.W., and Coleman, D.S., 2011, Hydrodyanmic fractionation of zircon age populations: Geological Society of America Bulletin, v. 123, p. 295–305.

Lawton, T.F., Hunt, G.J., and Gehrels, G.E., 2010, Detrital zircon record of thrust belt unroofing in Lower Cretaceous synorogenic conglomerates, central Utah: Geology, v. 38, p. 463–466.

Lazarev, S. et al., 2021, Five-fold expansion of the Caspian Sea in the late Pliocene: New and revised magnetostratigraphic and 40Ar/39Ar age constraints on the Akchagylian Stage: Global and Planetary Change, v. 206, p. 103624, doi:10.1016/j.gloplacha.2021.103624.

Lazarev, S., Jorissen, E.L., van de Velde, S., Rausch, L., Stoica, M., Wesselingh, F.P., Van Baak, C.G.C., Yanina, T.A., Aliyeva, E., and Krijgsman, W., 2019, Magneto-biostratigraphic age constraints on the palaeoenvironmental evolution of the South Caspian basin during the Early-Middle Pleistocene (Kura basin, Azerbaijan): Quaternary Science Reviews, v. 222, p. 105895–105895, doi:10.1016/j.quascirev.2019.105895.

Leary, R.J., DeCelles, P.G., Quade, J., Gehrels, G.E., and Waanders, G., 2016, The Liuqu Conglomerate, southern Tibet: Early Miocene basin development related to deformation within the Great Counter Thrust system: Lithosphere, v. 8, p. 427–450, doi:10.1130/L542.1.

Lease, R.O., Burbank, D., Gehrels, G.E., Wang, Z., and Yuan, D., 2007, Signatures of mountain building: Detrital zircon U/Pb ages from northeastern Tibet: Geology, v. 35, p. 239–242.

Li, C., and Yang, S., 2010, Is chemical index of alteration (CIA) a reliable proxy for chemical weathering in global drainage basins? American Journal of Science, v. 310, p. 111–127.

Link, P.K., Fanning, C.M., and Beranek, L.P., 2005, Reliability and longitudinal change of detrital-zircon age spectra in the Snake River system, Idaho and Wyoming: An example of reproducing the bumpy barcode: Sedimentary Geology, v. 182, p. 101–142.

Lowe, D.J., 2011, Tephrochronology and its application: A review: Quaternary Geochronology, v. 6, p. 107–153, doi:10.1016/j.quageo.2010.08.003.

Lowe, D.J., Pearce, N.J.G., Jorgensen, M.A., Kuehn, S.C., Tryon, C.A., and Hayward, C.L., 2017, Correlating tephras and cryptotephras using glass compositional analyses and numerical and statistical methods: Review and evaluation: Quaternary Science Reviews, v. 175, p. 1–44, doi:10.1016/j.quascirev.2017.08.003.

Malkowski, M.A., Sharman, G.R., Johnstone, S.A., Grove, M.J., Kimbrough, D.L., and Graham, S.A., 2019, Dilution and propagation of provenance trends in sand and mud: Geochemistry and detrital zircon geochronology of modern sediment from central California (U.S.A.): American Journal of Science, v. 319, p. 846–902, doi:10.2475/10.2019.02.

Martín-Fernández, J.A., Barceló-Vidal, C., and Pawlowsky-Glahn, V., 2003, Dealing with zeros and missing values in compositional data sets using nonparametric imputation: Mathematical Geology, v. 35, p. 253–278.

McKenzie, D., Jackson, J., and Priestley, K., 2019, Continental collisions and the origin of subcrustal continental earthquakes: Canadian Journal of Earth Sciences, v. 56, p. 1101–1118, doi:10.1139/cjes-2018-0289.

McLennan, S.M., 2001, Relationship between the trace element composition of sedimentary rocks and upper continental crust: Geochemistry Geophysics Geosystems, v. 2.

McLennan, S.M., 1993, Weathering and global denudation: The Journal of Geology, v. 101, p. 295–303.

McLennan, S.M., and Taylor, S.R., 1991, Sedimentary rocks and crustal evolution: Tectonic setting and secular trends: The Journal of Geology, v. 99, p. 1–21.

Messager, E., Lordkipanidze, D., Delhon, C., and Ferring, C.R., 2010a, Palaeoecological implications of the Lower Pleistocene phytolith record from the Dmanisi Site (Georgia): Palaeogeography, Palaeoclimatology, Palaeoecology, v. 288, p. 1–13, doi:10.1016/j.palaeo.2010.01.020.

Messager, E., Lordkipanidze, D., Kvavadze, E., Ferring, C.R., and Voinchet, P., 2010b, Palaeoenvironmental reconstruction of Dmanisi site (Georgia) based on palaeobotanical data: Quaternary International, v. 223–224, p. 20–27.

Morton, A.C., Allen, M.B., Simmons, M., Spathopoulos, F., Still, J., Hinds, D.J., Ismail-Zadeh, A., and Kroonenberg, S.B., 2003, Provenance patterns in a neotectonic basin: Pliocene and Quaternary sediment supply to the South Caspian: Basin Research, v. 15, p. 321–337.

Morton, A.C., and Yaxley, G., 2007, Detrital apatite geochemistry and its application in provenance studies, *in* Arribas, J., Critelli, S., and Johnsson, M.J. eds., Sedimentary provenance and petrogenesis: Perspectives from petrography and geochemistry, p. 319–344.

Mosar, J., Kangarli, T., Bochud, M., Glasmacher, U.A., Rast, A., Brunet, M.-F., and Sosson, M., 2010, Cenozoic-Recent tectonics and uplift in the Greater Caucasus: a perspective from Azerbaijan, *in* Sosson, M., Kaymakci, N., Stephenson, R.A., Bergerat, F., and Starostenko, V.I. eds., Sedimentary Basin Tectonics from the Black Sea and Caucasus to the Arabian Platform, London, Geological Society, v. 340, p. 261–280.

Mumladze, T., Forte, A.M., Cowgill, E., Trexler, C.C., Niemi, N.A., Yikilmaz, M.B., and Kellogg, L.H., 2015, Subducted, detached, and torn slabs beneath the Greater Caucasus: GeoResJ, v. 5, p. 36–46, doi:10.1016/j.grj.2014.09.004.

Nagel, S., Castelltort, S., Garzanti, E., Lin, A.T., Willett, S.D., Mouthereau, F., Limonta, M., and Adatte, T., 2014, Provenance Evolution During Arc-Continent Collision: Sedimentary Petrography of Miocene To Pleistocene Sediments In the Western Foreland Basin of Taiwan: Journal of Sedimentary Research, v. 84, p. 513–528, doi:10.2110/jsr.2014.44.

Nesbitt, H.W., and Young, G.M., 1982, Early Proterozoic climates and plate motions inferred from major element chemistry of lutites: Nature, v. 299, p. 715–717.

Ogg, J.G., 2020, Geomagnetic Polarity Time Scale, *in* Gradstein, F.M., Ogg, J.G., Schmitz, M.D., and Ogg, G.M. eds., Geologic Time Scale, Elsevier, v. 1, p. 159–192.

Ohta, T., and Arai, H., 2007, Statistical empirical index of chemical weathering in igneous rocks: A new tool for evaluating the degree of weathering: Chemical Geology, v. 240, p. 280–297.

Palcu, D.V., Vasiliev, I., Stoica, M., and Krijgsman, W., 2019, The end of the Great Khersonian Drying of Eurasia: Magnetostratigraphic dating of the Maeotian transgression in the Eastern Paratethys: Basin Research, v. 31, p. 33–58, doi:10.1111/bre.12307.

Panaiotu, C.E., Vasiliev, I., Panaiotu, C.G., Krijgsman, W., and Langereis, C.G., 2007, Provenance analysis as a key to orogenic exhumation: a case study from the East Carpathians (Romania): Terra Nova, v. 19, p. 120–126.

Pawlowsky-Glahn, V., and Egozcue, J.J., 2006, Compositional data and their analysis: an introduction, *in* Buccianti, A., Mateu-Figueras, G., and Pawlowsky-Glahn, V. eds., Compositional data analysis in the geosciences: From theory to practice, London, Geological Society, v. 264, p. 1–10.

Pe-Piper, G., Triantafyllidis, S., and Piper, D.J.W., 2008, Geochemical identification of clastic sediment provenance from known sources of similar geology: The Cretaceous Scotian Basin, Canada: Journal of Sedimentary Research, v. 78, p. 595–607.

Perkins, M.E., Nash, W.P., Brown, F.H., and Fleck, R.J., 1995, Fallout tuffs of Trapper Creek, Idaho—A record of Miocene explosive volcanism in the Snake River Plain volcanic province: Geological Society of America Bulletin, p. 23.

Philip, H., Cisternas, A., Gvishiani, A., and Gorshkov, A., 1989, The Caucasus: an actual example of the initial stages of continental collision: Tectonophysics, v. 161, p. 1–21.

Plank, T., and Langmuir, C.H., 1998, The chemical composition of subducting sediment and its consequences for the crust and mantle: Chemical Geology, v. 145, p. 325–394.

Popov, S.V., Antipov, M.P., Zastroshnov, A.S., Kurina, E.E., and Pinchuk, T.N., 2010, Sea-level fluctuations on the northern shelf of the eastern Paratethys in the Oligocene-Neogene: Stratigraphy and Geological Correlation, v. 18, p. 200–224.

Popov, S.V., Shcherba, I.G., Ilyina, L.B., Nevesskaya, L.A., Paramonova, N.P., Khondkarian, S.O., and Magyar, I., 2006, Late Miocene to Pliocene palaeogeography of the Paratethys and its relation to the Mediterranean: Palaeogeography, Palaeoclimatology, Palaeoecology, v. 238, p. 91–106.

Raines, K.M., Hubbard, S.M., Kukulski, R.B., Leier, A.L., and Gehrels, G.E., 2013, Sediment dispersal in an evolving foreland: Detrital zircon geochronology from Upper Jurassic and lowermost Cretaceous strata, Alberta Basin, Canada: Geological Society of America Bulletin, doi:10.1130/B30671.1.

Reilinger, R. et al., 2006, GPS constraints on continental deformation in the Africa-Arabia-Eurasia continental collision zone and implications for the dynamics of plate interactions: Journal of Geophysical Research, v. 111, p. doi:10.1029/2005JB004051-doi:10.1029/2005JB004051.

Reynolds, A.D. et al., 1998, Implications of Outrcrop Geology for Reservoirs in the Neogene Productive Series: Apsheron Peninsula, Azerbaijan: American Association of Petroleum Geologists Bulletin, v. 82, p. 25–49.

Richards, K., van Baak, C.G.C., Athersuch, J., Hoyle, T.M., Stoica, M., Austin, W.E.N., Cage, A.G., Wonders, A.A.H., Marret, F., and Pinnington, C.A., 2018, Palynology and micropalaeontology of the Pliocene - Pleistocene transition in outcrop from the western Caspian Sea, Azerbaijan: Potential links with the Mediterranean, Black Sea and the Arctic Ocean? Palaeogeography, Palaeoclimatology, Palaeoecology, v. 511, p. 119–143, doi:10.1016/j.palaeo.2018.07.018.

Rolland, Y., Sosson, M., Adamia, Sh., and Sadradze, N., 2011, Prolonged Variscan to Alpine history of an active Eurasian margin (Georgia, Armenia) revealed by 40Ar/39Ar dating: Gondwana Research, v. 20, p. 798–815, doi:10.1016/j.gr.2011.05.007.

Roman, D.C., Campisano, C., Quade, J., DiMaggio, E., Arrowsmith, J.R., and Feibel, C., 2008, Composite tephrostratigraphy of the Dikika, Gona, Hadar, and Ledi-Geraru project areas, northern Awash, Ethiopia, *in* The Geology of Early Humans in the Horn of Africa, Geological Society of America, doi:10.1130/2008.2446(05).

Roser, B.P., and Korsch, R.J., 1986, Determination of tectonics setting of sandstone-mudstone suites using SiO2 and K2O/Na2O ratio: The Journal of Geology, v. 94, p. 635–650.

Roser, B.P., and Korsch, R.J., 1988, Provenance signatures of sandstone-mudstone suites determined using discriminant function analysis of major-element data: Chemical Geology, v. 67, p. 119–139.

Safonova, I., Maruyama, S., Hirata, T., Kon, Y., and Rino, S., 2010, LA ICP MS U-Pb ages of detrital zircons from Russia largest rivers: Implications for major granitoid events in Eurasia and global eposides of supercontinent formation: Journal of Geodynamics, v. 50, p. 134–153.

Saintot, A., Brunet, M.-F., Yakovlev, F., Sebrier, M., Stephenson, R.A., Ershov, A.V., Chalot-Prat, F., and McCann, T., 2006, The Mesozoic-Cenozoic tectonic evolution of the Greater

Caucasus, *in* Gee, D.G. and Stephenson, R.A. eds., European Lithosphere Dynamics, London, Geological Society, v. 32.

Saylor, J.E., Jordan, J.C., Sundell, K.E., Wang, X., Wang, S., and Deng, T., 2018, Topographic growth of the Jishi Shan and its impact on basin and hydrology evolution, NE Tibetan Plateau: Basin Research, v. 30, p. 544–563, doi:10.1111/bre.12264.

Saylor, J.E., and Sundell, K.E., 2016, Quantifying comparison of large detrital geochronology data sets: Geosphere, v. 12, p. 203–220, doi:10.1130/GES01237.1.

Shikalibeily, E.Sh., Abdullayev, R.N., and Ali-Zade, Ak.A., 1988, Geological results from the Saatly superdeep drillhole: International Geology Review, v. 30, p. 1272–1277.

Shimodaira, H., 2004, Approximately unbiased tests of regions using multistep-multiscale bootstrap resampling: Annals of Statistics, v. 32, p. 2616–2641.

Sinclair, H.D., 1997, Flysch to molasse transition in peripheral foreland basins: The role of the passive margin versus slab breakoff: Geology, v. 25, p. 1123–1126.

Skolbeltsyn, G., Mellors, R., Gök, R., Türkelli, N., Yetirmishli, G., and Sandvol, E., 2014, Upper mantle S wave velocity structure of the East Anatolian-Caucasus region: Tectonics, v. 33, p. 207–221, doi:10.1002/2013TC003334.

Smosna, R., Bruner, K.R., and Burns, A., 1999, Numerical analysis of sandstone composition, provenance, and paleogeography: Journal of Sedimentary Research, v. 69, p. 1063–1070.

Sobornov, K.O., 1996, Lateral variations in structural styles of tectonic wedging in the northeastern Caucasus: Bulletin of Canadian Petroleum Geology, v. 44, p. 385–399.

Sobornov, K., 2021, STRUCTURE AND EVOLUTION OF THE TEREK-CASPIAN FOLD-AND-THRUST BELT: NEW INSIGHTS FROM REGIONAL SEISMIC DATA: Journal of Petroleum Geology, v. 44, p. 259–286, doi:10.1111/jpg.12793.

Sobornov, K.O., 1994, Structure and petroleum potential of the Dagestan thrust belt, northeastern Caucasus, Russia: Bulletin of Canadian Petroleum Geology, v. 42, p. 352–364.

Somin, M.L., 2011, Pre-Jurassic Basement of the Greater Caucasus: Brief Overview: Turkish Journal of Earth Sciences, v. 20, p. 546–610.

Spencer, C.J., Kirkland, C.L., Nicholas, M.W., and Spencer, C.J., 2018, Implications of erosion and bedrock composition on zircon fertility; examples from South America and Western Australia: Terra Nova, v. 30, p. 289–295, doi:10.1111/ter.12338.

Sukhishvili, L., Forte, A.M., Merebashvili, G., Leonard, J., Whipple, K.X., Javakhishvili, Z., Heimsath, A., and Godoladze, T., 2020, Active deformation and Plio-Pleistocene fluvial reorganization of the western Kura fold–thrust belt, Georgia: implications for the evolution of the Greater Caucasus Mountains: Geological Magazine, p. 1–15, doi:10.1017/S0016756820000709.

Sundell, K., and Saylor, J.E., 2017, Unmixing detrital geochronology age distributions: Geochemistry, Geophysics, Geosystems, v. 18, p. 2872–2886, doi:10.1002/2016GC006774.

Suzuki, R., and Shimodaira, H., 2009, pvclust: Heirarchical Clustering with P-values via Multiscale Bootstrap Resampling:, http://www.is.titech.ac.jp/~shimo/prog/pvclust/.

Taylor, S.R., and McLennan, S.M., 1985, The Continental Crust: Its composition and evolution: Malden, Mass, Blackwell.

Team, R.D.C., 2010, R: A language and environment for statistical computing:, http://www.r-project.org.

Thomas, C.W., and Aitchison, J., 2006, Log-ratios and geochemical discrimination of Scottish Dalradian limestones: a case study, *in* Buccianti, A., Mateu-Figueras, G., and Pawlowsky-Glahn, V. eds., Compositional data analysis in the geosciences: From theory to practice, London, Geological Society, v. 264, p. 25–41.

Tibaldi, A., Babayev, G., Bonali, F.L., Pasquaré Mariotto, F., Russo, E., Tsereteli, N., and Corti, N., 2021, Active Kinematics of the Greater Caucasus from Seismological and GPS Data: A Review, *in* Bonali, F.L., Pasquaré Mariotto, F., and Tsereteli, N. eds., Building Knowledge for Geohazard Assessment and Management in the Caucasus and other Orogenic Regions, Dordrecht, Springer Netherlands, NATO Science for Peace and Security Series C: Environmental Security, p. 33–57, doi:10.1007/978-94-024-2046-3_4.

Tibaldi, A., Bonali, F.L., Russo, E., and Pasquarè Mariotto, F.A., 2018, Structural development and stress evolution of an arcuate fold-and-thrust system, southwestern Greater Caucasus, Republic of Georgia: Journal of Asian Earth Sciences, v. 156, p. 226–245, doi:10.1016/j.jseaes.2018.01.025.

Tibaldi, A., Russo, E., Bonali, F.L., Alania, V., Chabukiani, A., Enukidze, O., and Tsereteli, N., 2017, 3-D anatomy of an active fault-propagation fold: A multidisciplinary case study from Tsaishi, western Caucasus (Georgia): Tectonophysics, v. 717, p. 253–269, doi:10.1016/j.tecto.2017.08.006.

Totten, M.W., Hanan, M.A., and Weaver, B.L., 2000, Beyond whole-rock geochemistry of shales: The importance of assessing mineralogic controls for revealing tectonic discriminants of mulitple sediment sources for the Ouachita Mountain flysch deposits: Geological Society of America Bulletin, v. 112, p. 1012–1022.

Trexler, C.C., Cowgill, E.S., Niemi, N.A., Vasey, D.A., and Godoladze, T., 2022, Tectonostratigraphy and major structures of the Georgian Greater Caucasus: Implications for structural architecture, along-strike continuity, and orogen evolution: Geosphere, doi:10.1130/GES02385.1.

Trexler, C.C., Cowgill, E., Spencer, J.Q.G., and Godoladze, T., 2020, Rate of active shortening across the southern thrust front of the Greater Caucasus in western Georgia from kinematic modeling of folded river terraces above a listric thrust: Earth and Planetary Science Letters, v. 544, p. 116362, doi:10.1016/j.epsl.2020.116362.

Tsereteli, N., Tibaldi, A., Alania, V., Gventsadse, A., Enukidze, O., Varazanashvili, O., and Müller, B.I.R., 2016, Active tectonics of central-western Caucasus, Georgia: Tectonophysics, v. 691, p. 328–344, doi:10.1016/j.tecto.2016.10.025.

Tye, A.R., Niemi, N.A., Cowgill, E., Kadirov, F.A., and Babayev, G.R., 2022, Diverse Deformation Mechanisms and Lithologic Controls in an Active Orogenic Wedge: Structural Geology and Thermochronometry of the Eastern Greater Caucasus: Tectonics, v. 41, doi:10.1029/2022TC007349.

Tye, A.R., Niemi, N.A., Safarov, R.T., Kadirov, F.A., and Babayev, G.R., 2020, Sedimentary response to a collision orogeny recorded in detrital zircon provenance of Greater Caucasus foreland basin sediments: Basin Research, p. bre.12499, doi:10.1111/bre.12499.

Tye, A.R., Wolf, A.S., and Niemi, N.A., 2019, Bayesian population correlation: A probabilistic approach to inferring and comparing population distributions for detrital zircon ages: Chemical Geology, doi:10.1016/J.CHEMGEO.2019.03.039.

Van Baak, C.G.C., Stoica, M., Grothe, A., Aliyeva, E., and Krijgsman, W., 2016, Mediterranean-Paratethys connectivity during the Messinian salinity crisis: The Pontian of Azerbaijan: Global and Planetary Change, v. 141, p. 63–81, doi:10.1016/j.gloplacha.2016.04.005.

Vasey, D.A., Cowgill, E., and Cooper, K.M., 2021, A Preliminary Framework for Magmatism in Modern Continental Back-Arc Basins and Its Application to the Triassic-Jurassic Tectonic Evolution of the Caucasus: Geochemistry, Geophysics, Geosystems, v. 22, doi:10.1029/2020GC009490.

Vasey, D.A., Cowgill, E., Roeske, S.M., Niemi, N.A., Godoladze, T., Skhirtladze, I., and Gogoladze, S., 2020, Evolution of the Greater Caucasus Basement and Formation of the Main Caucasus Thrust, Georgia: Tectonics, v. 39, doi:10.1029/2019TC005828.

Vasiliev, I., Iosifidi, A.G., Khramov, A.N., Krijgsman, W., Kuiper, K.F., Langereis, C.G., Popov, V.V., Stoica, M., Tomsha, V.A., and Yudin, S.V., 2011, Magnetostratigraphy and radio-isotope dating of upper Miocene-lower Pliocene sedimentary successions of the Black Sea Basin

(Taman Peninsula, Russia): Palaeogeography, Palaeoclimatology, Palaeoecology, v. 310, p. 163–175.

Venables, W.N., and Ripley, B.D., 2002, Modern Applied Statistics with S: New York, Springer-Verlag, 495 p.

Vermeesch, P., 2013, Multi-sample comparison of detrital age distributions: Chemical Geology, v. 341, p. 140–146, doi:10.1016/j.chemgeo.2013.01.010.

Vermeesch, P., 2012, On the visualization of detrital age distributions: Chemical Geology, v. 312–313, p. 190–194.

Vezzoli, G., Garzanti, E., Limonta, M., and Radeff, G., 2020, Focused erosion at the core of the Greater Caucasus: Sediment generation and dispersal from Mt. Elbrus to the Caspian Sea: Earth-Science Reviews, v. 200, p. 102987, doi:10.1016/j.earscirev.2019.102987.

Vezzoli, G., Garzanti, E., Vincent, S.J., Ando, S., Carter, A., and Resentini, A., 2014, Tracking sediment provenance and erosional evolution of the western Greater Caucasus: Earth Surface Processes and Landforms, doi:10.1002/esp.3567.

Vincent, S.J., Braham, W., Lavrishchev, V.A., Maynard, J.R., and Harland, M., 2016, The formation and inversion of the western Greater Caucasus Basin and the uplift of the western Greater Caucasus: Implications for the wider Black Sea region: Tectonics, v. 35, p. 2948–2962, doi:10.1002/2016TC004204.

Vincent, S.J., Carter, A., Lavrishchev, A., Rice, S.P., Barabadze, T.G., and Hovius, N., 2011, The exhumation of the western Greater Caucasus: a thermochronometric study: Geological Magazine, v. 148, p. 1–21, doi:10.1017/S0016756810000257.

Vincent, S.J., Davies, C.E., Richards, K., and Aliyeva, E., 2010, Contrasting Pliocene fluvial depostional systems within the rapidly subsiding South Caspian Basin; a case study of the palaeo-Volga and palaeo-Kura river systems in the Surakhany Suite, Upper Productive Series, onshore Azerbaijan: Marine and Petroleum Geology, v. 27, p. 2079–2106.

Vincent, S.J., Hyden, F., and Braham, W., 2014, Along-strike variations in the composition of sandstones dervied from the uplifting western Greater Caucasus: causes and implications for reservoir quality prediciton in the Eastern Black Sea, *in* Scott, R.A., Smyth, H.R., Morton, A.C., and Richardson, N. eds., Sediment Provenance Studies in Hydrocarbon Exploration and Production, London, Geological Society, p. 11–127, doi:10.1144/SP386.15.

Vincent, S.J., Morton, A.C., Carter, A., Gibbs, S., and Teimuraz, G.B., 2007, Oligocene uplift of the Western Greater Caucasus: an effect of initial Arabia-Eurasia collision: Terra Nova, v. 19, p. 160–166.

Vincent, S.J., Morton, A.C., Hyden, F., and Fanning, M., 2013, Insights from petrography, mineralogy and U-Pb zircon geochronology into the provenance and reservoir potential of Cenozoic siliciclastic depositional systems supplying the northern margin of the nothern margin of the Eastern Black Sea: Marine and Petroleum Geology, v. 45, p. 331–348.

Vincent, S.J., Saintot, A., Mosar, J., Okay, A.I., and Nikishin, A.M., 2018, Comment on "Relict basin closure and crustal shortening budgets during continental collision: An example from Caucasus sediment provenance" by Cowgill et al (2016): Tectonics, v. 37, p. 1006–1016, doi:10.1002/2017TC004515.

Vincent, S.J., Somin, M.L., Carter, A., Vezzoli, G., Fox, M., and Vautravers, B., 2020, Testing Models of Cenozoic Exhumation in the Western Greater Caucasus: Tectonics, v. 39, doi:10.1029/2018TC005451.

Von Eynatten, H., 2003, Petrography and chemistry of sandstones from the Swiss Molasse Basin: an archive of the Oligocene to Miocene evolution of the Central Alps: Sedimentology, v. 50, p. 703–724, doi:10.1046/j.1365-3091.2003.00571.x.

Von Eynatten, H., Barceló-Vidal, C., and Pawlowsky-Glahn, V., 2003, Composition and discrimination of sandstones: A statistical evaluation of different analytical methods: Journal of Sedimentary Research, v. 73, p. 47–57.

Vortisch, W., Harding, D., and Morgan, J., 2003, Petrographic analysis using cathodoluminescence microscopy with simultaneous energy-dispersive X-ray spectroscopy: Mineralogy and Petrology, v. 79, p. 193–202, doi:10.1007/s00710-003-0009-1.

Wang, C.Y., Campbell, I.H., Stepanov, A.S., Allen, C.M., and Burtsev, I.N., 2011, Growth rate of the preserved continental crust: II. Constraints from Hf and O isotopes in detrital zircons from Greater Russian Rivers: Geochimica et Cosmochimica Acta, v. 75, p. 1308–1345.

Whipple, K.X., and Meade, B., 2004, Controls on the strength of coupling among climate, erosion, and deformation in two-sided, frictional orogenic wedges at steady state: Journal of Geophysical Research, v. 109, p. F01011–F01011, doi:10.1029/2003JF000019.

Whipple, K.X., and Meade, B., 2006, Orogen response to changes in climatic and tectonic forcing: Earth and Planetary Science Letters, v. 243, p. 218–228.

Žák, J., Svojtka, M., Hajná, J., and Ackerman, L., 2020, Detrital zircon geochronology and processes in accretionary wedges: Earth-Science Reviews, v. 207, p. 103214, doi:10.1016/j.earscirev.2020.103214.

Zonenshain, L.P., and Le Pichon, X., 1986, Deep basins of the Black Sea and Caspian Sea as remnants of Mesozoic back-arc basins: Tectonophysics, v. 123, p. 181–211.

Zubakov, V.A., and Borzenkova, I.I., 1990, Global palaeoclimate of the Late Cenozoic: Amsterdam, Elsevier.